THE UNIVERSITY OF CALGARY

A Vibrational Circular Dichroism Study of Deoxyoctanucleotides and Their Daunorubicin Complexes

by

Vanitha Maharaj

A DISSERTATION
SUBMITTED TO THE FACULTY OF GRADUATE STUDIES
IN PARTIAL FULFILMENT OF THE REQUIREMENTS FOR THE
DEGREE OF DOCTOR OF PHILOSOPHY

DEPARTMENT OF CHEMISTRY

CALGARY, ALBERTA
OCTOBER, 1996

National Library of Canada
Acquisitions and Bibliographic Services
395 Wellington Street
Ottawa ON K1A 0N4
Canada

Bibliothèque nationale du Canada
Acquisitions et services bibliographiques
395, rue Wellington
Ottawa ON K1A 0N4
Canada

Your file Votre référence

Our file Notre référence

0-612-20751-X

Canada

Abstract

VCD spectroscopy identifies the three-dimensional conformation and absolute configuration of optically active systems. The primary objectives of this study were achieved in that VCD is capable of revealing sequence specificity and demonstrating conformational changes accompanying DNA-drug interactions using deoxyoctanucleotides with daunorubicin, an anti-tumor drug currently used for the treatment of acute leukemia.

The FTIR/VCD spectra of the deoxyoctanucleotides and their daunorubicin complexes were measured in the continuous 1750-850 cm^{-1} range. The most prominent VCD features occur between 1750-1600 cm^{-1} ascribed to dipolar coupling of the carbonyl and/or skeletal stretching vibrations of the stacked nucleotide bases, and 1100-1050 cm^{-1} arising from the symmetric PO_2^- stretching vibrations of the sugar-phosphate backbone. For the deoxyoctanucleotides with varying sequences the structural changes were monitored by wavenumber shifts and intensity variations in the VCD spectra. The nucleotide base modes appear to reveal sequence specificity in contrast to the phosphate backbone vibrations.

Daunorubicin is an intercalating drug which inserts itself between two stacked C-G base-pairs causing the DNA helix to unwind and lengthen. The DNA topology is thus changed and daunorubicin acts as a physical barrier that inhibits DNA replication and transcription processes thereby stopping cell proliferation. The VCD spectra of the deoxyoctanucleotides upon intercalation with daunorubicin, in some cases, revealed the elimination of VCD couplets attributed to the C-G base-pair, which is consistent with the DNA sequence preference of daunorubicin according to previous literature.

The FTIR/VCD spectra of the deoxyoctanucleotides and their daunorubicin complexes were simulated with the non-degenerate extended coupled oscillator (NECO) model, which assumes that the predominant interaction is due to dipolar coupling of the stacked

nucleotide bases and the phosphate backbone in the helical orientation. The IR absorption positions and the electric transition dipole moments, parameters required by the NECO model, were derived from *ab initio* calculations using the B3-LYP procedure with the 6-31G** basis set. The former was adjusted according to experimental IR spectra before implementation into the NECO model. For a simplistic model, the overall features of the FTIR/VCD spectra of the deoxyoctanucleotides and their daunorubicin complexes were simulated adequately.

Acknowledgements

I would like to express my sincere gratitude to all those who have been instrumental in this research project, with special thanks to:

Dr. H. Wieser, my supervisor, for the opportunity to work on this stimulating project, his continuous enthuism and encouragement.

Dr. J.H. van de Sande, my co-supervisor, for his time, patience and guidance through the course of this project

Dr. A Rauk, for his time on informative computational discussions.

Dr. Petr Bour , ***Dr. Dimiter Tsankov***, and ***Jennifer McCann***, my colleagues whose contributions to this project were invaluable.

Dr. Doug Phillips, ***Bernd Kalisch***, ***Kim Wagstaff***, and ***Mike Siewart*** who assisted with various technical aspects of this project.

Jeff Walker for his objective insight, encouragement and understanding.

My family for their unconditional love and support.

I acknowledge scholarships from the Alberta Heritage Foundation for Medical Research (***AHFMR***) and the Foundation for Research and Development (***FRD***) in South Africa, and teaching assistantships from the University of Calgary.

To

Mum, Dad

Shanil & Pranitha

Table of Contents

List of Tables

List of Figures

List of Appendices

1. Introduction

Vibrational circular dichroism (VCD) spectroscopy measures the differential absorption of circularly polarized infrared radiation, hence VCD is specific to chiral (optically active) systems. The three-dimensional conformation and absolute configuration of chiral molecules are the key features that can be identified with VCD spectroscopy. In comparison with IR and Raman spectroscopy, VCD spectra by their nature offer information and detail additional to their parent spectra. The desire to understand DNA-drug interactions inspired this research project, to investigate whether VCD was capable of revealing sequence specificity and subsequently to examine DNA interactions with the anti-tumor drug daunorubicin. Currently, daunorubicin is clinically used for the treatment of acute leukemia.

1.1 Objectives

- To establish systematic relationships between DNA structural characteristics and spectral features arising from VCD spectroscopy.

- To demonstrate the utility of VCD spectroscopy as an analytical method for probing conformational changes accompanying DNA-drug interactions using DNA-daunorubicin as an example.

1.2 Sequence Selection

Since the ultimate objective of this study involves DNA-drug interactions it is necessary to take into account the fact that most drugs have sequence specificity, and therefore base-pairs can successively be varied with a view to provide determinants for DNA-drug interactions. There are two major categories of DNA-drug interactions (Wilson, 1990), each classified by the type of drug and its mode of binding, namely:

i) *Intercalating drugs*, e.g. anthracycline antibiotics of which daunorubicin is but one example, which causes unwinding and lengthening of the helix upon binding thereby profoundly changing the DNA conformation (Neidle, 1984). These structural changes may be monitored by wavenumbers shifts and/or intensities variations in the VCD spectra.

ii) *Groove-binding drugs*, e.g netropsin, which bind to DNA in the minor groove by displacing the spine of hydration and reproducing its coordination without greatly distorting the DNA conformation. For VCD measurements in this instance it appears more appropriate to monitor the drug rather than the DNA.

The DNA-drug interaction can therefore be probed by monitoring the VCD spectrum of either the drug or the DNA. The latter is preferred for our objectives thus advocating daunorubicin as the drug of choice for this study. DNA sequences containing eight base-pairs were used to minimize end fraying and unwinding of the double helix. The molecules selected were systematically varied self-complementary deoxyoctanucleotide sequences of the type d(CGNNNNCG).d(CGNNNNCG), where N can be adenine (A), cytosine (C), thymine (T) or guanine (G). This specific series was targeted on the basis of previously reported structural details, and the fact that it showed sequence variants and contained determinants for daunorubicin binding.

a) d(CGCGCGCG).d(CGCGCGCG)

The VCD spectrum in the 1750-1550 cm^{-1} region has previously been reported for the deoxydecanucleotide, d(CGCGCGCGCG).d(CGCGCGCGCG), (Zhong *et al.*, 1990; Gulotta *et al.*, 1989). The corresponding deoxyoctanucleotide is expected to have similar characteristics and was therefore chosen as a standard and the principal sequence in this study.

b) d(CGCATGCG).d(CGCATGCG) and d(CGCTAGCG).d(CGCTAGCG)

The deoxyhexanucleotides, d(CGATCG).d(CGATCG) and d(CGTACG).d(CGTACG), complexed with the antitumor drug daunorubicin have been characterized by X-ray crystallography (Frederick *et al.*, 1990; Wang *et al.*, 1987). The corresponding deoxyoctanucleotides are expected to behave in a similar fashion. The affects on the VCD spectra of substituting the principal sequence with two A-T base-pairs and switching their order shall also be considered.

c) d(CGTATACG).d(CGTATACG), d(CGATATCG).d(CGATATCG) and d(CGAATTCG).d(CGAATTCG)

The deoxydodecanucleotides, d(CGCGATATCGCG).d(CGCGATATCGCG) complexed with netropsin and d(CGCGAATTCGCG).d(CGCGAATTCGCG), have been characterized by X-ray crystallography (Dickerson, 1990). The corresponding deoxyoctanucleotides are expected to behave in a similar fashion. The effects on the VCD spectra of substituting the principal sequence with four A-T base-pairs and switching them will also be considered.

d) d(CGCGTGCG).d(CGCGTGCG)

G-T is an example of a transition mismatch base-pair, which has the correct purine but incorrect pyrimidine. A mismatch (wobble) base-pair is attained by a sideways displacement of one base relative to its position in the regular Watson-Crick geometry. The resulting loss of a hydrogen bond leads to a reduced stability which may be compensated for by improved base stacking. The effect of a mismatched G-T base-pair on Z-DNA has been investigated by X-ray crystallography of the deoxyhexanucleotide, d(CGCGTG).d(CGCGTG), (Ho *et al.*, 1985). The corresponding deoxyoctanucleotide is in the B-conformation and expected to behave differently. The effect on the VCD spectra of substituting the principal sequence with two G-T base-pairs will be considered.

1.3 Thesis Outline

Deoxyoctanucleotides comprising the self-complementary sequence d(CGNNNNCG). d(CGNNNNCG) where N can be A, T, C or G, were synthesized by using automated phosphoramidite chemistry on a DNA synthesizer, purified by the principle of molecular weight exclusion, assessed by polyacrylamide gel electrophoresis and analyzed by ultraviolet (UV) absorption, electronic circular dichroism (ECD) and melting temperature (T_m) measurements (Chapter 2).

Daunorubicin is an anti-tumor drug, that binds to DNA by the process of intercalation. The drug inserts itself between two stacked C-G base-pairs thereby unwinding and lengthening the DNA helix. Daunorubicin thus creates a physical barrier that inhibits DNA replication and transcription processes, hence stopping cell proliferation. The intravenous administration of daunorubicin induces physiological side-effects including severe acute toxicities. Daunorubicin exhibits DNA sequence preference as established by solution, X-ray crystallography and theoretical studies (Chapter 3).

The UV absorption and ECD spectra of the selected deoxyoctanucleotides were measured in the 31250-50000 cm^{-1} range. Particularly prominent ECD features occur between 33300-42500 cm^{-1} (300-235 nm), which are ascribed to the $\pi \rightarrow \pi^*$ electronic transitions of the nucleotide bases. The FT-IR absorption and VCD spectra of the selected deoxyoctanucleotides and their daunorubicin complexes were measured in the continuous 1750-850 cm^{-1} range (Chapter 4).

In order to extract the desired structural information, the observed UV/IR absorption and ECD/VCD spectra were compared with those theoretically simulated by an approximate model, viz. the non-degenerate extended coupled oscillator (NECO) model. This model assumes that the predominant interaction is due to dipolar coupling of the stacked nucleotide bases and the phosphate backbone in the helical orientation (Chapter 5).

The vibrational transitions are assigned on the basis of *ab initio* harmonic wavenumbers and intensities while the electronic transitions are assigned on the basis of *ab initio* excitation energies. Optimized geometries, harmonic force fields and atomic polar tensors (electric transition dipole moments) of the nucleotide bases (C, G, A and T), nucleotide base pairs (C-G and A-T) and the dimethyl phosphate anion were calculated using density functional theory (DFT) with B3-LYP functionals and the 6-31G** basis set. Atomic polar tensors of the nucleotide bases were also calculated using configuration interaction singles (CIS) with the 6-31+G* basis set, for the simulation of the UV absorption and ECD spectra. The standard B-DNA conformation of the selected deoxyoctanucleotides were generated using MSI's molecular modeling system (*Insight II* 95.0, 1995) and were modified to incorporate daunorubicin at the terminal base-pairs. Accordingly, the magnitude and orientation of the relevant electric transition dipole moments required by the coupled oscillator model were derived from *ab initio* calculations and transformed to helical coordinates.

The two regions of interest, viz. 1750-1500 cm^{-1} and 1100-1050 cm^{-1} were simulated concurrently for both the IR absorption and VCD spectra of the selected deoxyoctanucleotides and their daunorubicin complexes, while the UV absorption and ECD spectra of the deoxyoctanucleotides were simulated in the single region of interest, viz. 33300-42500 cm^{-1}.

2. Deoxyoctanucleotides

2.1 Introduction

Deoxyribonucleic acid (DNA) is central to life since a single heritable element of DNA constitutes a gene. DNA is a linear polymer comprising nucleotide monomers which are constructed from three components: a deoxyribose sugar (see Figure 1), a phosphate anion (see Figure 1) and a nitrogen heterocyclic base, either purine or pyrimidine. Cytosine (C) and thymine (T) are pyrimidines while adenine (A) and guanine (G) constitute purines (illustrated in Figure 2). The conventional Watson-Crick nucleotide base-pairs include A-T and C-G, with two and three hydrogen bonds, respectively (see Figure 3), therefore C-G is more stable than A-T (Blackburn, 1990; Saenger, 1984a) . The integrity of transmission of the genetic code relies on the specific pairings of A-T and C-G bases, nevertheless mispairings do occasionally occur in nature. G-T is an example of a transition mismatch base-pair where a purine (G) is paired with an incorrect pyrimidine (T) (Ho *et al.*, 1985; Blackburn, 1990). Nucleotide monomers linked via phosphodiester bonds between the 3′ and 5′ positions of successive deoxyribose sugars constitute the primary DNA structure while the double-stranded, base-paired helical DNA forms the secondary DNA structure. In a Watson-Crick type double helix the orientation of the sugar-phosphate backbone of the two strands is directed opposite, antiparallel, to each other. A self-complementary deoxyoctanucleotide forms an eight base-pair, double-stranded, antiparallel segment of DNA.

Polymorphism of DNA has been well established, with the relative stability of the DNA conformation depending upon environmental conditions such as salt concentration, extent of hydration, and the base sequence. The two common right-handed helical conformations, viz. B-DNA (aqueous conditions) and A-DNA (less hydrated aqueous conditions), are differentiated by sugar puckering, base tilt relative to the helix axis, distance of base pairs from the center of the helix and relative dimensions of the major

and minor grooves. Z-DNA has a left-handed helical conformation, induced under high alcohol or salt conditions, which differs in several respects from the A- and B-conformations (Blackburn, 1990; Saenger, 1984b).

B-DNA is the preferred conformation *in vivo*, hence DNA segments with the B-conformation were used in this research. In B-DNA there are an average of 10.4 base-pairs per turn of the helix, corresponding to an average helical-twist (pitch) of 34.6° between two base-pairs and their separation along the helix axis (rise) being 3.4 Å. The helix axis passes through the center of each base-pair, and the base-pairs are stacked perpendicular to the helix axis. Hence the major and minor grooves of B-DNA are of similar depths with the major groove being almost twice as wide as the minor groove. The $C_{2'}$-*endo* pucker conformation of the deoxyribose sugar predominates in B-DNA. In this conformation the five membered ring exists in an envelope form in which four of the five atoms are coplanar while the 2′ atom lies above the plane (Kennard & Hunter, 1991; Blackburn, 1990; Saenger, 1984b).

2.2 Methods of Investigation

A multitude of spectroscopic techniques has been used to investigate DNA conformations with X-ray crystallography, nuclear magnetic resonance (NMR), UV absorption and electronic circular dichroism (ECD) being the most diagnostic. Spectroscopic analysis of DNA is demanding since DNA is chiral and expresses its biological activity only in solution.

Detailed information regarding the arrangement of atoms within the DNA molecule is required to obtain the three-dimensional structure. X-ray crystallography uses the interaction of X-rays with electrons within molecules, contained in a well ordered crystal, to obtain an electron density map of the molecule, which can then be interpreted as an atomic model (Branden & Tooze, 1991). Crystallization of DNA molecules can be

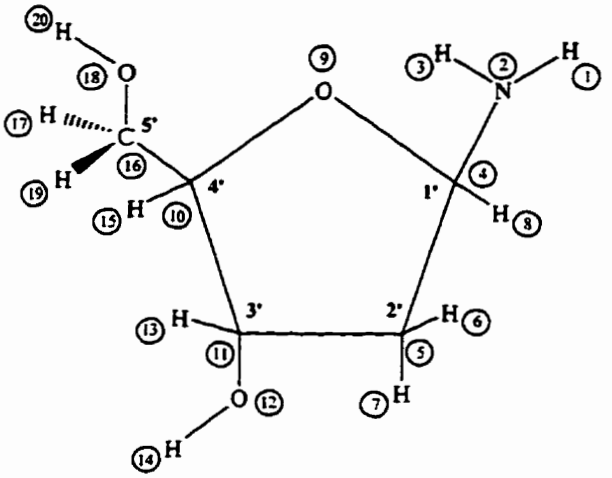

1-Amino-Deoxyribose

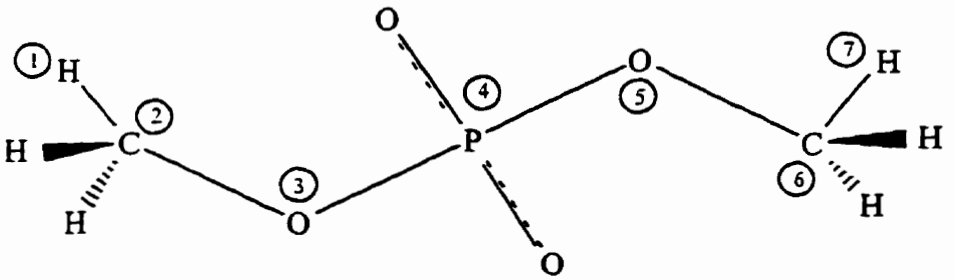

Dimethyl Phosphate

Figure 1
Model for DNA Sugar–Phosphate Backbone

where an amino group and two methyl groups are appended to the deoxyribose and phosphate residues of DNA, respectively, for computational modeling. The encircled numbers represent those used for the computation described in Chapter 5.

PYRIMIDINES

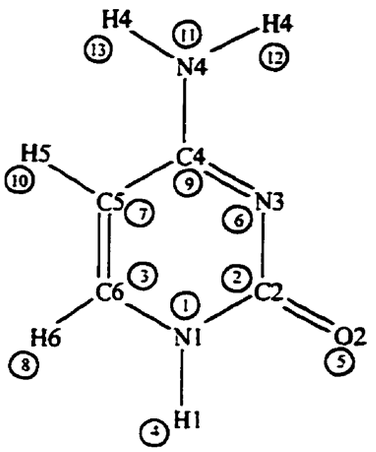

Cytosine (C)

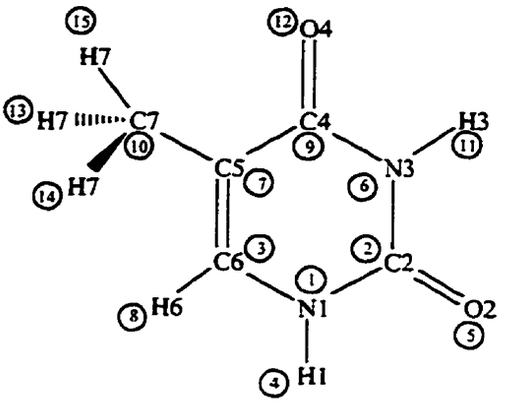

Thymine (T)

PURINES

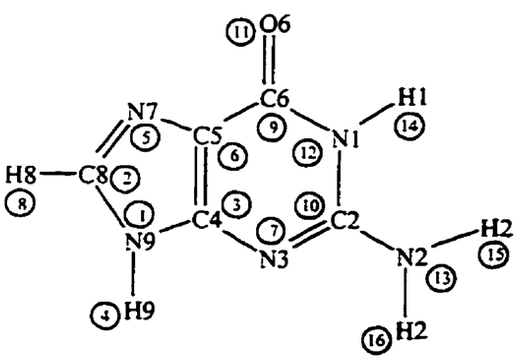

Guanine (G)

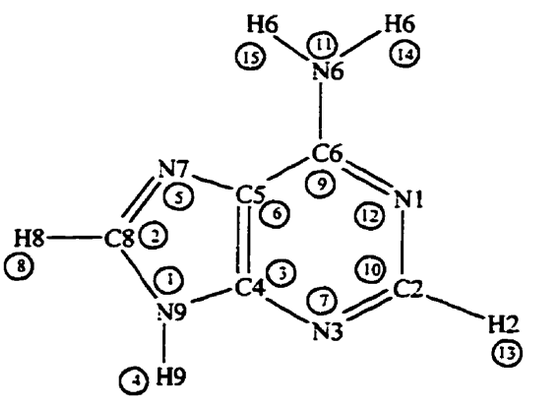

Adenine (A)

Figure 2
Nucleotide Bases in DNA

where (C) and (T) are pyrimidines while (G) and (A) are purines. The encircled numbers represent those used for the computation described in Chapter 5.

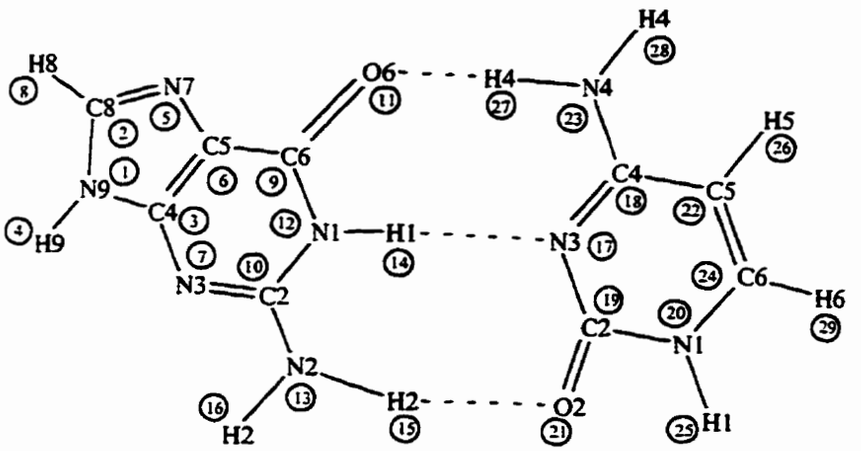

Guanine - Cytosine (G-C)

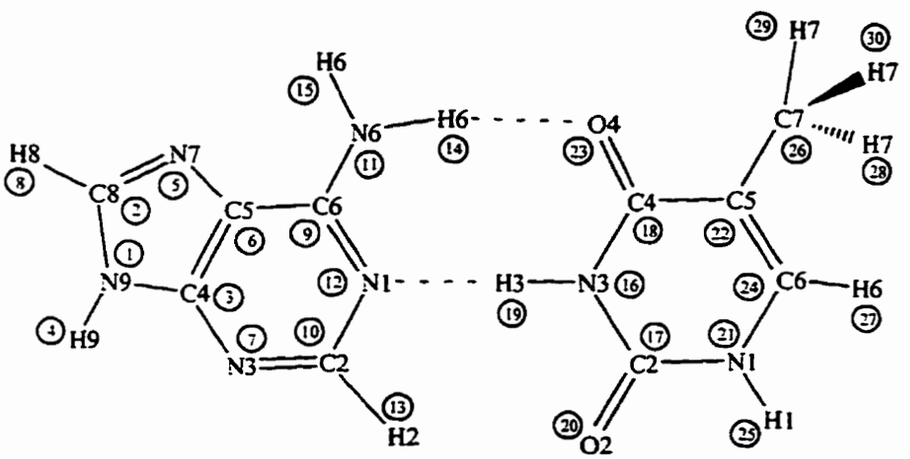

Adenine - Thymine (A-T)

Figure 3
Nucleotide Base-Pairs in DNA

where C-G and A-T are conventional Watson-Crick base-pairs. The encircled numbers represent those used for the computation described in Chapter 5.

difficult to achieve. Improvements in the methods for the chemical synthesis of DNA have recently made it possible to study single crystals of short DNA molecules of various sequences (Wang & Gao, 1990; Dickerson, 1990). NMR spectroscopy uses the magnetic-spin properties of the atomic nuclei within a molecule to obtain a list of distance constraints between atoms in the molecules, from which a three-dimensional structure of the DNA molecule can be derived. This method requires concentrated solutions of DNA (Branden & Tooze, 1991). Nucleotides have UV absorption spectra that are similar to those of their constituent bases ($\lambda_{max} \cong 260$ nm) because the deoxyribose sugar and phosphate show no appreciable UV absorbance above 230 nm. A prerequisite to DNA helix formation is base stacking, which is accompanied by a reduction in UV absorbance (hypochromicity) at 260 nm by virtue of the electronic interactions between the bases in DNA. Thus, UV constitutes a reliable probe to monitor the formation and disruption of double helices. ECD, a differential method characterized by measuring left versus right circularly polarized UV/Vis radiation, is complementary to UV and often used to monitor conformational transitions in DNA (Sheardy, 1991). UV and ECD measurements are commonly utilized to determine temperature dependent changes in base stacking and helix-coil transitions (Blackburn, 1990).

2.3 Deoxyoctanucleotide Sequence Selection

Self-complementary deoxyoctanucleotide sequences were chosen because eight base-pairs will minimize end fraying and unwinding of the double helix (duplex) (Dickerson, 1990). Seven self-complementary deoxyoctanucleotides, consisting of systematically varied sequences of the type $^{5'}$d(CGNNNNCG)$_{3'}$.$^{5'}$d(CGNNNNCG)$_{3'}$, where N can be C, G, A or T, were selected. These sequences were assembled by systematic base substitutions, as illustrated in Figure 4 and discussed in Chapter 1, to evaluate interactions with daunorubicin, an anti-tumor intercalating drug. The following self-complementary sequences, whose X-ray crystal structures were reported in the literature, were instrumental in the deoxyoctanucleotide sequence selection:

d(CGATCG).d(CGATCG)- 2(daunorubicin) (Frederick *et al.*, 1990), d(CGATCG). d(CGATCG)-2(daunorubicin) (Wang *et al.*, 1987), d(CGCGAATTCGCG). d(CGCGAATTCGCG) (Dickerson, 1990) and d(CGCGTG).d(CGCGTG) (Ho *et al.*, 1985).

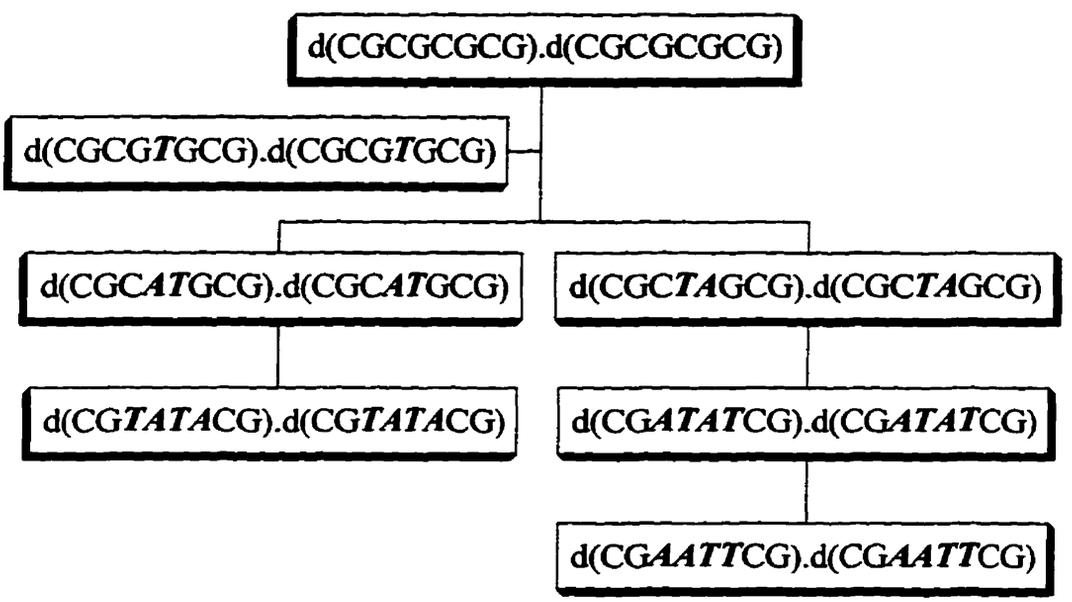

Figure 4
Deoxyoctanucleotide Sequence Selection

where the substitutions in the sequences are indicated with bold-italics

2.4 Deoxyoctanucleotide Synthesis, Purification and Analysis

2.4.1 Deoxyoctanucleotide Synthesis

The seven self-complementary deoxyoctanucleotides (illustrated in Figure 4) were synthesized by using automated phosphoramidite chemistry on a DNA synthesizer (Applied Biosystems, Model 380B) in the Faculty of Medicine at the University of

Calgary. The DNA synthesizer employs solid-phase synthesis (Caruthers, 1985; Blackburn & Gait, 1990) which entails a heterogeneous coupling reaction between a deoxyribonucleotide derivative in solution and another residue bound to an insoluble support. The reaction can be forced to high yield with a large excess of the soluble deoxyribonucleotide. The support-bound product dinucleotide can be removed from the excess of reactant mononucleotide by filtration and washing. Other reactions can also be carried out heterogeneously and reagents removed similarly. This process is much faster than a conventional separation technique in solution.

The four essential steps in solid-phase synthesis are:

- attachment of the first deoxyribonucleoside to the support
- assembly of the oligonucleotide chain
- deprotection and removal of the oligonucleotide from the support
- purification

Assembly of the protected oligonucleotide chain can be conducted on a very small scale (0.2 μM) with machinery to add solvents and reagents reproducibly to the solid support, followed by filtration and purification (Blackburn & Gait, 1990).

2.4.2 Deoxyoctanucleotide Purification

The deoxyoctanucleotide samples were desalted (exchange NH_4^+ from the synthesis with Na^+) and the smaller molecular weight contaminants (mainly aromatics used as protective groups in the synthesis) were removed. Samples of deoxyoctanucleotides were dissolved in 1.5 ml of 1.0 M NaCl, applied to a Sephadex G-25 packed column (75 x 3 cm) and eluted with distilled water. A flow rate of 200 ml/h was maintained and a UV detector monitored the eluent. The deoxyoctanucleotides, present in the eluent, were then lyophilized to dryness. A neutral pH was maintained because acidic conditions result in depurination.

Polyacrylamide gel electrophoresis was used to analyze and assess the purity of the deoxyoctanucleotides. Vertical polyacrylamide gel electrophoresis was carried out on a 1 mm thick gel glass plate sandwich (20 x 20 cm). The gel preparation is described in detail elsewhere (Maniatis *et al.*, 1982). In essence, the cross-linking of 15% polyacrylamide, which contained 0.75% bis-polyacrylamide, was accomplished by a free radical reaction. The polyacrylamide denaturing gel also contained 8 M urea, which destabilized the double helix. The running buffer of the denaturing and native gels were 66 mM trisborate (TB) at pH 8.3 together with 0.1 mM EDTA (TBE), and 15 mM $MgCl_2$ (TBM), respectively. Concentrations of 0.02 mM and 0.04 mM of the lyophilized deoxyoctanucleotides were resuspended in 95% formamide and 20% glycerol, to increase the density of the sample, for the denaturing and native gels, respectively. The denaturing gel was run at 40 V cm^{-1} for 0.5 h while the native gel was run at 10 V cm^{-1} for 16 h at 4°C.

The deoxyoctanucleotides were allowed to move down 70% of the polyacrylamide gel as indicated by the marker dye, bromophenol blue, which incidentally is indicative of a deoxyoctanucleotide. The samples were then located on the gels by UV-illumination on a TLC plate (Polygram Cell300 polyethylimine) impregnated with a fluorescent indicator. The native gel was stained on ice with 1 M NaCl and 0.5 μg/ml ethidium bromide and observed under a fluorescent light bulb. The denaturing gel compared the relative purity and length of the sequences whereas the non-denaturing gel was indicative of the duplex stability.

2.4.3 Deoxyoctanucleotide Quantification

The deoxyoctanucleotide concentration was determined by perchlorate analysis (Germann, 1989). This method is based on the sum of each mononucleotide's contribution to the total extinction coefficient (E) at a particular wavelength. It is imperative that the sample is completely denatured therefore a high concentration of

$NaClO_4$ was used which destabilizes the duplex while still being optically transparent and suitable for high temperature measurements.

An aliquot of the stock solution was diluted with 5.0 M $NaClO_4$ and 50 mM tris(hydroxymethyl)aminomethane at pH 7.2. This deoxyoctanucleotide solution was held in a sealed cuvette to avoid evaporation losses. The absorbance was measured in triplicate at 90°C and 260 nm. The deoxyoctanucleotide concentration was calculated from the theoretical molar extinction coefficient of the denatured form, given by Equation 1:

$$E_{[D]} = \frac{[a \cdot A\varepsilon(r) + c \cdot C\varepsilon(r) + g \cdot G\varepsilon(r) + t \cdot T\varepsilon(r)]}{[a + c + g + t]} \; M^{-1}cm^{-1} \qquad (1)$$

where a, c, g and t represent the number of A, C, G and T residues and $A\varepsilon(r)$, $C\varepsilon(r)$, $G\varepsilon(r)$ and $T\varepsilon(r)$ are the mononucleotide extinction coefficients at 90°C and 260 nm, respectively (Germann, 1989):

$A\varepsilon(r) = 15500\ M^{-1}cm^{-1}$ $\qquad$ $C\varepsilon(r) = 6980\ M^{-1}cm^{-1}$

$G\varepsilon(r) = 11200\ M^{-1}cm^{-1}$ $\qquad$ $T\varepsilon(r) = 9360\ M^{-1}cm^{-1}$

The calculated extinction coefficients per residue of the selected sequences are listed in Table 1. These extinction coefficients are used in conjunction with the absorbances measured at 90°C and 260 nm to calculate the deoxyoctanucleotide concentrations using Equation 2:

$$M_{[DUPLEX]} = \frac{1}{16} \times \left(\frac{A_{260\,nm}}{E} \right) = 2\ mM \qquad (2)$$

In order to normalize adequate concentrations for vibrational circular dichroism (VCD) spectroscopy, final duplex concentrations of 20 mM were used for all seven deoxyoctanucleotides. Therefore 1.0 ml of 2.0 mM duplex deoxyoctanucleotide was

lyophilized to dryness and then resuspended in 0.1 ml D_2O to give a final concentration of 20 mM duplex deoxyoctanucleotide.

Table 1
Calculated Extinction Coefficients of Deoxyoctanucleotides

Deoxyoctanucleotide Sequences	Extinction Coefficients (E) ($M^{-1}cm^{-1}$)
d(CGCGCGCG).d(CGCGCGCG)	9090
d(CGCGTGCG).d(CGCGTGCG)	9387.5
d(CGCATGCG).d(CGCATGCG)	9925
d(CGCTAGCG).d(CGCTAGCG)	9925
d(CGATATCG).d(CGATATCG)	10760
d(CGTATACG).d(CGTATACG)	10760
d(CGAATTCG).d(CGAATTCG)	10760

2.4.4 Melting Temperature Measurements

Melting temperature measurements are used to determine the stability of DNA sequences. An increase in temperature can cause the denaturation of DNA, which occurs when all the hydrogen bonds are broken and the two strands of the double helix separate. This process occurs over a narrow temperature range and is associated with a hyperchromic effect, i.e. the UV absorbance at 260 nm increases due to the breakdown of the double helix. The midpoint of the temperature range over which the transition from native double-strand to denatured random coil DNA occurs, is called the melting point and is designated T_m (Saenger, 1984a).

T_m measurements were adopted in this work to assess the stability of base substitutions in the selected deoxyoctanucleotides. A temperature range of 5 to 75°C was used with

ramps of 1°C/min. The system was buffered with 40 mM sodium cacodylate (dimethyl arsenic acid) and 50 mM NaCl in D_2O. A concentration of 0.1 mM deoxyoctanucleotide was measured at $A_{260\ nm}$ with a pathlength of 1 cm. Melting temperatures were calculated with the thermal analysis application which operates in conjunction with the Varian-Cary base software on a Cary3E UV/Vis spectrophotometer.

2.5 Results and Discussion

The denaturing polyacrylamide gel electrophoresis results corroborate the high purity of the selected deoxyoctanucleotides used in this study. The alignment of the deoxyoctanucleotides evident on the denaturing polyacrylamide gel (see Figure 5) verifies the high purity and the equivalent chain length of the seven deoxyoctanucleotides. The native gel on the other hand, did take up the intercalating drug, ethidium bromide, which is only possible in the presence of a double helix, thereby confirming the double helical existence of the deoxyoctanucleotides.

Melting temperature measurements (see Table 2) are indicative of the relative stability of the seven deoxyoctanucleotides. The total stabilizing energy of base-paired DNA helices are derived from two components, viz. base-pairing which is composition dependent and base-stacking which is both composition and sequence dependent, with the base-pairing being more important. Base-pair stacking and hydrogen-bonding interactions are responsible for the cooperative behavior of DNA helix formation and denaturation, i.e. melting. Since C-G base-pairs are more stable than A-T pairs, DNA helices with a high C-G content are energetically preferred to those rich in A-T.

The effect of base-stacking energy, associated with sequence dependence, revealed that $^{5'}$pyrimidine-purine$_{3'}$ is more stable than $^{5'}$purine- pyrimidine $_{3'}$ (Saenger, 1984a). T_m also increases with increased ionic strength of the medium and DNA chain length. However, both the ionic strength (50 mM NaCl and 40 mM sodium cacodylate in D_2O) and the deoxyoctanucleotide chain length are constant parameters in this study.

Figure 5
Denaturing Polyacrylamide Gel

where B ⇒ bromophenol blue (indicative of a deoxyoctanucleotide)
1 ⇒ d(CGCATGCG).d(CGCATGCG)
2 ⇒ d(CGCTAGCG).d(CGCTAGCG)
3 ⇒ d(CGTATACG).d(CGTATACG)
4 ⇒ d(CGATATCG).d(CGATATCG)
5 ⇒ d(CGAATTCG).d(CGAATTCG)
6 ⇒ d(CGCGTGCG).d(CGCGTGCG)
7 ⇒ d(CGCGCGCG).d(CGCGCGCG)

Therefore the parameters influencing the T_m are the C-G content and the sequence, with the following order of stability expected: d(CGCGCGCG).d(CGCGCGCG) > d(CGCGTGCG).d(CGCGTGCG) > d(CGCATGCG).d(CGCATGCG) > d(CGCTAGCG). d(CGCTAGCG) > d(CGATATCG).d(CGATATCG) > d(CGTATACG).d(CGTATACG) > d(CGAATTCG).d(CGAATTCG). The expected trend is consistent with experiment, except for the mismatch base-pair, d(CGCGTGCG).d(CGCGTGCG), and d(CGAATTCG). d(CGAATTCG). The former did not show sharp cooperative melting. Perhaps the G-T mismatch base-pair destabilized the duplex to a large extent even though it has a high C-G content. The "Drew-type" sequence, (CGAATTCG).d(CGAATTCG) (Dickerson, 1990), had a T_m higher than anticipated.

Table 2
Melting Temperature (T_m)

Deoxyoctanucleotide Sequences	% (C-G)	Melting Temperature (T_m) (°C)
d(CGCGCGCG).d(CGCGCGCG)	100.0	56.0
d(CGCGTGCG).d(CGCGTGCG)	87.5	25.0*
d(CGCATGCG).d(CGCATGCG)	75.0	35.3
d(CGCTAGCG).d(CGCTAGCG)	75.0	27.5
d(CGATATCG).d(CGATATCG)	50.0	25.0
d(CGTATACG).d(CGTATACG)	50.0	24.0
d(CGAATTCG).d(CGAATTCG)	50.0	27.5

* no sharp cooperative melting was observed

All the deoxyoctanucleotides exist as double helices in aqueous solution (40 mM sodium cacodylate and 50 mM NaCl in D_2O) as characterized by the usual T_m, UV and ECD measurements. UV and ECD measurements are discussed further in Chapter 4.

3. Daunorubicin

3.1 Introduction

Daunorubicin, also referred to as daunomycin, was isolated from *Streptomyces peucetius* in 1963 (Arcamone, 1981a). It is the prototype anthracycline antibiotic whose structure consists of a tetracycline aglycone, daunomycinone, attached to an amino-sugar, daunosamine, by a glycosidic linkage (see Figure 6). A prerequisite for activity in daunorubicin is the coupling of a coplanar hydrophobic region (anthraquinone) with an angled hydrophilic structure (OH groups and protonated amino sugars), while the quinone and hydroquinone moieties on adjacent rings allow them to function as electron accepting and donating agents. Daunorubicin, pharmaceutically referred to as Cerubidine, is clinically used for the treatment of acute lymphocytic leukemia. It is an intercalator with complex groove-binding substituents (Pindur *et al.*, 1993).

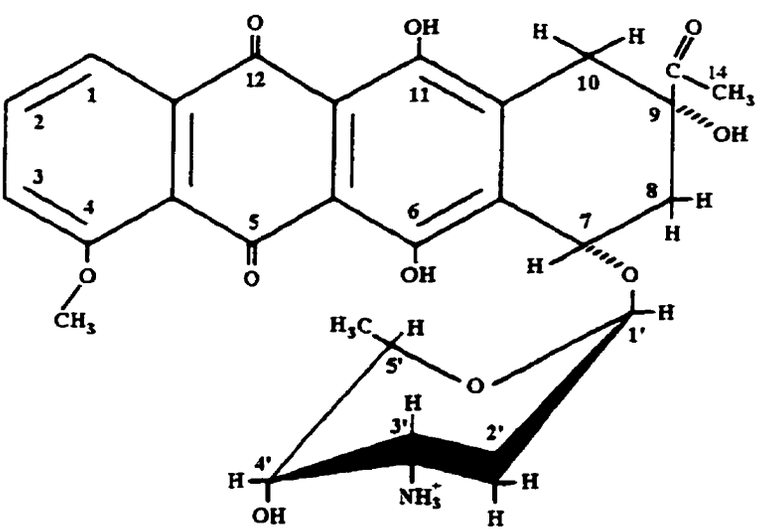

Figure 6
Chemical Structure of Daunorubicin

3.2 Mode of Action

Daunorubicin binds to DNA by the process of intercalation where an anthraquinone skeleton (chromophore) inserts between two stacked base-pairs. Optimal intercalation is achieved when the intercalator possesses a polarizable planar aromatic chromophore with three or four fused rings. The primary and secondary structures of DNA remain unchanged upon intercalation, however, the tertiary helical structure is lengthened and concurrently unwound in comparison to the original DNA. The average separation between base-pairs increases from 3.4 to 6.8 Å. Daunorubicin intercalates via the minor groove, with its chromophore aligned almost perpendicular to the long axis of adjacent base-pairs. The stability of the complex is enhanced by the hydrogen bonds between the phosphate groups and the terminal amino and hydroxyl groups of daunosamine, which lies in the minor groove of DNA, while the methoxy group of the chromophore protrudes into the major groove. Significant changes occur in DNA duplex conformations in order to accommodate daunorubicin, namely, the torsion angles between the sugar-phosphate skeleton, sugar puckering, torsions of the glycosidic angle (χ), the phosphoric ester angle (β) and the "unwinding" angle of the helix (α). Single crystal X-ray structure analyses in conjunction with molecular calculations have revealed that the major contribution to intercalation in DNA emanate from electrostatic, van der Waals and, in *vitro*, hydrophobic forces of interaction (Pindur *et al.*, 1993; Kennard & Hunter, 1991; Neidle, 1984).

The cationic daunosamine substituent essentially fills the minor groove, displacing water molecules and ions from it. Accordingly, the neighbor exclusion principle attributed to both conformational and electrostatic forces (McGhee & von Hippel, 1974; Crothers, 1968) is exhibited by inhibiting the intercalation of a further daunorubicin molecule per three base-pairs. Consequently, the selected deoxyoctanucleotides can intercalate a maximum of two daunorubicin molecules per deoxyoctanucleotide. An analytical expression which reflects the neighbor exclusion principle permits the convenient

extraction of the binding constant and the exclusion parameter from experimental data by nonlinear least-squares fitting procedures, given by Equation 3 (McGhee & von Hippel, 1974):

$$\frac{r}{C_f} = K(1 - nr)\left[\frac{1 - nr}{1 - (n-1)r}\right]^{n-1} \quad (3)$$

where r denotes the molar ratio of bound drug to total DNA base-pair, C_f the free drug concentration, K the binding constant for the interaction of drug with an isolated base-pair binding site and n the exclusion parameter. For example, K and n were estimated from fluorescence and absorbance titration experiments, for the interaction of daunorubicin with DNA of varying C-G content, illustrated in Table 3 (Chaires *et al.*, 1987).

Table 3
Estimates of Binding Constants and Exclusion Parameters for Interactions of Daunorubicin with DNAs of Varying C-G Content

% C-G	[†] K (x 10^5 M^{-1})	[*] n (base-pair)
100	37.0	2.8
72	15.0	3.1
50	7.1	3.3
42	6.6	3.6
31	3.9	3.0

Data taken from Chaires *et al.*, 1987.

[†] Error estimates of 15-20 % have been assigned to values of K.

[*] Error estimates of 10 % have been assigned to values of n.

The thermodynamic profile of the daunorubicin-DNA interaction was obtained by calorimetric measurements where the temperature dependence of the binding constant

was monitored. Enthalpy and entropy contributions to the binding free energy were determined from the Gibbs free energy relation, given by Equation 4:

$$\Delta G^\circ = -RT \ln K = \Delta H^\circ - T\Delta S^\circ \quad (4)$$

Daunorubicin binding to DNA was shown to be driven by a large, negative van't Hoff enthalpy term, i.e. it is energetically favored rather than by entropy (Chaires, 1990).

Kinetic studies indicate that daunorubicin binding to DNA is slow and complex. The lifetime of the daunorubicin-DNA complex was found by stop flow experiments to be comparatively long, about 1 s, in keeping with the clinical effectiveness of the drug, i.e. the complex forms a physical barrier that exists long enough to disrupt DNA replication and transcription processes. The kinetic complexity of daunorubicin has been postulated to arise from transient intermediates and multiple binding pathways where branched mechanisms are preferred, whereas the kinetic complexity of the binding process was suggested to arise from daunorubicin binding to specific classes of sites that differ in sequence or conformation (Chaires, 1990).

3.3 Physiological Aspects

The changed DNA topology effected by the intercalation of daunorubicin inhibits DNA replication and transcription which stops cell proliferation thereby categorizing daunorubicin as a cytostatic agent. Topoisomerase II is an enzyme responsible for cleaving, unwinding and rejoining segments of DNA, which are processes required for DNA and RNA synthesis. Daunorubicin is a potent inhibitor of topoisomerase II and forms a cleavable ternary complex with the enzyme and DNA.

Daunorubicin is administered intravenously and metabolized in the liver. Acute toxicities include total loss of hair, nausea, vomiting, local tissue necrosis due to leakage of the drug from the injection site. A chronic toxicity of daunorubicin is cardiomyopathy, damage to heart muscle manifested by an often irreversible decrease in the ability of the

heart to pump (Krogh, 1995). The metabolism of the daunorubicin quinone ring yields semiquinone radical intermediates which rapidly react with oxygen to produce superoxide anion radicals. These can generate both hydrogen peroxide and hydroxyl radicals, which are highly destructive to cells. Free-radical formation is suggested to contribute to cardiac toxicity. There are continued efforts to find structural analogues of daunorubicin with reduced toxicity and a wider spectrum of activity, e.g. epirubicin and mitoxantrone. The understanding of structure-activity relationships is therefore imperative (Suarato, 1990; Manfait *et al.*, 1984).

3.4 Sequence Specificity

Intercalation and groove-binding constitute the two major categories of anti-tumor drug interaction with DNA duplexes. The latter entails the drug binding directly to the edges of base-pairs in either of the minor or major grooves of DNA. Intercalating drugs have markedly less binding selectivity than groove-binding drugs. In a DNA complex the intercalation sites at A-T or C-G base-pairs have similar interaction potentials, while groove-binding drugs contact more base-pairs along the groove where the A-T and C-G regions are quite distinct (Wilson, 1990). Binding specificity depends on dipole interactions with polarizable intercalators, on hydrogen bonding interactions, on the size, hydration and electrostatic potential of the grooves.

Earlier literature on sequence dependence for daunorubicin intercalation was contradictory. For example, equilibrium studies on the interaction of daunorubicin with synthetic deoxypolynucleotides revealed a preference for sequences containing alternating A-T versus C-G base-pairs and for sequences of an alternating purine-pyrimidine structure (Chaires, 1983). The alternating purine-pyrimidine specificity is consistent with that revealed by ^{1}H and ^{31}P NMR studies of a synthetic deoxypolynucleotide consisting of alternating A-T base-pairs, complexed with daunorubicin (Patel *et al.*, 1981). More recent literature based on the interaction of daunorubicin with a series of natural DNA samples

of varying base composition indicates that alternating purine-pyrimidine sequences are preferred and the magnitude of the equilibrium binding constant (K) increases with increasing C-G content (see Table 3), thus implying that daunorubicin interacts preferentially with sites containing adjacent C-G base-pairs (Chaires *et al.*, 1987). It has also been noted that site preference is complex and involves more than a single base-pair. The C-G base-pair preference of daunorubicin is suggested to originate from the larger intrinsic dipole moment of C-G relative to A-T base-pairs and the subsequent ability of C-G base-pairs to induce polarization in the anthraquinone skeleton of daunorubicin (Pindur *et al.*, 1993; Wilson, 1990).

Computations performed on the energetics of daunorubicin intercalation with duplex deoxyhexanucleotides of varying sequence revealed that daunorubicin preferentially recognized a triplet sequence in the following descending order: 5′-TCG ≥ 5′-ACG > 5′-ATA >> 5′-GCG > 5′-GTA (Chen *et al.*, 1985; Chaires, 1990). Footprinting methods offer a high resolution procedure for mapping preferred antibiotic-binding sites on DNA in solution. Footprinting titration experiments using deoxyribonuclease I (Dnase 1), an enzymatic cleavage reagent, revealed preferential binding of daunorubicin to 5′-TCG, 5′-ACG, 5′-TGC and 5′-AGC sequences (Chaires *et al.*, 1990). The first two sequences are in keeping with the specificity predicted by the above mentioned theoretical studies. The proposition that daunorubicin recognizes a triplet sequence is consistent with the neighbor exclusion prediction from equilibrium binding studies where daunorubicin binds to a site containing three base-pairs. The C-G base-pair preference is sustained in the most preferred triplet sequences, viz. 5′-TCG and 5′-ACG, which are the identical sites to which daunorubicin is observed to be bound in the crystal studies of deoxyhexanucleotides (Frederick *et al.*, 1990; Wang *et al.*, 1987), indicating that those sites are energetically more favorable than the other available intercalation sites.

The crystal structures of d(CGTACG).d(CGTACG)-2(daunorubicin) at 1.2 Å resolution (Wang *et al.*, 1987) and d(CGATCG).d(CGATCG)-2(daunorubicin) at 1.5 Å resolution (Frederick *et al.*, 1990) show two daunorubicin molecules intercalated, one at each of the two terminal C-G sites of each duplex, with the amino-sugar lying in the minor groove. The C-G base-pairs on either side of daunorubicin undergo increased separation, are displaced relative to the helix axis in the direction of the minor groove and are significantly buckled, not propellor twisted, in the center of the base-pair. At the intercalation site there is no unwinding of base-pairs from the usual 36° helical twist but base-pairs at adjacent sites are unwound by 8° with an associated distortion of the backbone (Wang *et al.*, 1987). Such long range induced conformational changes emphasize the flexibility of DNA.

3.5 Experimental Details

The deoxyoctanucleotide-daunorubicin complexes are composed of a 2 to 1 ratio of daunorubicin to duplex deoxyoctanucleotide. Daunorubicin hydrochloride (90% purity) was purchased from Calbiochem, and used as provided. Its concentration was determined by measuring the absorbance at 475 nm in a 1 cm Quartz cuvette on a Cary3E Spectrophotometer, and an extinction coefficient of 9860 $M^{-1}cm^{-1}$ at 475 nm was used (Jorgenson, 1981). Daunorubicin, as quoted by one supplier, is light sensitive; therefore all experiments were conducted in the dark. A concentration of 40 mM daunorubicin buffered with 40 mM sodium cacodylate and 50 mM NaCl in D_2O constituted the free drug solution, whereas an addition of 20 mM duplex deoxyoctanucleotide formed the deoxyoctanucleotide-daunorubicin mixture. The mixture was allowed to stand for 6 hours to permit complexation. The reddish colored solutions were then lyophilized and resuspended to make a final volume of 0.1 ml in D_2O. Six deoxyoctanucleotide-daunorubicin complexes were prepared with the deoxyoctanucleotides shown in Figure 4 on page 12, with the exception of the mismatch sequence. The measurement of the

IR/VCD spectra of the free daunorubicin and the deoxyoctanucleotide-daunorubicin complexes is analogous to that of the free deoxyoctanucleotides, described in Chapter 4.

3.6 Discussion

Solution, X-ray crystallographic and theoretical studies provide a consistent and coherent conception of the sequence preference of daunorubicin. The reported 1 s lifetime of the daunorubicin-DNA complex suggests that it might be long enough to observe intermediates during the IR/VCD spectral measurements. However, the possibility of separate transition species showing different VCD features is unknown at this stage.

IR and Raman spectra of a closely related antibiotic, adriamycin, have been reported (Suarato, 1990; Pohle & Flemming, 1985). Structurally adriamycin (14-hydroxyl-daunorubicin) differs only slightly from daunorubicin but clinically the difference is vast (Arcamone, 1981a; Arcamone, 1981b). One of the primary objectives of this work was an investigation of whether VCD measurements provide any new information on DNA-drug interactions that were not feasible by other techniques. Daunorubicin constituted the drug of choice for accomplishing this objective because of the immense literature available on daunorubicin and DNA-daunorubicin complexes, and the fact that adriamycin is a derivative of daunorubicin. Consequently, this Chapter focused almost exclusively on daunorubicin.

4. Vibrational Circular Dichroism

4.1 Introduction

Vibrational circular dichroism (VCD) is a relatively new field of molecular spectroscopy which is exclusive to chiral molecules. Chiral (asymmetric and dissymmetric) molecules are not superimposable on their mirror images. They exhibit a differential interaction with left and right circularly polarized radiation, thereby rendering them optically active. Optical activity originates as a consequence of the three-dimensional arrangement of molecular constituents, hence the spectroscopic results correlate directly to the structures of the molecules, e.g. enantiomeric (mirror-image pair) molecules display circular dichroism (CD) spectra of equal intensity and opposite sign. X-ray crystallography is another method that provides stereospecific information. However, it is specific to single crystals whose conformation can differ markedly from those in solution.

CD, the difference in absorbance of left versus right circularly polarized light, can occur for both electronic and vibrational excitations of a chiral molecule. VCD spectra by their nature provide more detail than their parent absorption spectrum, and also contain new information regarding the conformation and absolute molecular configuration (Nafie & Freedman, 1987). Electronic circular dichroism (ECD) is extensively used to derive stereochemical information of proteins and nucleic acids (Sheardy, 1991; Sprecher & Johnson, 1977; Bush, 1974). There are a limited number of allowed UV transitions which correspond to relatively delocalized excitations of the molecules, often resulting in broad and overlapping UV spectral bands (Keiderling *et al.,* 1989). VCD has the potential to be a more powerful stereospecific analytical tool than ECD, since the vibrational spectrum ideally comprises as many transitions as the 3N-6 degrees of freedom to describe a molecule. CD arises from dipolar interactions where the intensity of a CD band depends on the magnitudes and relative orientations of the dipole transition moments. Since the dipole strengths of electronic transitions may be an order of magnitude greater than those

of vibrational transitions, their interactions are stronger and extend over greater distances. In the case of a deoxypolynucleotide, ECD is capable of monitoring greater lengths than VCD. The latter offers the possibility of studying relatively localized regions, a few neighboring nucleotides in a typical nucleic acid (Diem, 1991).

4.2 Theory

The theoretical basis for VCD is discussed comprehensively elsewhere (Nafie & Freedman, 1987; Rauk, 1991). The following synopsis is derived from these references. Experimentally one measures the difference in absorption (ΔA_{CD}) of an optically active molecule as a function of wavenumber:

$$\Delta A_{CD}(\bar{\nu}) = A_L(\bar{\nu}) - A_R(\bar{\nu}) \tag{5}$$

where A_L and A_R are the absorbance of the left and right circularly polarized infrared radiation, respectively. The VCD measurement is fairly difficult since the difference signal, ΔA_{CD}, is approximately three to five orders of magnitude lower than either A_L or A_R.

The VCD intensity of a fundamental vibrational transition between v = 0 and 1 levels of the a^{th} normal vibrational mode is determined in the harmonic approximation by the rotational strength, R_{01}^{a}:

$$\begin{aligned} R_{01}^{a} &= I_m\left[(\bar{\mu})_{01}^{a} \cdot (\bar{m})_{10}^{a}\right] \\ &= \frac{h}{4\pi c}\left(\frac{\partial \bar{\mu}}{\partial \bar{Q}_a}\right)_0 \cdot \left(\frac{\partial \bar{m}}{\partial \bar{P}_a}\right)_0 \\ &\propto \int_0^{\infty} \frac{\Delta A_{CD}(\bar{\nu})}{\bar{\nu}} \partial\bar{\nu} \end{aligned} \tag{6}$$

where h is Planck's constant; I_m refers to the imaginary part of the scalar product; $(\bar{\mu})_{01}^{a}$ and $(\bar{m})_{10}^{a}$ are the electric and magnetic transition matrix elements, respectively,

between v = 0 and 1 levels of the a[th] normal mode; $\left(\frac{\partial\bar{\mu}}{\partial\bar{Q}_a}\right)_0$ and $\left(\frac{\partial\bar{m}}{\partial\bar{P}_a}\right)_0$ are the atomic polar tensor (APT) and the atomic axial tensor (AAT) elements, respectively. These derivatives are calculated with respect to the normal coordinate of position, $\bar{Q}_a$, and conjugate momentum, $\bar{P}_a$. The electric and magnetic dipole moment operators, $\hat{\mu}$ and $\hat{m}$, respectively, are the sums of the electron and nuclear operators:

$$\hat{\mu} = \hat{\mu}^e + \hat{\mu}^n = -\sum_i^{\text{electrons}} e\bar{r}_i + \sum_I^{\text{nuclei}} Z_I e\bar{R}_I \tag{7}$$

and

$$\hat{m} = \hat{m}^e + \hat{m}^n = -\sum_i^{\text{electrons}} \frac{e}{2mc}\bar{r}_i \times \bar{p}_i + \sum_I^{\text{nuclei}} \frac{Z_I e}{2M_I c}\bar{R}_I \times \bar{P}_I \tag{8}$$

where e, m, $\bar{r}_i$, and $\bar{p}_i$, represent the charge, mass, position, and momentum of the i^{th} electron, respectively; $Z_I e$, M_I, $\bar{R}_I$, $\bar{P}_I$, are the charge, mass, position and momentum of the I^{th} nucleus, respectively; and c is the speed of light.

The conventional infrared absorption intensity for the same vibrational transition is determined by the dipole strength, D_{01}^a:

$$\begin{aligned} D_{01}^a &= \left|(\bar{\mu})_{01}\right|^2 \\ &= \frac{h}{4\pi\omega_a}\left|\left(\frac{\partial\bar{\mu}}{\partial Q_a}\right)_0^a\right|^2 \\ &\propto \int_0^\infty \frac{A(\bar{\nu})}{\bar{\nu}}\,\partial\bar{\nu} \end{aligned} \tag{9}$$

where ω_a is the angular wavenumber of the a[th] normal mode and A is absorbance of unpolarized light.

Experiment and theory can be compared through the anisotropy ratio (dissymmetry factor), given by:

$$g_{01}^{a} = \frac{4R_{01}^{a}}{D_{01}^{a}} = \frac{\Delta\varepsilon_{CD}}{\varepsilon} \qquad (10)$$

where ε is the extinction coefficient. This ratio defines the intensity and sign of a VCD band relative to is parent absorption intensity. The difficulty in measuring the VCD of a given band increases as the anisotropy ratio diminishes.

Conventional IR intensities are proportional to the square of the electric dipole transition moments (see Equation 9), while VCD intensities are derived from the scalar product of the electric and magnetic dipole transition moments (see Equation 6). Consequently, positive VCD features result when the two transition moments form angles less than 90°, whereas angles greater than 90° result in negative VCD features. In achiral molecules either one of the moments is zero, both of them are zero or orthogonal to each other and no VCD features arise. Knowledge of the relative orientations of the electric and magnetic dipole transition moments is therefore essential for predicting the sign of the VCD band for a particular vibration. VCD features can be predicted by various approximate models or by quantum mechanical, *ab initio*, methods. These are discussed in detail elsewhere (Freedman & Nafie, 1987; Rauk, 1991; Yang & Rauk, 1996).

The characteristic bisignate VCD features, i.e. bands with alternating signs of equivalent intensities, suggest a coupled oscillator mechanism (Rauk & Freedman, 1994; Tinoco, 1963; Holzwarth & Chabay, 1972), discussed in detail in Chapter 5. In this approximate model approach, the in- and out-of-phase vibrations of two identical, chirally oriented oscillators give rise to a VCD couplet. Such couplets arise from dipolar interactions which split the wavenumber of the in- and out-of-phase modes (Nafie & Freedman, 1987).

4.3 Literature Survey

VCD spectroscopy has been very successful for small organic molecules, both experimentally and computationally (Rauk, 1991; Yang & Rauk, 1996). This new insight has encouraged the application of VCD to molecules of biological interest, which has proven effective for detecting conformational changes and for characterizing secondary structures in polypeptides, proteins and nucleic acids in solution. Several empirical and theoretical studies are reported in the literature (Keiderling & Pancoska, 1993; Zhong *et al.*, 1990; Gulotta *et al.*, 1989). Most peptide investigations are conducted in the amide A (N-H stretch), amide I (C=O stretch) and amide II (mixture of C-N stretch and H-N-C bend) regions. The bisignate amide A bands are consistently opposite in sense to that of the amide I for right-handed α-helices in non-aqueous solution but these modes are not observed for samples in aqueous solution (Lal & Nafie, 1982). The sense of these bisignate couplets reflect the handedness of the α-helix and not the configuration of the constituent amino acid residues. The amide II band exhibits monosignate VCD features which are also diagnostic for α-helical structures (Sen & Keiderling, 1984).

Biochemical research has been directed towards the resolution of the secondary structure and folding of proteins in solution. A preliminary requirement is the determination of the protein composition in terms of α-helix, β-sheet and random-coil content. Since VCD features of large molecules (like proteins) are overlapped, statistical approaches are adopted to correlate the spectra with the structure (Pancoska *et al.*, 1991; Pancoska & Keiderling, 1991). This approach utilizes the VCD spectra of polypeptides containing α-helices, β-sheets or random-coils exclusively, as basis sets which are linearly combined to fit the observed VCD spectrum of a protein. The resulting coefficients of the basis set infer the structural composition of the protein.

A theoretical and experimental VCD study of a cyclic pentapeptide (Wyssbrod & Diem, 1992) disclosed characteristic VCD signatures which were indicative of the β-turn

contained in fractions of the molecule. VCD conformational studies of a cyclic hexapeptide and its complexes with cations (Xie & Diem, 1995) showed that VCD is a powerful conformational probe for small peptides in solution, thereby emphasizing the diagnostic ability of VCD for biomolecules. VCD results, in comparison to ECD, also exhibit enhanced sensitivity to various globular protein conformations (Pancoska *et al.*, 1989).

The application of VCD to proteins has been extended to nucleic acids. A comparative study of ribonucleic acids (RNA) in aqueous solution (Annamalai & Keiderling, 1987) revealed that mononucleotides gave no significant VCD in comparison to the polymers which generally displayed larger, bisignate VCD signals in the 1750-1550 cm^{-1} region associated with carbonyl stretching modes. Variations in the VCD magnitude and band shape were correlated with base stacking, base-pairing and the degree of order. A VCD study of the thermal denaturation of double-stranded poly(rA).poly(rU) (Yang & Keiderling, 1993) showed a helix-to-coil transition at temperatures greater than 54°C, with the resulting single-strand (coil) retaining some local order to 80°C. The results were qualitatively explained with dipolar coupling between relatively isolated bases thus signifying the immense capability of VCD for studying conformational transitions of biopolymers.

VCD studies of the A to B conformational transition in DNA (Wang & Keiderling, 1992) in the 1700-1550 cm^{-1} spectral region showed subtle changes in the VCD signal. The B-form showed broader, less intense VCD bands than the A-form, i.e. a B to A conformational transition is accompanied by an intensifying and sharpening of the VCD band in the carbonyl stretching region. This VCD occurrence is sequence dependent, C-G versus A-T content, in contrast to ECD where a much smaller difference in the bandshape is observed. VCD displays more sensitivity to sequence than ECD since the VCD spectrum reflects the coupling of local oscillators, particularly the C=O stretches, which

differ for each base, whereas the ECD spectrum senses coupling of the π-electron systems, which have intrinsic similarities among the bases (Pancoska *et al.*, 1989; Wang & Keiderling, 1992). VCD characteristics of the A-form of DNA is consistent with those of RNA due to the similarity of their structures (Wang & Keiderling, 1992).

The B to Z phase transition in deoxyoligonucleotides (Gulotta *et al.*, 1989; Keiderling *et al.*, 1989; Diem, 1991) revealed a sign change in the VCD signal, as predicted when the sense of the helices change. Thus the B to Z transition in DNA is more pronounced than the A to B transition (Wang & Keiderling, 1992) in the carbonyl stretching region, both experimentally and computationally using the coupled oscillator model. This inversion is also evident in the VCD spectra of the PO_2^- stretching region (1300-1000 cm^{-1}) (Wang *et al.*, 1994b), which is representative of the change in the helical sense of the nucleic acid backbone. The VCD spectra of the symmetric PO_2^- stretching vibration (1150-1000 cm^{-1}) is invariant to base sequence in contrast to that found for the C=O stretching and other skeletal modes of the bases, an effect displayed by NMR spectroscopy.

Experimental and theoretical VCD results for B-family polymers (Zhong *et al.*, 1990) allowed quantitative interpretation of the carbonyl stretching region in terms of the coupled oscillator model. Triple-helical pyrimidine-purine-pyrimidine nucleic acids were detected and characterized with VCD in the carbonyl stretching region (Wang *et al.*, 1994a), where the VCD spectra of the triplexes differed from their corresponding duplexes. The VCD spectra of deoxydinucleotides containing C and G were observed (Birke & Diem, 1995). Their qualitative agreement with calculated VCD spectra suggested that the deoxydinucleotides occur in a solution conformation that correspond to d(CG).d(CG) and d(GC).d(GC) sequences in poly(dG-dC).poly(dG-dC). VCD spectra have also been obtained for self-complementary deoxytetranucleotides, d(CGCG).d(CGCG), d(GCGC). d(GCGC), d(CCGG).d(CCGG) and d(GGCC).d(GGCC) (Birke *et al.*, 1993).

It should also be pointed out at this stage that there has been extensive work done on the IR and Raman of DNA (Wang *et al.*, 1987; Nishimura & Tsuboi, 1986; Taillandier *et al.*, 1985; Tsuboi *et al.*, 1973; Tsuboi, 1974) and DNA-drug complexes (Broyde *et al.*, 1981; Manfait & Theophanides, 1986; Missailidis & Hester, 1995; Manfait *et al.*, 1981; Manfait *et al.*, 1984). This work is acknowledged but a literature review in this regard is beyond the scope of this thesis.

4.4 Spectroscopy Experiments

4.4.1 FT-VCD Instrument

Experimental techniques for measuring VCD spectra of biopolymers were reviewed in recent publications (Keiderling, 1990; Keiderling & Pancoska, 1993; Freedman & Nafie, 1993). VCD can be measured with either a dispersive or a Fourier Transform instrument. The latter is unique for measuring continuous regions in the IR spectrum, e.g. 1750-850 cm^{-1} in this study.

In our laboratory we use a Bomem MB100 interferometer as the basic instrument, equipped with the additional components necessary for VCD measurements (Tsankov *et al.*, 1995) as illustrated in Figure 7. Beginning with the optical components of the VCD instrument, light leaves the FTIR interferometer through the side port and consecutively passes through a linear polarizer, a ZnSe photoelastic modulator (Hinds International), the sample contained in a cooling jacket, a ZnSe lens (which focuses the light onto the detector window), an optical filter (Optical Coating Laboratory, Inc.) and a Mercury-Cadmium-Tellurium (MCT) detector (Bevlov Technology). The MCT detector selected for improved sensitivity is cooled with liquid nitrogen. The electronic components of the VCD instrument are encountered when the signal, upon preamplification, is split into two pathways. The first pathway conveys the conventional infrared transmission, designated dc, and the second the differential transmission, designated ac. The ac signal is demodulated with a lock-in amplifier operating at the PEM

frequency of 37 kHz. Electronic filters demodulate the Fourier frequency from the modulated frequency. The ac and dc transmission spectra are collected and stored separately, then ratioed to give the VCD spectra $\left(\frac{\Delta A_{CD}}{A}\right)$.

The intensity of the experimental VCD spectra is given by (Nafie & Diem, 1979):

$$\frac{I_{AC}(\bar{\nu})}{I_{DC}(\bar{\nu})} = I_{CD}(\bar{\nu}) = 2J_1\left[\alpha_0(\bar{\nu})\right](1.15)\,\Delta A_{CD}(\bar{\nu}) \qquad \textbf{(11)}$$

where the factor $2J_1\left[\alpha_0(\bar{\nu})\right]$ accounts for the efficacy of the modulator to produce circularly polarized radiation at various wavenumbers. The angle $\alpha_0(\bar{\nu})$ corresponds to the maximum retardation amplitude achieved by the modulator at a given wavenumber during the course of its oscillation cycle. The value of $J_1\left[\alpha_0(\bar{\nu})\right]$ can be determined by calibration measurements described elsewhere (Tsankov *et al.*, 1995).

The FT-VCD instrument described has the capability of successfully measuring VCD spectra in the continuous 1750-850 cm^{-1} region. The impediments to recording VCD spectra outside this region are incurred by cutoffs of the ZnSe lens and PEM at 800 cm^{-1}, the optical filter which prevents detector saturation and the PEM transmission envelope at 1750 cm^{-1}, and the detector at 750 cm^{-1}.

4.4.2 IR/VCD of Deoxyoctanucleotides

The selected deoxyoctanucleotide samples at 20 mM duplex in D_2O/cacodylate buffer solution, at pD 7.3, were contained in a 25 μm BaF_2 liquid cell (International Crystal Laboratories, Inc.) and maintained at a constant temperature of 4°C in a variable temperature chamber. For these experiments 7500 ac scans were acquired in 165 min and ratioed against 750 dc scans, both at a resolution of 4 cm^{-1}. The resulting VCD spectra were corrected for polarization artifacts by subtracting the spectra of the solvent (40 mM

sodium cacodylate and 50 mM NaCl in D_2O), recorded with the same instrumental conditions. The noise estimate, which gives the reliability of the VCD signal, was obtained by subtracting two consecutively recorded VCD spectra of the same sample (solvent-subtracted) and dividing the resulting background by two (Maharaj *et al.*, 1995).

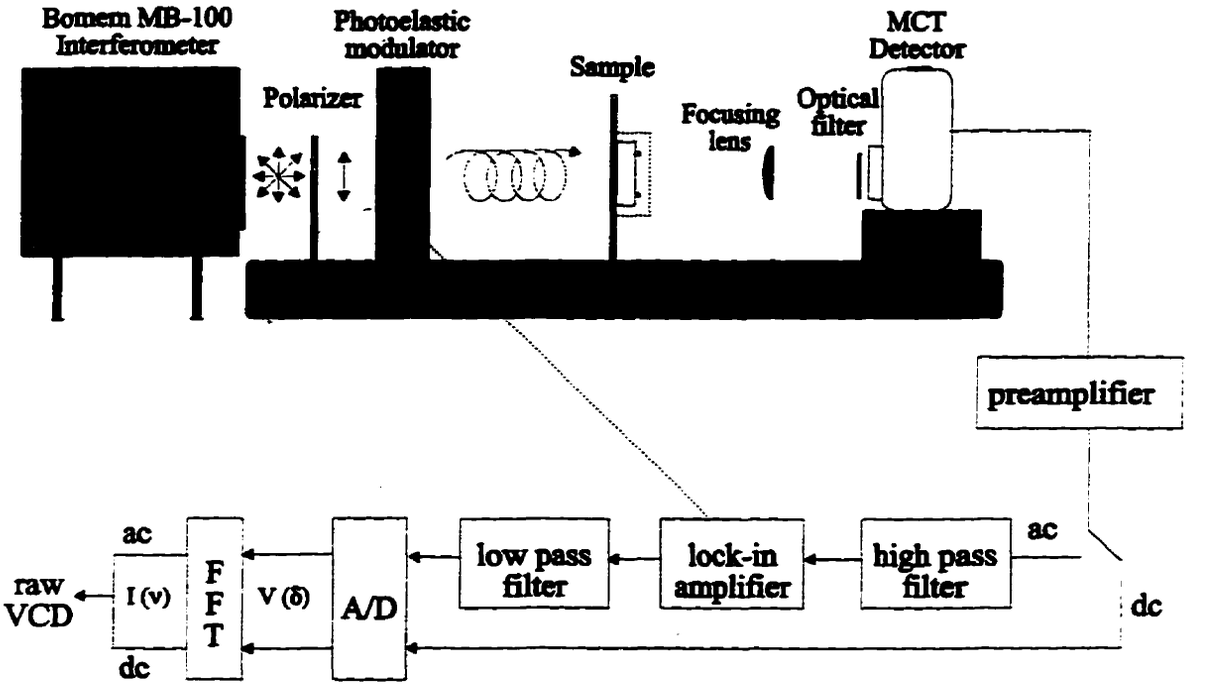

Figure 7
Optical and Electronic Components of the VCD Instrument

4.4.3 UV/ECD of Deoxyoctanucleotides

The deoxyoctanucleotide samples at 0.02 mM duplex in D_2O/cacodylate buffer solution, at pD 7.3, were contained in a 5 mm Quartz cuvette, and maintained at a constant

temperature of 4°C. The UV measurements were conducted on a Cary3E spectrophotometer, while a Jasco J-715 spectropolarimeter was used for the ECD measurements.

4.4.4 IR/VCD Deoxyoctanucleotide-Daunorubicin Complexes

Daunorubicin at 40 mM in D_2O/cacodylate buffer solution and the deoxyoctanucleotide-daunorubicin complexes at a 2 to 1 ratio (40 mM daunorubicin and 20 mM duplex) in D_2O/cacodylate buffer solution, at pD 7.3, were contained in a 25 μm BaF_2 liquid cell (International Crystal Laboratories, Inc.) and maintained at a constant temperature of 4°C in a variable temperature chamber. These experiments, apart from being carried out in the dark, were identical to those of the free deoxyoctanucleotides.

4.5 Results and Discussion

The IR absorption/FT-VCD spectra of daunorubicin, the selected deoxyoctanucleotides (Figure 4, page 12) and their daunorubicin complexes were measured in D_2O buffered at pD 7.3 with sodium cacodylate in the region of 1750 to 850 cm^{-1}. The UV absorption/ECD spectra of the selected deoxyoctanucleotides were also measured in D_2O buffered at pD 7.3 with sodium cacodylate in the region of 25000 to 55000 cm^{-1} and these spectral results are discussed in conjunction with their simulated counterparts in Chapter 5.

This work demonstrates the first successful attempt at recording FT-VCD of deoxyoctanucleotides and their daunorubicin complexes in the continuous region of 1750-850 cm^{-1}. While the spectra are generally complex with broad and overlapping bands especially for absorption, the advantage of VCD is clearly evident with positive and negative features that enhance resolution as well as identify specific vibrational modes. The infrared absorption and the VCD spectra generally correspond to one another.

Characteristic VCD bands with high signal-to-noise ratios are indeed observed in both the selected deoxyoctanucleotides (see Figure 8, page 44 to Figure 14, page 50) and the deoxyoctanucleotide-daunorubicin complexes (see Figure 16, page 55 to Figure 21, page 60) but not in daunorubicin (see Figure 15, page 51). The remarkably good noise estimates suggest that even the small VCD features are reliable. However, in the region of solvent (D_2O) absorption the large noise estimates result from low energy reaching the detector. The most prominent features occur between 1750-1600 cm^{-1}, arising from carbonyl and/or skeletal stretching vibrations of the nucleotide bases. Minor peaks in the region of 1600-1450 cm^{-1} of deoxyoctanucleotides, assumed to result from the nucleotide bases, have not been reported previously. The PO_2^- symmetric stretching vibration of the phosphate backbone which occurs between 1100-1050 cm^{-1}, constitutes the second most prominent features. Conversely, the PO_2^- antisymmetric stretching vibration is obscured by D_2O absorbance. The VCD spectra also hint at the C-O stretching of the deoxyribose below 1050 cm^{-1}, however it is not clear enough to be diagnostic.

The nucleotide base modes appear to reveal sequence specificity in contrast to the phosphate backbone vibrations (Maharaj *et al.*, 1995). The two most prominent regions show bisignate VCD couplets, with negative VCD bands at higher wavenumber and positive VCD bands at lower wavenumber denoting a right-handed helix. The VCD intensity of the carbonyl and/or skeletal stretching vibrations of the nucleotide bases, in the region of 1750-1600 cm^{-1}, decreases and the bisignate VCD couplet diminishes with increasing base substitutions of the principal sequence, d(CGCGCGCG). d(CGCGCGCG).

4.5.1 Experimental IR/VCD Spectra of Deoxyoctanucleotides

The following qualitative comparisons are performed on the premise that the selected deoxyoctanucleotides have eight base-pairs with concentrations normalized to 20 mM:

a) d(CGCGCGCG).d(CGCGCGCG) (Figure 8, page 44)

The IR absorption and VCD spectra of the principal sequence, d(CGCGCGCG). d(CGCGCGCG), are the most intense of all the selected deoxyoctanucleotides in the 1750-1500 cm^{-1} region. The IR absorption band at 1683 cm^{-1} and the corresponding VCD couplet at 1692(-)/1678(+) cm^{-1} dominates in both spectra. Its assignment to the carbonyl and/or skeletal stretching vibrations of the C-G base-pair is assured by comparison with the deoxypolynucleotide, poly(dG-dC).poly(dG-dC) (Zhong *et al.*, 1990) and the deoxytetranucleotide, d(CGCG).d(CGCG) (Birke *et al.*, 1993) with their IR absorption bands at 1685 cm^{-1} and their respective VCD couplets at 1700(-)/1670(+) and 1694(-)/1679(+) cm^{-1}. The deoxytetranucleotide has an additional IR absorption band at 1652 cm^{-1} with an associated VCD couplet at 1658(-)/1650(+) cm^{-1} (Birke *et al.*, 1993), which is similar to the deoxyoctanucleotide, d(CGCGCGCG).d(CGCGCGCG), whose IR absorption band at 1650 cm^{-1} gives rise to a VCD couplet at 1655(-)/1647(+) cm^{-1}. VCD couplets of interest in the deoxyoctanucleotide also include those at 1570(+)/1555(-), 1508(+)/1498(-) and 1089(-)/1072(+) cm^{-1}, which correspond to IR absorption bands at 1564, 1504 and 1087 cm^{-1}, respectively. The last mentioned VCD couplet is attributed to the symmetric PO_2^- stretching vibration in the sugar-phosphate backbone of the deoxyoctanucleotides (Wang *et al.*, 1994b).

b) d(CGCGTGCG).d(CGCGTGCG) (Figure 9, page 45)

The IR absorption and VCD spectra of d(CGCGTGCG).d(CGCGTGCG) are similar to those for d(CGCGCGCG).d(CGCGCGCG) discussed in (a), except for the broadening of the IR absorption band at 1650 to 1658 cm^{-1} and the development of a discernible VCD couplet at 1645(-)/1633(+) cm^{-1}, which may be attributed to the presence of thymine. The study of d(CGCGTGCG).d(CGCGTGCG) was peripheral to attaining the overall objective of monitoring DNA-drug interactions and in view of the minor changes in the IR/VCD spectra, it was not subjected to further investigation in this work.

c) d(CGCATGCG).d(CGCATGCG) (Figure 10, page 46) and
d(CGCTAGCG).d(CGCTAGCG) (Figure 11, page 47)

The d(CGCATGCG).d(CGCATGCG) and d(CGCTAGCG).d(CGCTAGCG) sequences have the most intense VCD couplets at 1692(-)/1674(+) and 1089(-)/1072(+) cm^{-1} corresponding to IR absorption bands at 1681 and 1087 cm^{-1}, respectively, which are essentially the same positions as in the principal sequence. This occurrence, in addition to the IR absorption bands at 1564 and 1504 cm^{-1} affiliated with the VCD couplets at 1570(+)/1555(-) and 1508(+)/1498(-) cm^{-1}, respectively, are comparable to those of d(CGCGCGCG).d(CGCGCGCG) discussed in (a), perhaps as a consequence of the high C-G base-pair content (75%).

d(CGCATGCG).d(CGCATGCG), in contrast to d(CGCTAGCG).d(CGCTAGCG), constituting a regular alternating $^{5'}$pyrimidine-purine$_{3'}$ sequence with a less intense VCD couplet at 1692(-)/1674(+), a sharper IR absorption band at 1648 cm^{-1} with a corresponding VCD couplet at 1653(+)/1644(-) cm^{-1}, a possible shoulder at 1699(-?) cm^{-1}, a less noticeable VCD couplet at 1507(+)/1497(-) cm^{-1}, and apparently better resolved VCD features at about 1060(+) cm^{-1}. VCD couplets at 1675(-)/1650(+), 1640(+)/1625(-) cm^{-1} and a (-)/(+) couplet centered at about 1700 cm^{-1} have been reported for the alternating poly(dA-dT).poly(dA-dT) and the homologous poly(dA).poly(dT), which does not contain the last mentioned couplet (Zhong *et al.*, 1990). These reported VCD couplets cannot be identified uniquely in the either of these deoxyoctanucleotides.

d) d(CGATATCG).d(CGATATCG) (Figure 12, page 48) and
d(CGTATACG).d(CGTATACG) (Figure 13, page 49)

The d(CGATATCG).d(CGATATCG) and d(CGTATACG).d(CGTATACG) sequences have the most intense VCD couplets at 1699(-)/1667(+), 1639(+)/1617(-) and 1089(-)/1072(+) cm^{-1} corresponding to IR absorption bands at 1681, 1623 and 1087 cm^{-1},

respectively. The positions of the first two VCD couplets in addition to the VCD couplet at 1578(-)/1562(+) cm^{-1} associated with the IR absorption band at 1573 cm^{-1}, differ from those of d(CGCGCGCG).d(CGCGCGCG), perhaps as a consequence of the reduced C-G base-pair content (50%). Furthermore, the IR absorption band at 1087 cm^{-1} together with its affiliated VCD couplet at 1089(-)/1072(+) cm^{-1} has a much higher intensity than the principal sequence and those sequences with two A-T base-pair substitutions, discussed in (c).

d(CGTATACG).d(CGTATACG), in contrast to d(CGATATCG).d(CGATATCG), constituting a regular alternating $^{5'}$pyrimidine-purine$_{3'}$ sequence with a more intense IR absorption band at 1681cm^{-1}, a sharper IR absorption band at 1650 cm^{-1}, a possible shoulder in the VCD spectrum at 1690(-?), a visually less discernible VCD couplet at 1507(+)/1497(-) cm^{-1} and apparently better resolved VCD features at about 1060 cm^{-1}. The reported VCD couplet at 1640(+)/1625(-) cm^{-1} attributed to the A-T base-pair (Zhong *et al.*, 1990) discussed in (c), likely concurs with those at 1639(+)/1617(-) evident in both of these deoxyoctanucleotides.

e) d(CGAATTCG).d(CGAATTCG) (Figure 14, page 50)

This sequence is discussed separately, even though it has the same number of C-G and A-T base-pairs as those discussed in (d), because of its uniqueness in both the IR absorption and VCD spectra. d(CGAATTCG).d(CGAATTCG) has the weakest VCD spectrum of all the selected deoxyoctanucleotides in the 1750-1500 cm^{-1} region, however the IR absorption band at 1086 cm^{-1} corresponding to the VCD couplet at 1091(-)/1070(+) cm^{-1} have high intensities which are equivalent to those discussed in (d) for the analogous features. The other apparent VCD couplets of interest include 1702(-)/1684(+), 1675(-)/1665(+) and 1636(+)/1619(-) cm^{-1} corresponding to IR absorption bands at 1691, 1664 and 1623 cm^{-1}, respectively. The last mentioned VCD couplet is also evident in the sequences discussed in (d), and hence appears to agree with

the reported VCD couplet at 1640(+)/1625(-) cm^{-1} attributed to the A-T base-pair (Zhong *et al.*, 1990), discussed in (c). In contrast to d(CGATATCG).d(CGATATCG) and d(CGTATACG).d(CGTATACG) the 1507(+)/1497(-) cm^{-1} VCD couplet associated with the IR absorption band at 1503 cm^{-1} is very weak and there is no evidence of a VCD couplet corresponding to the IR absorption band at 1575 cm^{-1}.

4.5.2 Experimental IR/VCD Spectra of Daunorubicin

Daunorubicin at the same concentration as in the deoxyoctanucleotide-daunorubicin complexes exhibits a reasonably strong absorption spectrum with no apparent VCD features (see Figure 15, page 51) even though it has six chiral centers. The IR absorption band of daunorubicin at 1706 cm^{-1} can probably be attributed to the ketone, whereas the absorption band at 1617 cm^{-1} may be assigned to the antisymmetric stretching vibrations of the quinone carbonyl groups at $C_{(5)}$ and $C_{(12)}$ (see Figure 6, page 20) which are polarized in plane perpendicular to the long axis of daunorubicin, while the bands at 1587 cm^{-1} and 1557 cm^{-1} can be attributed to the resonance structures (Suarato, 1990).

4.5.3 Experimental IR/VCD Spectra of Deoxyoctanucleotide-Daunorubicin Complexes.

All deoxyoctanucleotide IR and VCD spectra appear to have somewhat reduced intensity upon intercalation of daunorubicin. In fact, the negative VCD features of the deoxyoctanucleotide-daunorubicin complexes show decreased intensity in the 1750-1600 cm^{-1} region when compared to the free deoxyoctanucleotides .

The effects on the IR absorption and VCD spectra upon intercalation with daunorubicin shall be discussed in the form of a qualitative comparison of the spectra of the free deoxyoctanucleotides and their daunorubicin complexes, as follows:

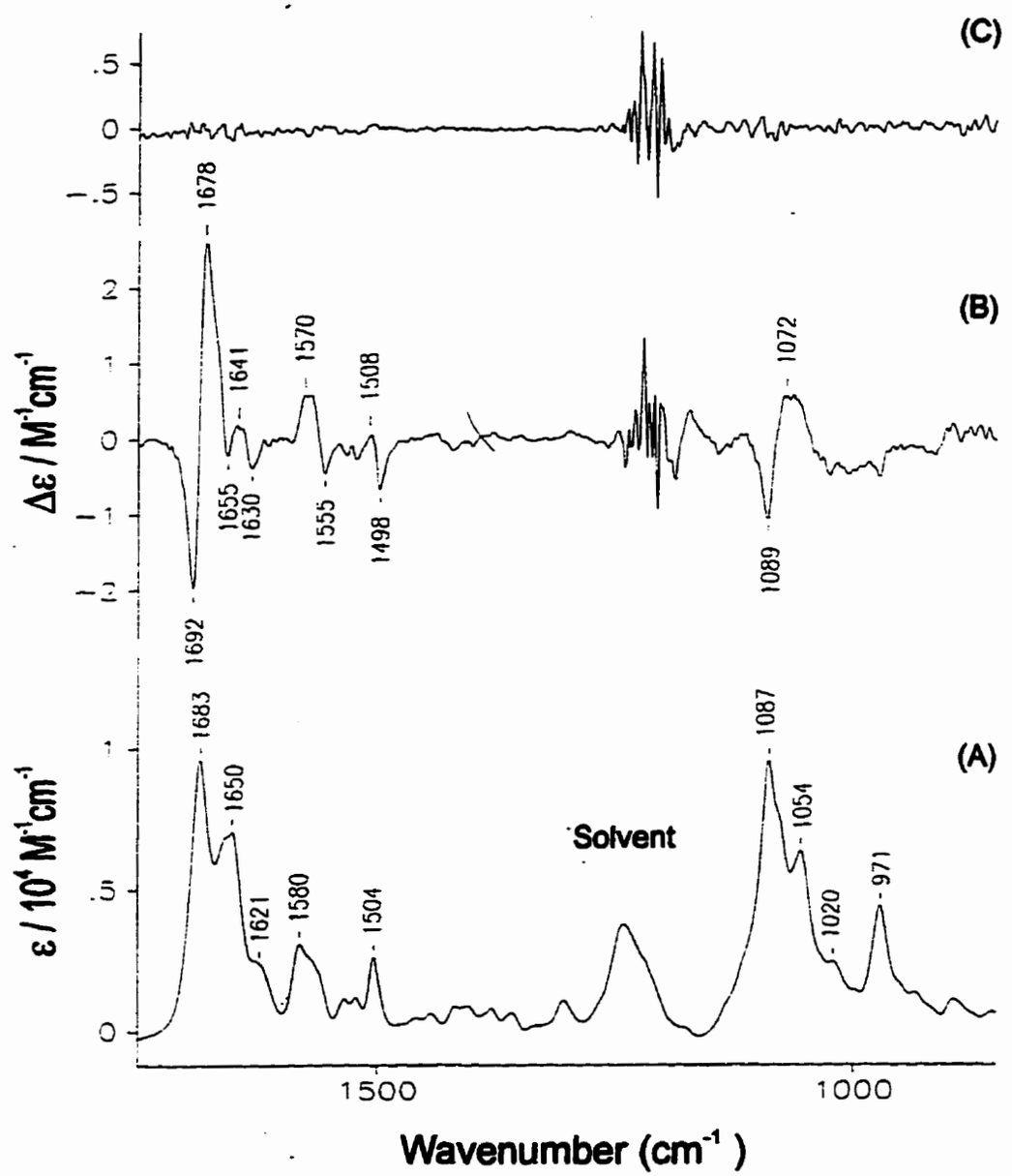

Figure 8
Experimental IR/VCD Spectra of d(CGCGCGCG).d(CGCGCGCG)

Experimental IR absorption (A) and VCD (B) spectra with the noise estimate (C).

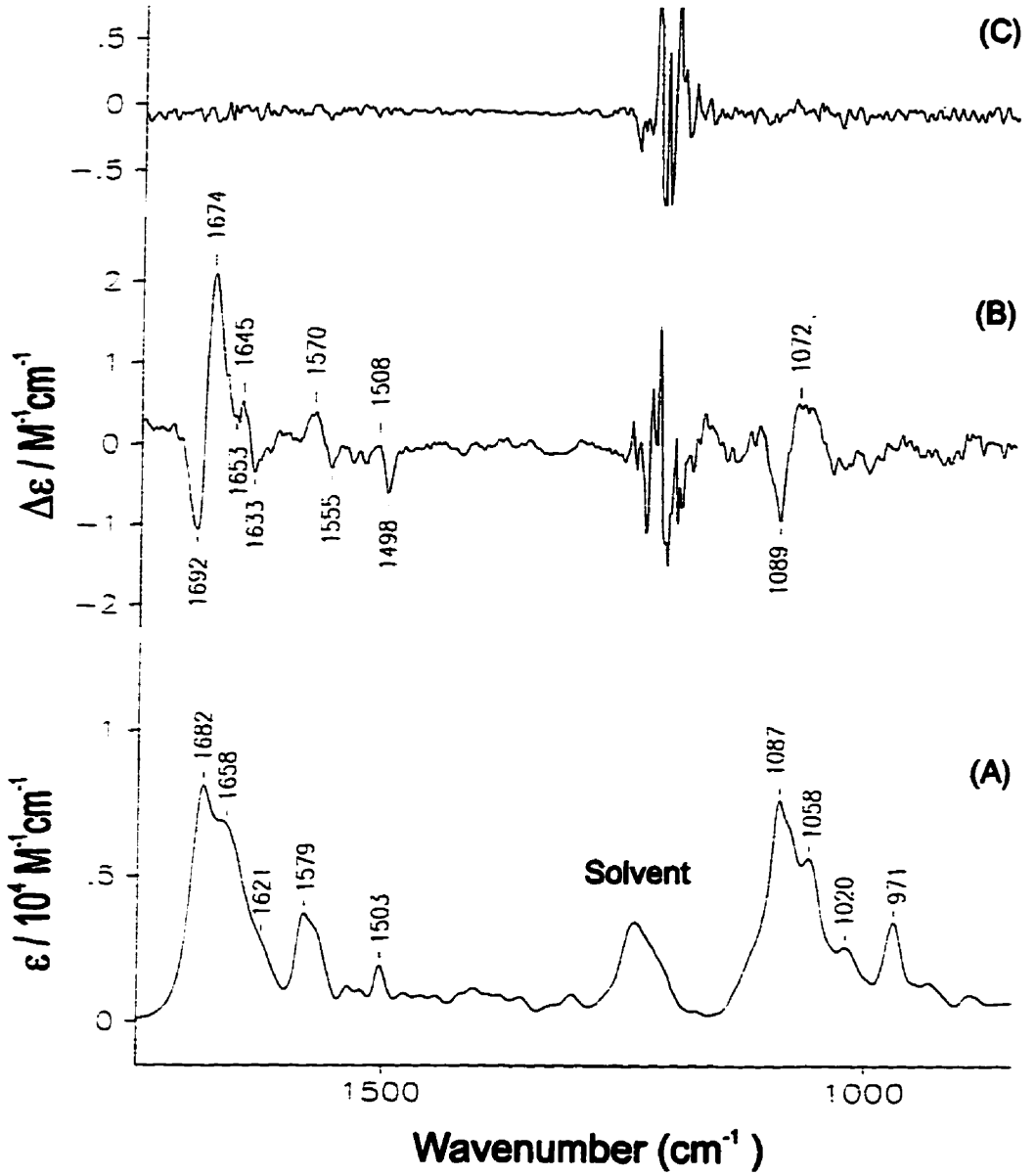

Figure 9
Experimental IR/VCD Spectra of d(CGCGTGCG).d(CGCGTGCG)

Experimental IR absorption (A) and VCD (B) spectra with the noise estimate (C).

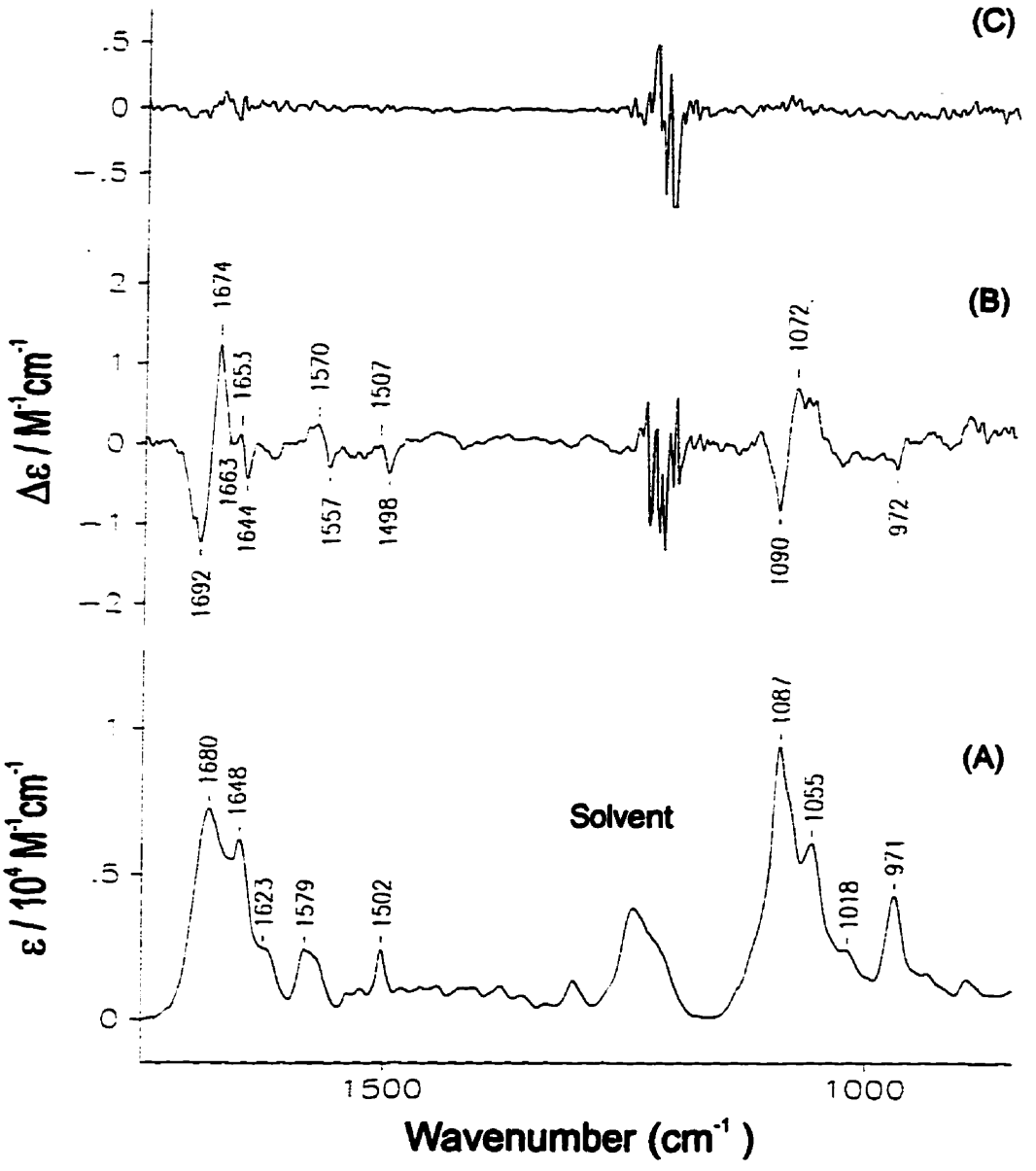

Figure 10
Experimental IR/VCD Spectra of d(CGCATGCG).d(CGCATGCG)

Experimental IR absorption (A) and VCD (B) spectra with the noise estimate (C).

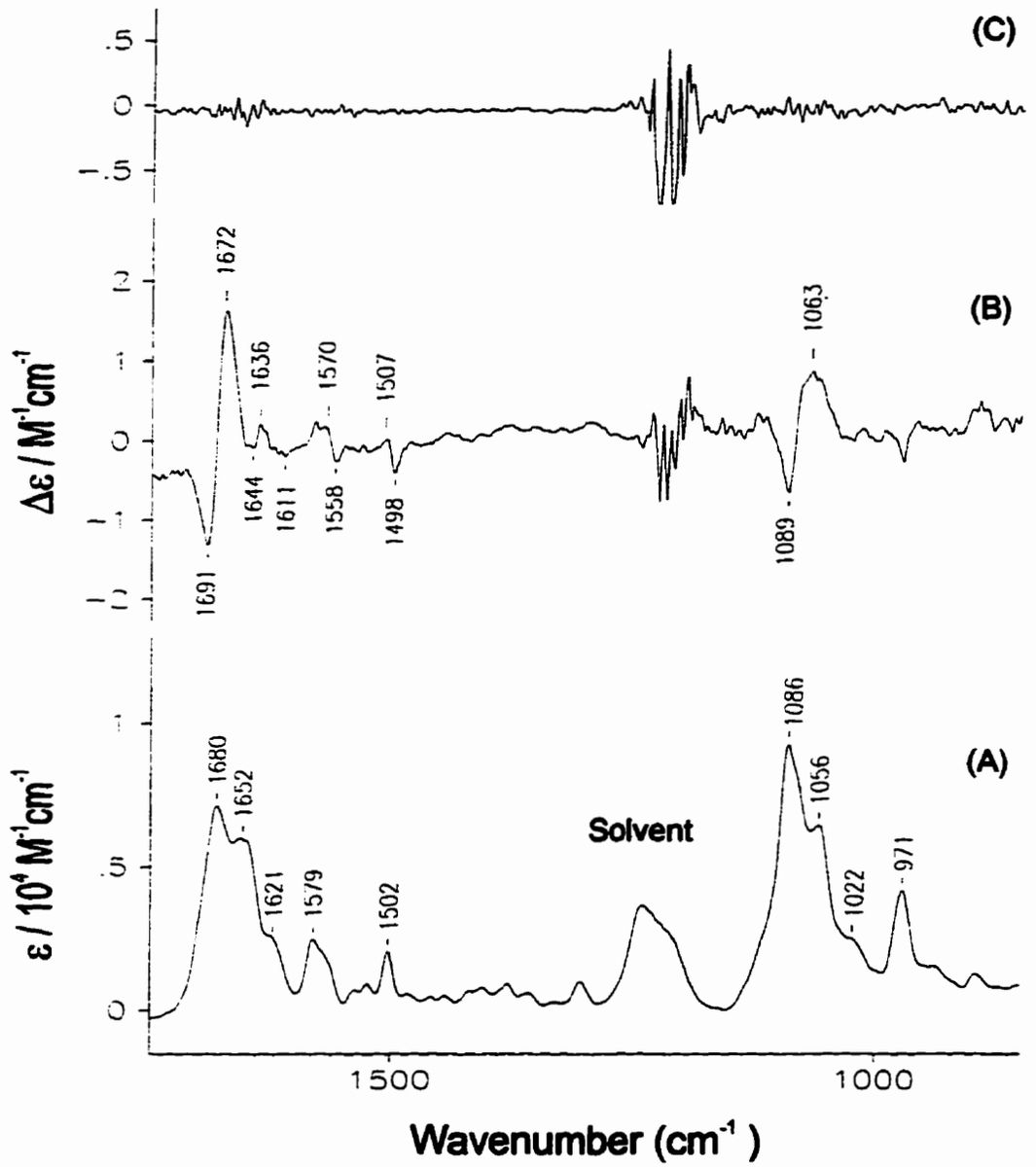

Figure 11
Experimental IR/VCD Spectra of d(CGCTAGCG).d(CGCTAGCG)

Experimental IR absorption (A) and VCD (B) spectra with the noise estimate (C).

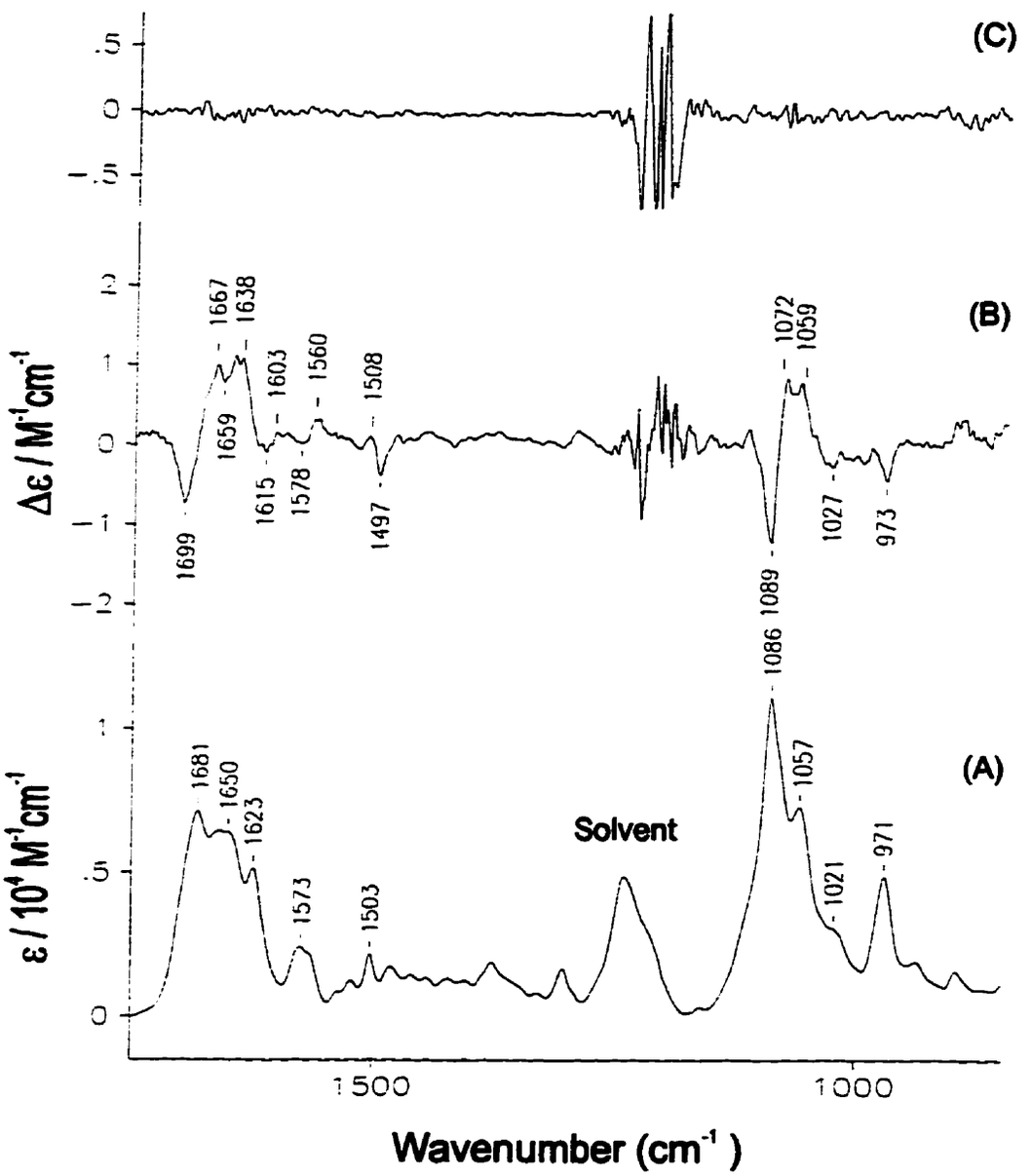

Figure 12
Experimental IR/VCD Spectra of d(CGATATCG).d(CGATATCG)

Experimental IR absorption (A) and VCD (B) spectra with the noise estimate (C).

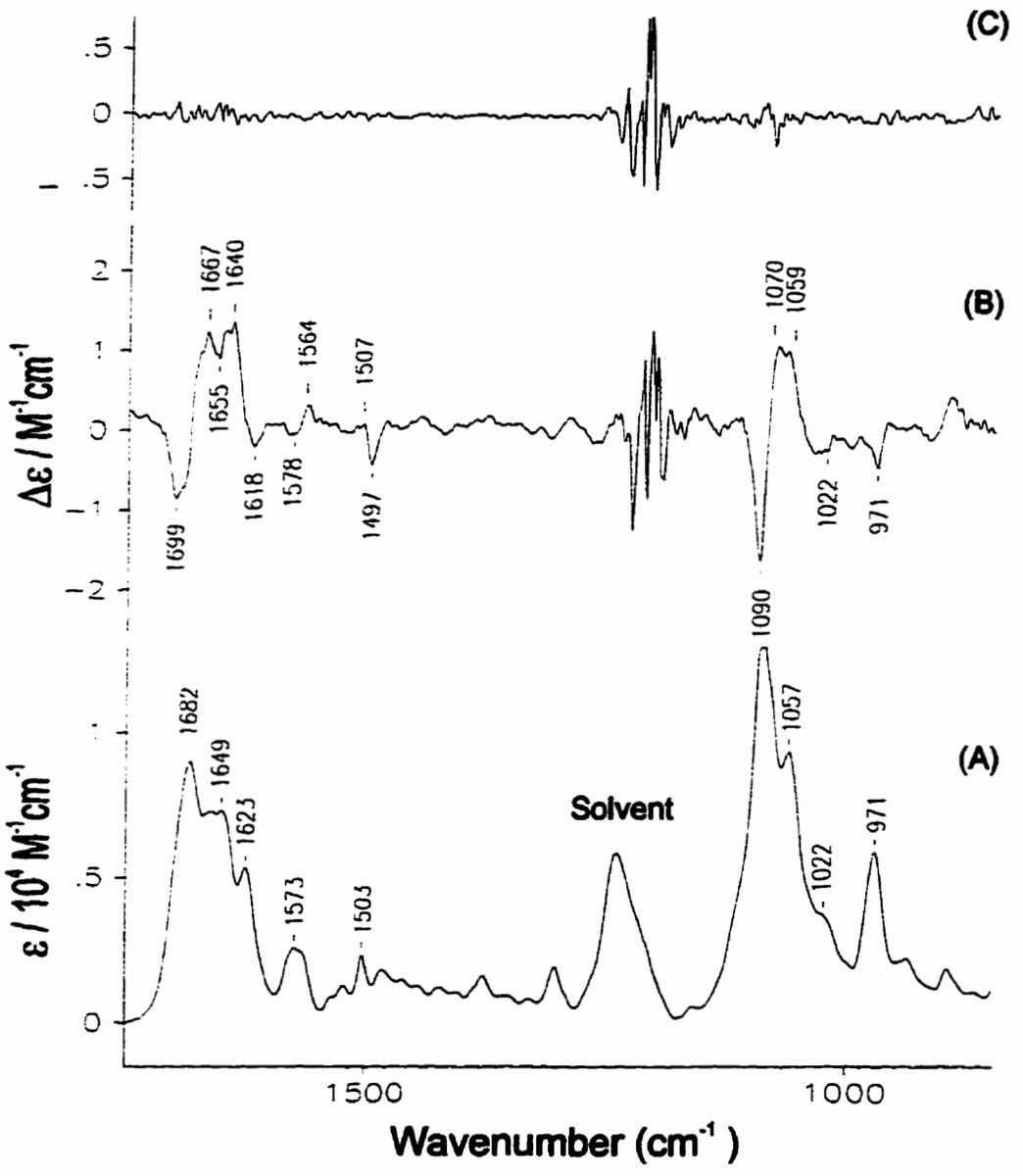

Figure 13
Experimental IR/VCD Spectra of d(CGTATACG).d(CGTATACG)

Experimental IR absorption (A) and VCD (B) spectra with the noise estimate (C).

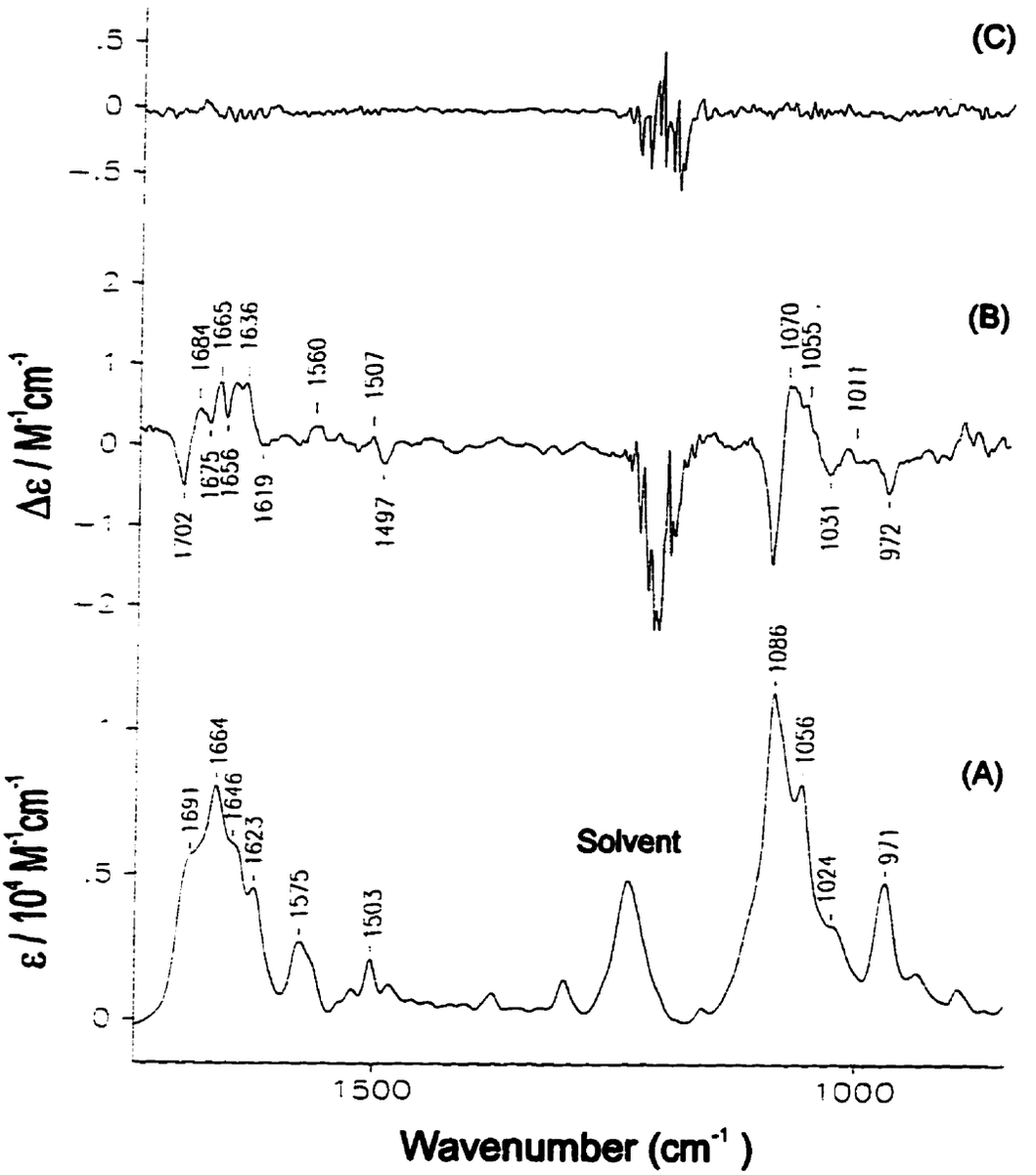

Figure 14
Experimental IR/VCD Spectra of d(CGAATTCG).d(CGAATTCG)

Experimental IR absorption (A) and VCD (B) spectra with the noise estimate (C).

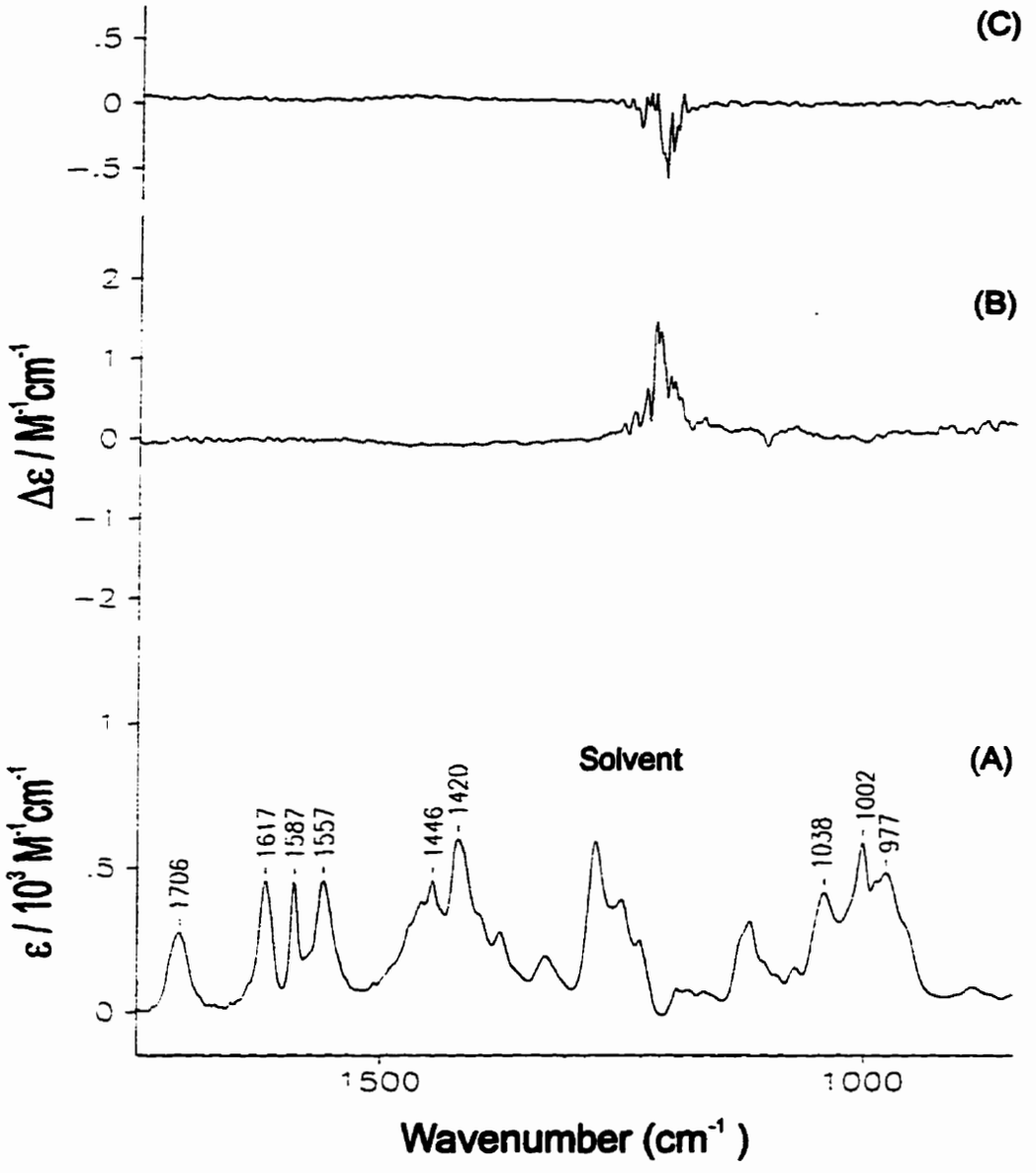

Figure 15
Experimental IR/VCD Spectra of Daunorubicin

Experimental IR absorption (A) and VCD (B) spectra with the noise estimate (C).

a) d(CGCGCGCG).d(CGCGCGCG)-2(Daunorubicin) (Figure 16, page 55)

The IR absorption and VCD spectra of the principal sequence, d(CGCGCGCG). d(CGCGCGCG) (see Figure 8, page 44), are still the most intense of the selected deoxyoctanucleotides in the 1750-1500 cm^{-1} region, after intercalation with daunorubicin. The VCD couplet of highest intensity at 1687(-)/1668(+) cm^{-1} associated with the IR absorption band at 1679 cm^{-1} has shifted to lower energy when compared to the VCD couplet at 1692(-)/1678(+) cm^{-1} corresponding to the IR absorption band at 1683 cm^{-1} in the free deoxyoctanucleotide. The IR absorption band at 1647 cm^{-1} increased in intensity giving rise to a VCD couplet at 1651(-)/1641(+), which differs significantly from the VCD couplet at 1655(-)/1647(+) cm^{-1} corresponding to the IR absorption band at 1650 cm^{-1} in the free deoxyoctanucleotide. Some of the VCD couplets that are retained upon intercalation include those at 1568(+)/1556(-), 1504(+)/1497(-) and 1090(-)/1076(+) cm^{-1} corresponding to IR absorption bands at 1562, 1501 and 1087 cm^{-1}, respectively.

b) d(CGCATGCG).d(CGCATGCG)-2(Daunorubicin) (Figure 17, page 56)

The IR absorption and VCD couplets in the 1700-1600 cm^{-1} region have shifted to lower energy upon intercalation with daunorubicin. The most prominent VCD couplet at 1692(-)/1674(+) cm^{-1} arising from the IR absorption band at 1681 cm^{-1} in the free deoxyoctanucleotide has shifted to 1687(-)/1667(+) cm^{-1} corresponding to the IR absorption band at 1674 cm^{-1}, with a broader, less intense negative VCD feature. The couplet at 1653(+)/1644(-) cm^{-1} centered at 1648 cm^{-1}, on the other hand, has increased in intensity and shifted very slightly to 1651(-)/1641(+) cm^{-1} corresponding to the IR absorption band at 1646 cm^{-1} upon intercalation with daunorubicin . IR absorption bands at 1087, 1562 and 1501 cm^{-1} affiliated with the VCD couplets at 1089(+)/1074(+), 1570(+)/1555(-) and 1504(+)/1497(-) cm^{-1}, are retained and more discernible than in the free deoxyoctanucleotide. The VCD features at about 1060(+) cm^{-1} appear to be slightly

better resolved in d(CGCTAGCG).d(CGCTAGCG)-2(Daunorubicin) than those in d(CGCATGCG).d(CGCATGCG)-2(Daunorubicin).

c) d(CGCTAGCG).d(CGCTAGCG)-2(Daunorubicin) (Figure 18, page 57)

Upon intercalation with daunorubicin the most prominent VCD couplet in the free deoxyoctanucleotide, 1692(-)/1674(+) cm^{-1} corresponding to the IR absorption band at 1681 cm^{-1}, has shifted to lower energy 1682(-)/1665(+) cm^{-1} associated with the IR absorption band at 1673 cm^{-1}, with a sharper, more intense negative VCD feature than that of d(CGCATGCG).d(CGCATGCG)-2(Daunorubicin). A VCD couplet, not evident in the free deoxyoctanucleotide, has emerged at 1649(+)/1642(-) cm^{-1} corresponding to the IR absorption band at 1646 cm^{-1}. IR absorption bands at 1087, 1562 and 1501 cm^{-1} corresponding to the VCD couplets at 1090(+)/1072(+), 1568(+)/1558(-) and 1504(+)/1497(-) cm^{-1}, respectively, are retained with the 1568(+)/1558(-) cm^{-1} couplet being more discernible than in the free deoxyoctanucleotide.

b) d(CGATATCG).d(CGATATCG)-2(Daunorubicin) (Figure 19, page 58) and
d(CGTATACG).d(CGTATACG)-2(Daunorubicin) (Figure 20, page 59)

Upon intercalation with daunorubicin, the free deoxyoctanucleotides, d(CGATATCG). d(CGATATCG) and d(CGTATACG).d(CGTATACG) appear to have lost their VCD couplet at 1699(-)/1667(+) cm^{-1} corresponding to the IR absorption band at 1681 cm^{-1} and a new couplet seems to have emerged at significantly lower energy, viz. 1676(-?)/1659(+) cm^{-1} associated with the IR absorption band at 1666 cm^{-1}. It thus appears that the 1699(-)/1667(+) cm^{-1} couplet (see Figure 8, page 44), assigned to the C-G base-pair (Zhong *et al.*, 1990), has disappeared upon intercalation thereby suggesting a markedly reduced contribution from the C-G base-pair. The VCD couplet at 1578(-)/1562(+) cm^{-1} centered at 1573 cm^{-1} in the free deoxyoctanucleotides are also replaced by a couplet at 1564(+)/1554(-) cm^{-1} affiliated with an IR absorption band at

1564 cm^{-1}. The IR absorption spectra appear to be somewhat better resolved upon intercalation. Conversely, the VCD couplet at 1636(+)/1618(-) cm^{-1} corresponding to the IR absorption band at 1621 cm^{-1} is retained and probably concurs with that reported at 1640(+)/1625(-) cm^{-1} attributed to the A-T base-pair (Zhong *et al.*, 1990), the 1504(+)/1496(-) cm^{-1} couplet centered at 1500 cm^{-1} has reduced intensity and the VCD couplet at 1090(-)/1072(+) cm^{-1} centered at 1087 cm^{-1} also has decreased intensity even though the IR absorption intensity is unchanged. The VCD features at about 1060(+) cm^{-1} appear to be better resolved in d(CGATATCG).d(CGATATCG)-2(Daunorubicin) than in d(CGTATACG). d(CGTATACG)-2(Daunorubicin).

b) d(CGAATTCG).d(CGAATTCG)-2(Daunorubicin) (Figure 21, page 60)

This sequence is unique in its manifestation of significantly varied intensities of the various VCD couplets rather than replacing couplets with lower energy ones in the 1700-1600 cm^{-1} region, as a result of daunorubicin intercalation. The VCD couplet at 1704(-)/1686(+) cm^{-1} corresponding to the IR absorption band at 1691 cm^{-1} has substantially diminished in intensity, the couplet at 1673(-)/1661(+) cm^{-1} affiliated with the IR absorption band at 1664 cm^{-1} has slightly shifted to lower energy but considerably increased in intensity and the VCD couplet at 1636(+)/1619(-) cm^{-1} corresponding to the IR absorption band at 1623 cm^{-1} diminished in intensity. The diminution of the first mentioned couplet assigned to the C-G base-pair (Birke *et al.*, 1993), suggests a considerably reduced contribution from the C-G base-pair, whereas the 1636(+)/1619(-) cm^{-1} couplet probably concurs with that reported at 1640(+)/1625(-) cm^{-1} attributed to the A-T base-pair (Zhong *et al.*, 1990). The VCD couplet at 1090(-)/1074(+) cm^{-1} corresponding to the IR absorption band at 1087 cm^{-1} is retained with an equivalent magnitude to that of the free deoxyoctanucleotide, whereas VCD couplets at 1564(+)/1554(-) and 1504(+)/1497(-) cm^{-1} affiliated the IR absorption band at 1564 and 1500 cm^{-1}, respectively, are not definitive.

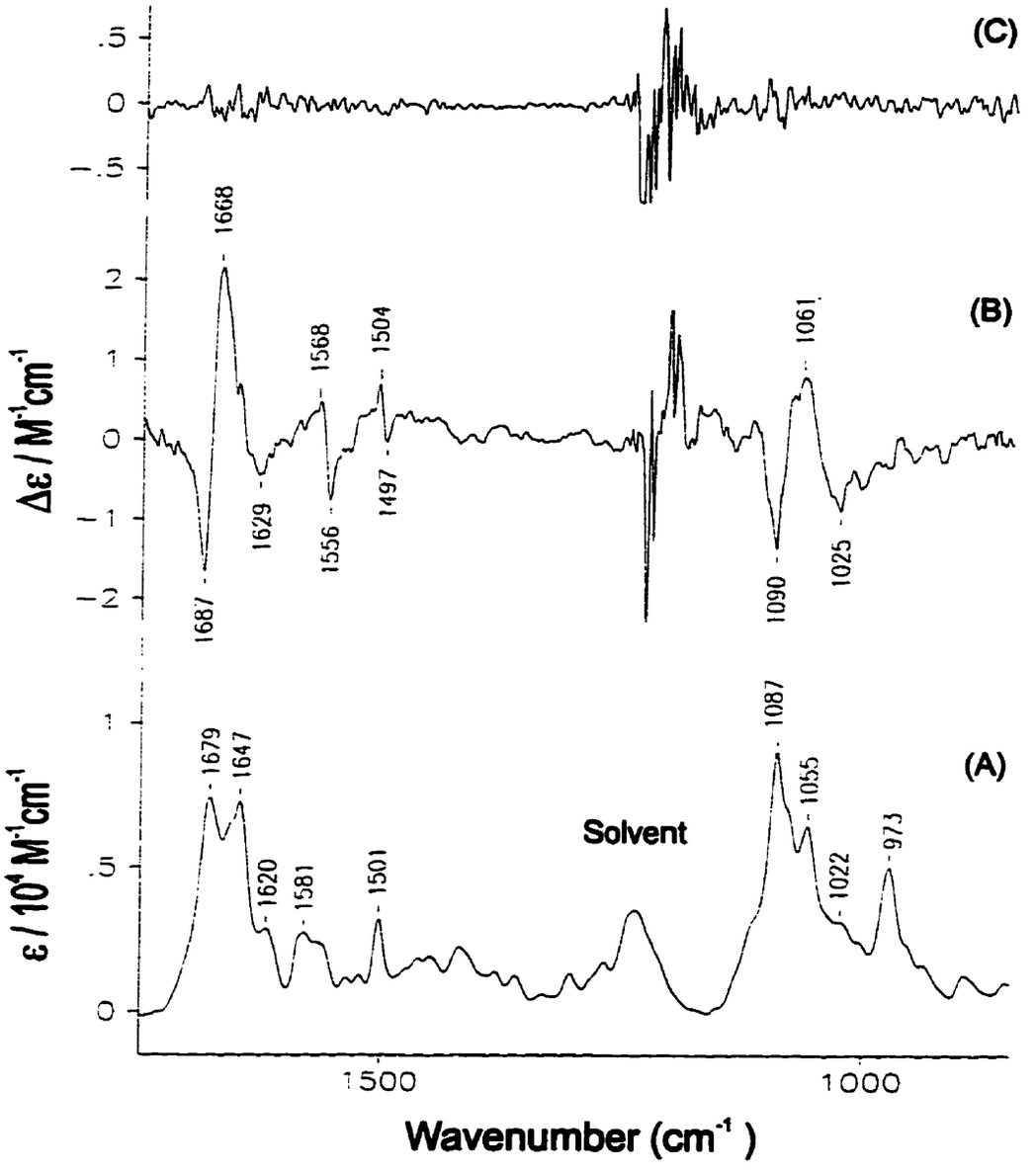

Figure 16
Experimental IR/VCD Spectra of
d(CGCGCGCG).d(CGCGCGCG)-2(Daunorubicin)

Experimental IR absorption (A) and VCD (B) spectra with the noise estimate (C).

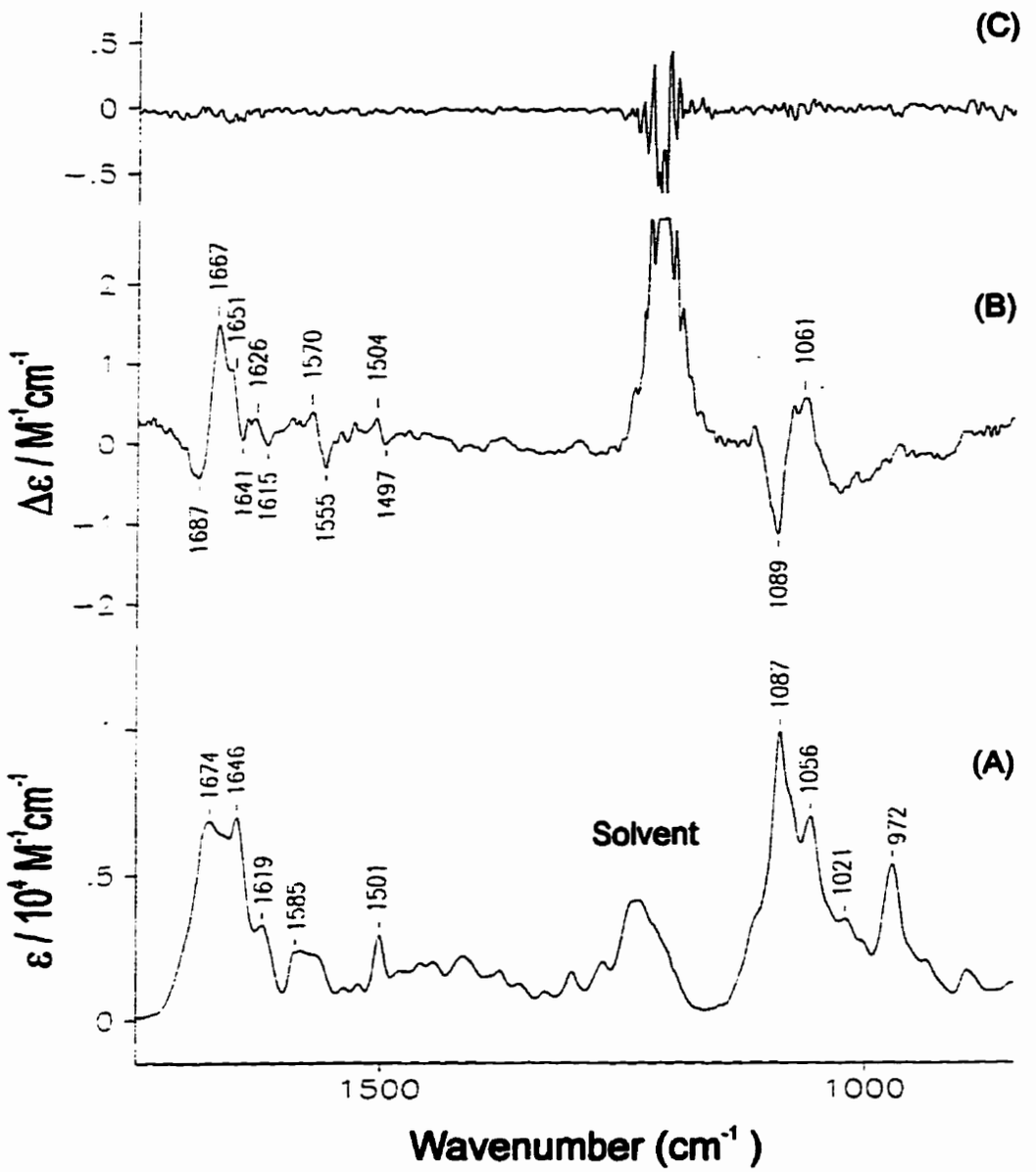

Figure 17
Experimental IR/VCD Spectra of
d(CGCATGCG).d(CGCATGCG)-2(Daunorubicin)

Experimental IR absorption (A) and VCD (B) spectra with the noise estimate (C).

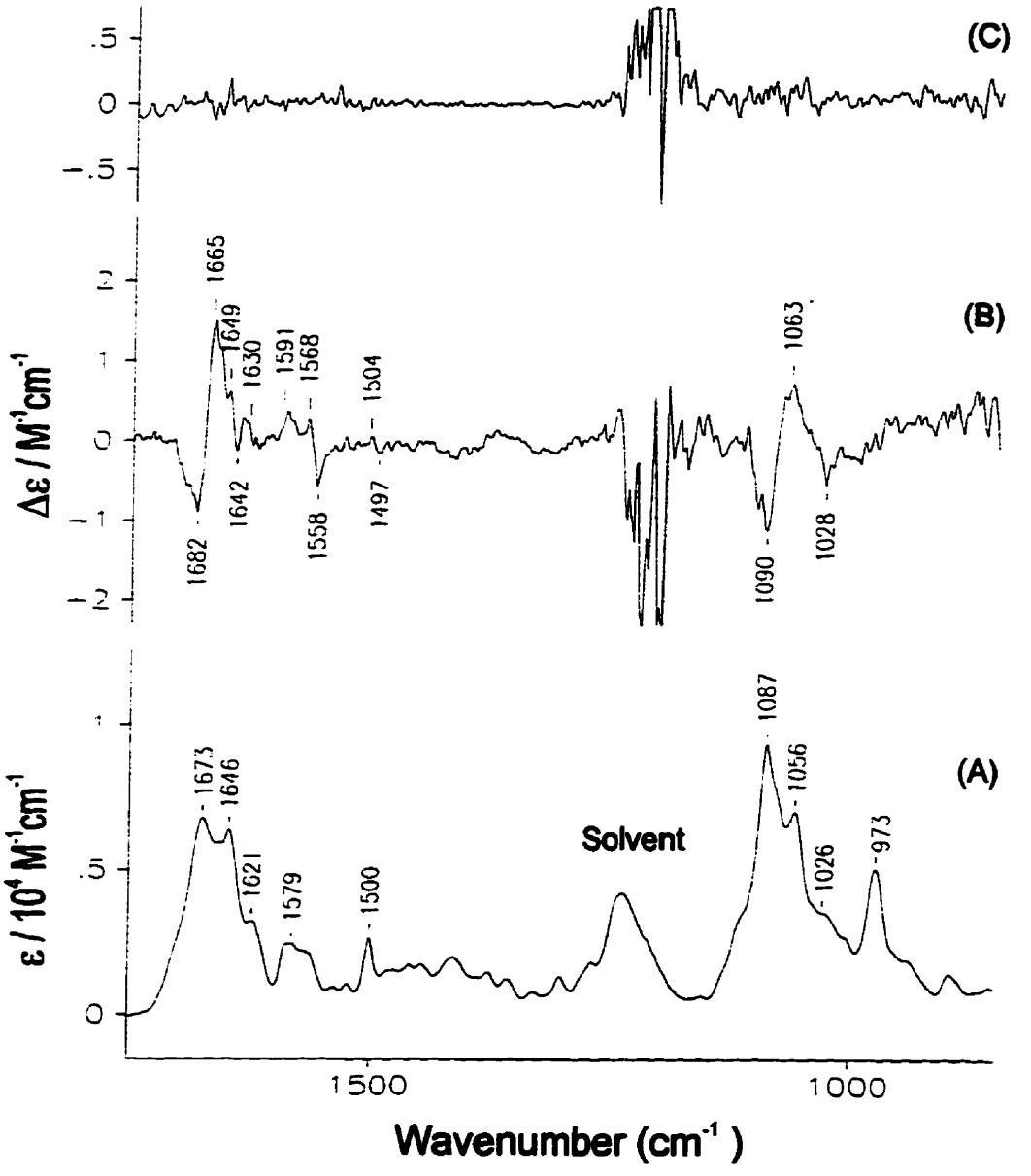

Figure 18
Experimental IR/VCD Spectra of
d(CGCTAGCG).d(CGCTAGCG)-2(Daunorubicin)

Experimental IR absorption (A) and VCD (B) spectra with the noise estimate (C).

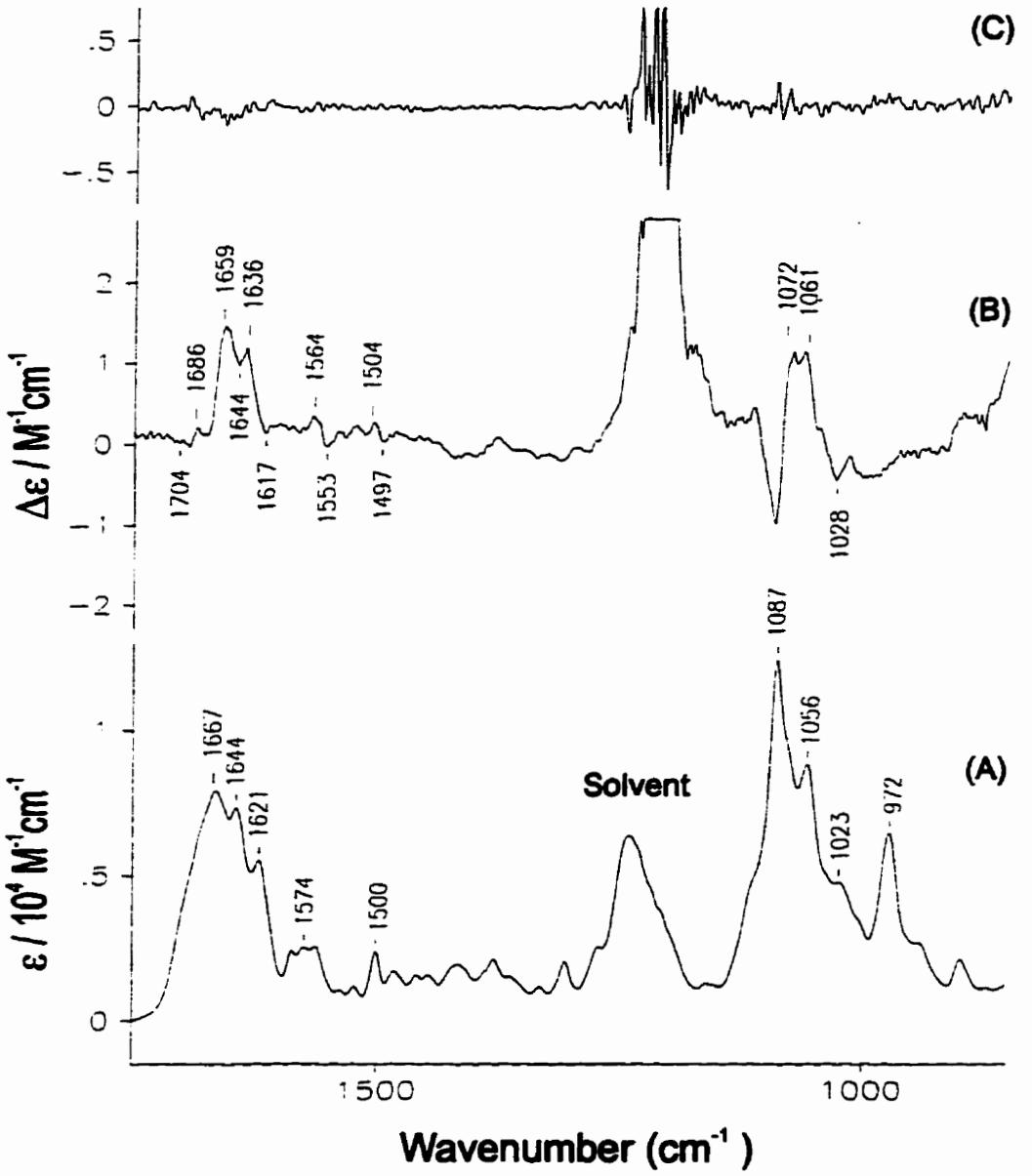

Figure 19
Experimental IR/VCD Spectra of
d(CGATATCG).d(CGATATCG)-2(Daunorubicin)

Experimental IR absorption (A) and VCD (B) spectra with the noise estimate (C).

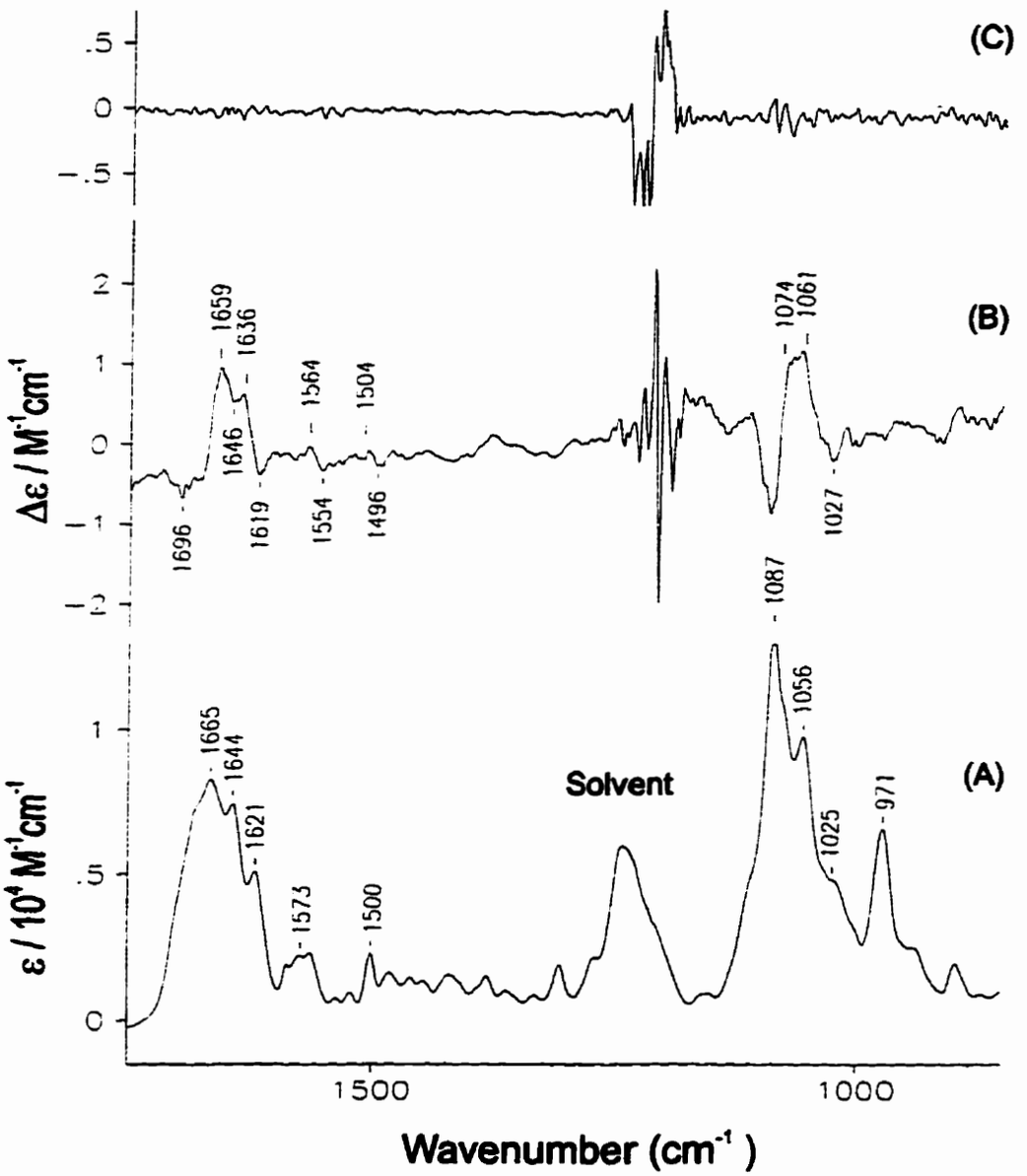

Figure 20
Experimental IR/VCD Spectra of
d(CGTATACG).d(CGTATACG)-2(Daunorubicin)

Experimental IR absorption (A) and VCD (B) spectra with the noise estimate (C).

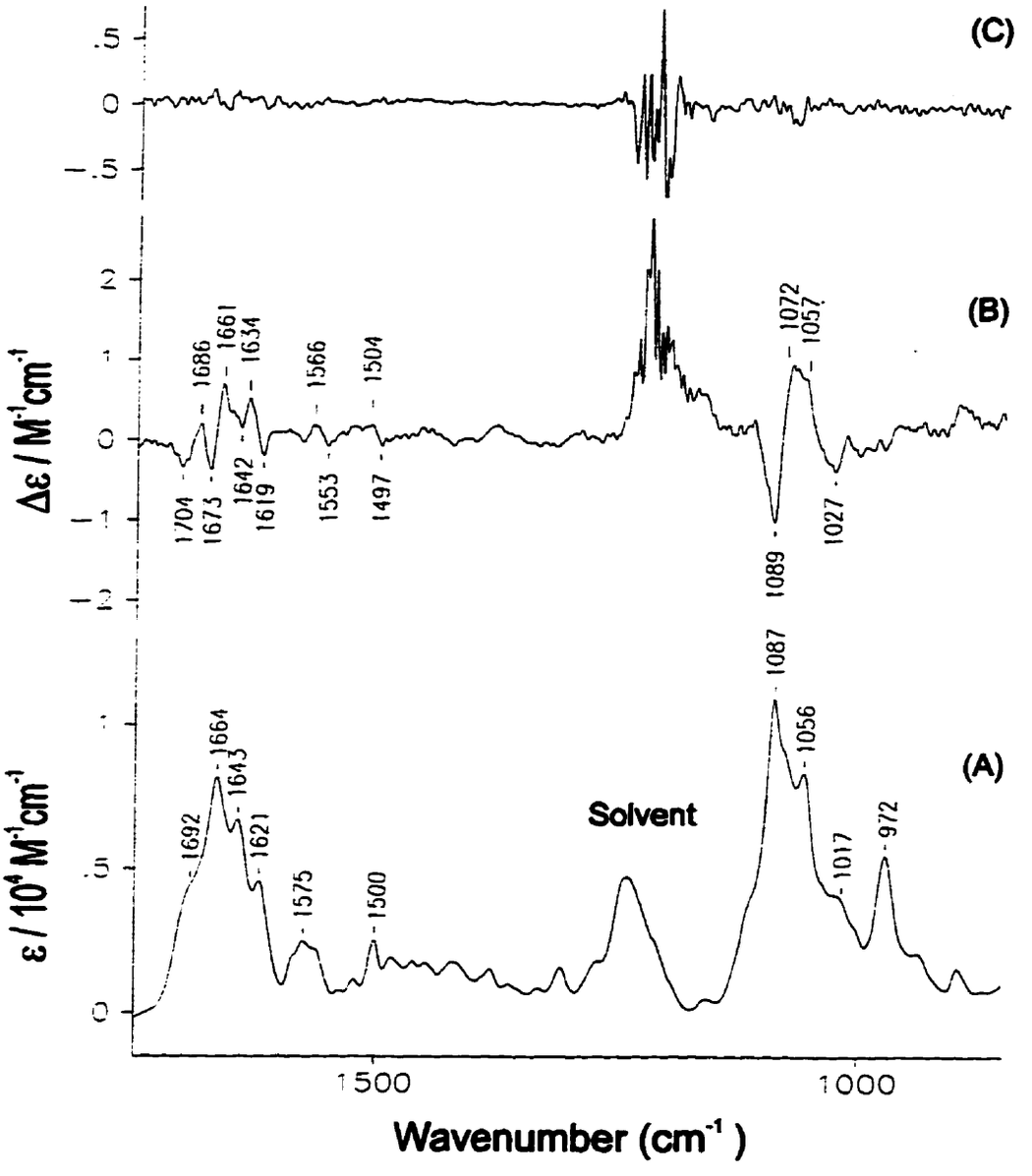

Figure 21
Experimental IR/VCD Spectra of
d(CGAATTCG).d(CGAATTCG)-2(Daunorubicin)

Experimental IR absorption (A) and VCD (B) spectra with the noise estimate (C).

4.5.4 Experimental Difference VCD Spectra

The difference VCD spectra (illustrated in Figure 22, page 63), deoxyoctanucleotide-daunorubicin complex minus deoxyoctanucleotide, reflects the deoxyoctanucleotide conformational changes upon intercalation with daunorubicin. Since VCD spectra are insensitive to contributions from daunorubicin conformational changes, the changes in the difference VCD spectra must be due to binding.

The discussion that follows is purely conjectured at this stage and can only be confirmed by further experimental and computational developments. The difference VCD spectra (see Figure 22, page 63) show a cancellation of the phosphate backbone features in the region of 1100-1050 cm^{-1} and an apparent sequential splitting of the negative features, in the 1600-1700 cm^{-1} region, corresponding to increased base substitution of the principal sequence. This trend is in keeping with the triplet sequence preference of daunorubicin, viz. 5′-TCG ≥ 5′-ACG > 5′-ATA >> 5′-GCG > 5′-GTA (Chaires, 1990). Figure 22 on page 63 displays one negative VCD feature for $^{5'}d(CGCGCGCG)_{3'}.^{5'}d(CGCGCGCG)_{3'}$, $^{5'}d(CGCATGCG)_{3'}.^{5'}d(CGCATGCG)_{3'}$ and $^{5'}d(CGCTAGCG)_{3'}.^{5'}d(CGCTAGCG)_{3'}$, which possess the 5′-GCG triplet, and two negative VCD features for $^{5'}d(CGATATCG)_{3'}.$ $^{5'}d(CGATATCG)_{3'}$, $^{5'}d(CGTATACG)_{3'}.^{5'}d(CGTATACG)_{3'}$ and $^{5'}d(CGAATTCG)_{3'}.$ $^{5'}d(CGAATTCG)_{3'}$ which contain the 5′-TCG, 5′-ACG (and 5′-GTA) and 5′-TCG triplets, respectively. $^{5'}d(CGAATTCG)_{3'}.^{5'}d(CGAATTCG)_{3'}$ also hints at a possible third negative VCD feature, but this is not definitive.

Consequently, complexes containing the more preferred triplet sequences for daunorubicin recognition confer more observable changes in the difference VCD spectra, thereby suggesting that deoxyoctanucleotides containing the most preferred triplet sequences of daunorubicin experience greater conformational changes upon intercalation of daunorubicin.

The deoxyoctanucleotides, d(CGATATCG).d(CGATATCG), d(CGTATACG).d(CGTATACG) and d(CGAATTCG).d(CGAATTCG), contain the most preferred daunorubicin triplet sequences. Upon intercalation with daunorubicin these sequences revealed markedly diminished C-G base-pair contributions in the VCD spectra, thus suggesting that the dipolar coupling between the terminal C-G base-pairs is extensively disrupted, which is consistent with daunorubicin intercalating between the terminal C-G base-pairs, with a triplet sequence preference as reported by previous X-ray crystallography, solution and theoretical literature (Chaires, 1990; Chen *et al.*, 1985; Chaires *et al.*, 1990; Frederick *et al.*, 1990; Wang *et al.*, 1987). In terms of the information that emerges from VCD versus the standard infrared absorption spectra it may be of interest to compare the above results with those deduced in a recent study of deoxyhexanucleotide duplexes complexed with nogalamycin (Missailidis & Hester, 1995). The observed difference in the absorption bands are subtle and difficult to quantify.

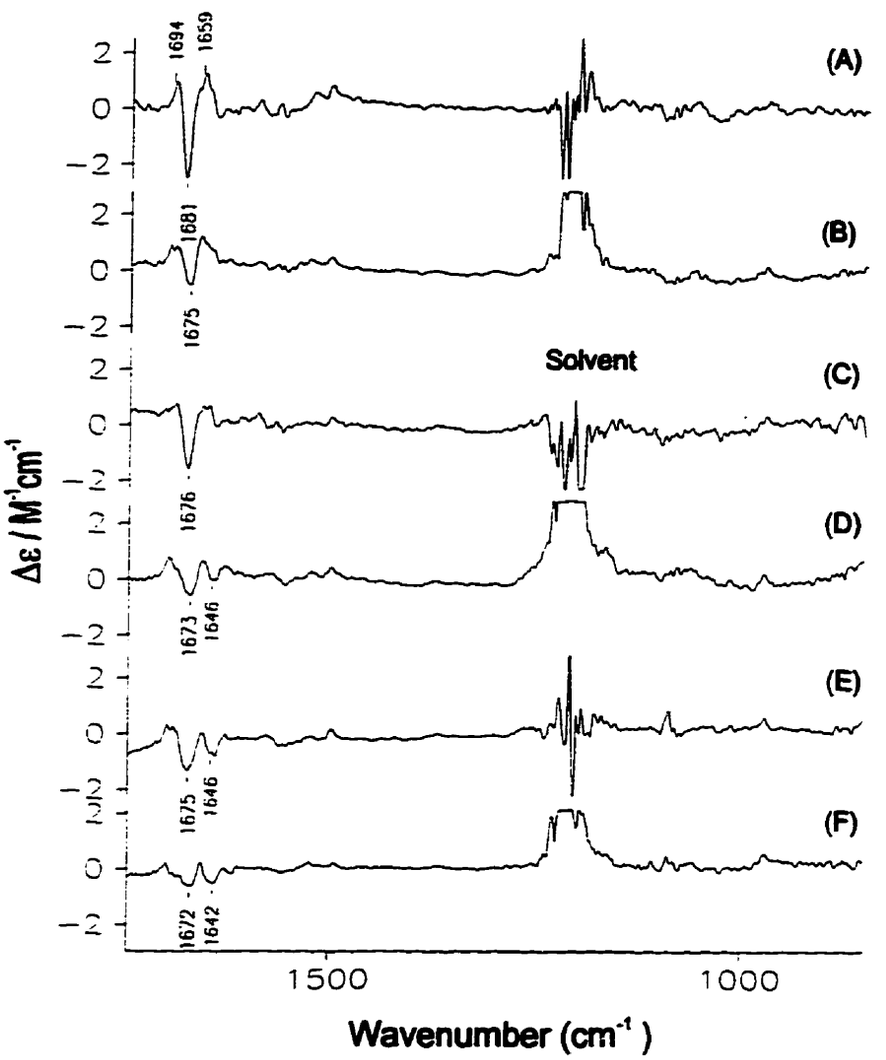

Figure 22
Experimental Difference VCD Spectra of Deoxyoctanucleotides

Deoxyoctanucleotide-Daunorubicin Complex minus Deoxyoctanucleotide VCD Spectra
(A) ⇒ d(CGCGCGCG).d(CGCGCGCG)
(B) ⇒ d(CGCATGCG).d(CGCATGCG)
(C) ⇒ d(CGCTAGCG).d(CGCTAGCG)
(D) ⇒ d(CGATATCG).d(CGATATCG)
(E) ⇒ d(CGTATACG).d(CGTATACG)
(F) ⇒ d(CGAATTCG).d(CGAATTCG)

5. Computations

5.1 Ab Initio Calculations

In order to extract the desired structural information, the observed UV/IR absorption and ECD/VCD spectra must be compared with those theoretically simulated by suitable calculations. *Ab initio* calculations are most desirable, however they are currently feasible for relatively small molecules only and are beyond the scope of the large molecules of interest in this work. Instead, an approximate model, viz. the non-degenerate extended coupled oscillator (NECO) model, was used for simulating the spectra of deoxyoctanucleotides and deoxyoctanucleotide-daunorubicin complexes. This model exhibits classic coupling of oscillators within chromophores distributed in space. The magnitude and orientation of the electric transition dipole moments within the chromophores are required by the NECO model, and have been derived by *ab initio* calculations on the deoxyoctanucleotide components.

5.1.1 Literature Survey

An overwhelming number of Raman and infrared citations on biological molecules exist in the literature (Wang *et al.*, 1987; Nishimura & Tsuboi, 1986; Taillandier, 1990; Taillandier *et al.*, 1985). Literature relevant to this work include computations based on DNA nucleotide bases, base-pairs and the DNA sugar-phosphate backbone. *Ab initio* predictions at the Hartree-Fock (HF)/6-31G** level of theory have been reported for the infrared absorption wavenumbers of C (Gould *et al.*, 1992), G (Gould *et al.*, 1993), T (Les *et al.*, 1992) and A (Nowak *et al.*, 1994), together with their vibrational assignments. The amino groups of C, G and A were shown to be non-planar at the HF level with the 6-31G* basis set, and for C also at the MP2/6-31G* level (Leszczynski, 1992). More recently the computed infrared and Raman spectra of the C-G base-pair, together with vibrational assignments were reported at the HF/6-31G* level of theory (Florian & Leszczynski, 1995), whereas literature on the A-T base-pair at an equivalent level of theory is non-existent at this stage. IR and Raman wavenumbers of the dimethyl phosphate anion derived from the B3-LYP/6-31G* procedure have also been reported

with vibrational assignments (Florian *et al.*, 1996), while computed absorption wavenumbers of deoxyribose have not been reported previously.

5.1.2 Procedure

Energy-minimized geometries, harmonic force fields and atomic polar tensors of the nucleotide components, viz. the deoxyribose sugar residue (in the form of 1-amino-deoxyribose) illustrated in Figure 1, page 8; the phosphate residue (in the form of dimethyl phosphate anion) exemplified in Figure 1, page 8; the nucleotide bases (G, C, A and T) shown in Figure 2, page 9; and the nucleotide base-pairs (C-G and A-T) illustrated in Figure 3, page 10, were calculated with the B3-LYP procedure (Becke, 1993), a hybrid Hartree Fock (HF) - Density functional theory (DFT) method, and the 6-31G** basis set using the Gaussian 94 programs (Gaussian 94 Revision B.3, 1995). All experimental measurements were conducted in deuterium oxide, therefore the nucleotide components used for IR computations have exchangeable hydrogen atoms substituted with deuterium. The standard geometry coordinates of the nucleotide components are listed in Appendix 1. To obtain the electric transition dipole moments for simulating the UV/ECD spectra, the nucleotide bases were also calculated with the configuration interaction singles (CIS) approach, a single point calculation used for modeling excited states such that the distribution of all the electrons is described by all possible single excitations (Rauk, 1994), and the 6-31+G* basis set using the Gaussian 94 programs (Gaussian 94 Revision B.3, 1995).

C_s symmetry was assumed for the nucleotide bases and base-pairs. The standard keto-tautomeric forms were used for the nucleotide bases, since there is no spectroscopic evidence for the existence of enol tautomers greater than 0.01%, at physiological pH (Blackburn, 1990). However, the possibility of isomerization cannot be excluded. The four torsion angles of 1-amino-deoxyribose, $C_{(5)}$-$C_{(4)}$-$N_{(2)}$-$H_{(1)}$, $H_{(14)}$-$O_{(12)}$-$C_{(11)}$-$C_{(10)}$, $O_{(18)}$-$C_{(16)}$-$C_{(10)}$-$O_{(9)}$ and $H_{(20)}$-$O_{(18)}$-$C_{(16)}$-$C_{(10)}$, and the dimethyl phosphate anion, $P_{(4)}$-$O_{(3)}$-$C_{(2)}$-$H_{(1)}$, $O_{(5)}$-$P_{(4)}$-$O_{(3)}$-$C_{(2)}$, $C_{(6)}$-$O_{(5)}$-$P_{(4)}$-$O_{(3)}$ and $H_{(7)}$-$C_{(6)}$-$O_{(5)}$-$P_{(4)}$ (see Figure 1, page 8) , were constrained to the values corresponding to the standard B-DNA helices, generated for the selected deoxyoctanucleotides using MSI's molecular modeling system

(*Insight II* 95.0, 1995), shown in Figure 23, page 67 for d(CGAATTCG). d(CGAATTCG).

The B3-LYP method employed with the 6-31G** basis set systematically overestimates vibrational wavenumbers by about 5% (Rauhut & Pulay, 1995). Hence calculated wavenumbers of all normal modes were scaled by a factor of 0.95. Vibrational mode analysis was carried out in order to make tentative vibrational assignments. The internal and local symmetry coordinates were defined as usual (Fogarasi & Pulay, 1985). The normal coordinate analyses were carried out by programs described elsewhere (Bour & Keiderling, 1993). The definitions of the internal valence and local symmetry coordinates used for the nucleotide bases can be found in Appendix 2 and those used for the base-pairs are listed in Table 4 and Table 6. Potential energy distribution (PED) contributions for both the deuterated and undeuterated nucleotide bases (see Appendix 2), the undeuterated base-pairs (see Appendix 2) and the deuterated base-pairs (see Table 5 and Table 7) include wavenumbers corresponding to the experimental spectral range of 1750-850 cm^{-1}. PED contributions less than 10 % are excluded.

The IR absorption wavenumbers were calculated for the undeuterated nucleotide components with the B3-LYP/6-31G** procedure (see Appendix 2), so as to establish reliability of these computational results by comparison with those reported previously. The undeuterated nucleotide bases calculated with the B3-LYP/6-31G** procedure (listed in Appendix 2) agree largely with those reported in the literature for C (Gould *et al.*, 1992), T (Les *et al.*, 1992), G (Gould *et al.*, 1993) and A (Nowak *et al.*, 1994) at the HF/6-31G* level of theory. C, G and A possess amino groups which were shown to be non-planar with *ab initio* HF/6-31G* and MP2/6-31G* studies (Leszczynski, 1992). Accordingly, the imaginary wavenumbers evident at low energy for C, G and A in this study are due to the C_s symmetry imposed for the nucleotide base calculations. The absorption wavenumbers of the undeuterated C-G base-pair calculated with the B3-LYP/6-31G** procedure (see Appendix 2) compare satisfactorily with those derived from *ab initio* HF/6-31G* (Florian & Leszczynski, 1995). However, they do differ in the

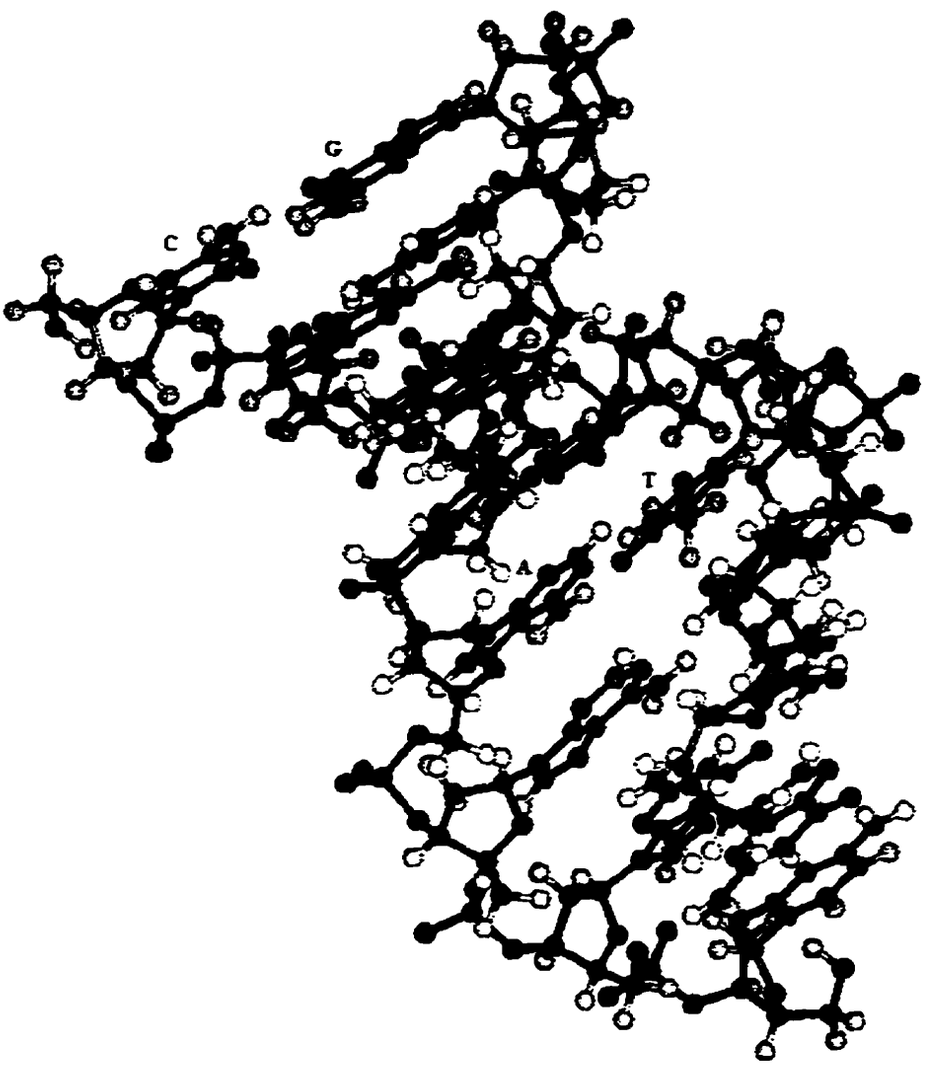

Figure 23
Deoxyoctanucleotide: d(CGAATTCG).d(CGAATTCG)

Table 4
Internal and Symmetry Coordinates of Cytosine-Guanine Base-Pair

Internal Valence Coordinates			Local Symmetry Coordinates		
no.[a]	definition [b]	description [c]	no.[d]	designation [e]	internal coordinate combination [f]
G1	N-H stretch	N(13) - H(15)	G1	-NH_2 asym stretch	$(2^{-1/2})$(1-2)
G2		N(13) - H(16)	G2	-NH_2 sym stretch	$(2^{-1/2})$(1+2)
G3		N(12) - H(14)	G3	-N(12)–H stretch	3
G4		N(1) - H(4)	G4	-N(1)–H stretch	4
G5	C-H stretch	C(2) - H(8)	G5	=C–H stretch	5
G6	C-N stretch	C(10) - N(13)	G6	-C–N(H_2) stretch	6
G7		C(9) - N(12)	G7	-C(O)–N- stretch	7
G8		C(10) - N(12)	G8	=C–N- stretch	8
G9		C(3) - N(7)	G9	-C(C)–N= stretch	9
G10		C(3) - N(1)	G10	=C(C)–N- stretch	10
G11		C(2) - N(1)	G11	=C(C)–N- stretch	11
G12		C(6) - N(5)	G12	=C(C)–N=	12
G13	C-C stretch	C(6) - C(9)	G13	=C(C)–C(O)	13
G14	C=O stretch	C(9) - O(11)	G14	-C=O stretch	14
G15	C=N stretch	C(10) - N(7)	G15	-C(N)=N- stretch	15
G16		C(2) - N(5)	G16	-C=N- stretch	16
G17	C=C stretch	C(3) - C(6)	G17	-C=C- stretch	17
C18	N-H stretch	N(23) - H(27)	C18	-NH_2 asym stretch	$(2^{-1/2})$(18 - 19)
C19		N(23) - H(28)	C19	-NH_2 sym stretch	$(2^{-1/2})$(18+ 19)
C20		N(20) - H(25)	C20	-N–H stretch	20
C21	C-H stretch	C(24) - H(29)	C21	=C–H asym stretch	$(2^{-1/2})$(21 - 22)
C22		C(22) - H(26)	C22	=C–H sym stretch	$(2^{-1/2})$(21 + 22)
C23	C-N stretch	C(18) - N(23)	C23	-C–N(H_2) stretch	23
C24		C(19) - N(20)	C24	-C(O)–N- stretch	24
C25		C(24) - N(20)	C25	=C–N(C)- stretch	25
C26		C(19) - N(17)	C26	-C(O)–N= stretch	26
C27	C-C stretch	C(18) - C(22)	C27	=C–C= stretch	27
C28	C=O stretch	C(19) - O(21)	C28	-C=O stretch	28
C29	C=N stretch	C(18) - N(17)	C29	-C=N- stretch	29
C30	C=C stretch	C(24) - C(22)	C30	-C=C- stretch	30
H31	H-O stretch	H(27) - O(11)	H31	H-O sym stretch	$(2^{-1/2})$(31 + 33)
H32	H-N stretch	H(14) - N(17)	H32	H-O asym stretch	$(2^{-1/2})$(31 - 33)
H33	H-O stretch	H(15) - O(21)	H33	H-N stretch	32
C34	H-N-H bend	α(27-23-28)	C34	-C-N(H_2) i/p wag	$(2^{-1/2})$(43-44)
C35	C-N-H i/p bend	α(18-23-27)	C35	H-N-H scis	$(6^{-1/2})$(2*34-35-36)
C36		α(18-23-28)	C36	H-N-H rock	$(2^{-1/2})$(35-36)
C37		α(19-20-25)	C37	N-H i/p bend	$(2^{-1/2})$(37-38)
C38		α(24-20-25)	C38	=C-H asym bend	(2^{-1})(39-42+41-40)
C39	N-C-H i/p bend	α(20-24-29)	C39	=C-H sym bend	(2^{-1})(39-42-41+40)
C40	C-C-H i/p bend	α(18-22-26)	C40	-C=O i/p wag	$(2^{-1/2})$(45-46)
C41	C=C-H i/p bend	α(24-22-26)	C41	6-ring deform	$(12^{-1/2})$(2*52-51-49+2*47-48-50)
C42		α(22-24-29)	C42	6-ring deform	$(6^{-1/2})$(52-51+49-47+48-50)
C43	N=C-N i/p bend	α(17-18-23)	C43	6-ring deform	(2^{-1})(49-51+50-48)
C44	C-C-N i/p bend	α(22-18-23)	G44	-C-N(H_2) i/p wag	$(2^{-1/2})$(64-65)
C45	N-C=O i/p bend	α(20-19-21)	G45	H-N-H scis	$(6^{-1/2})$(2*53-54-55)
C46		α(17-19-21)	G46	H-N-H rock	$(2^{-1/2})$(54-55)

Table 4 (cont.)

Internal Valence Coordinates			Local Symmetry Coordinates		
no.[a]	definition [b]	description [c]	no.[d]	designation [e]	internal coordinate combination [f]
C47	C-N-C ring bend	α(19-20-24)	G47	N(12)-H i/p bend	$(2^{-1/2})$(56-57)
C48	N-C-N ring bend	α(20-19-17)	G48	N(1)-H i/p bend	$(2^{-1/2})$(58-59)
C49	C=C-N ring bend	α(20-24-22)	G49	=C-H i/p bend	$(2^{-1/2})$(60-61)
C50	C=N-C ring bend	α(19-17-18)	G50	-C=O i/p wag	$(2^{-1/2})$(62-63)
C51	C=C-C ring bend	α(24-22-18)	G51	6-ring deform	$(12^{-1/2})$(2*66-74-69+2*72-70-67)
C52	N=C-C ring bend	α(17-18-22)	G52	6-ring deform	$(6^{-1/2})$(66-74+69-72+70-67)
G53	H-N-H bend	α(15-13-16)	G53	6-ring deform	(2^{-1})(69-74+67-70)
G54	C-N-H i/p bend	α(10-13-15)	G54	5-ring deform	$(2^{-1/2})$(73-68)
G55		α(10-13-16)	G55	5-ring deform	$(6^{-1/2})$(2*71-68-73)
G56		α(9-12-14)	G56	H-N-H sym torsion	84-85
G57		α(10-12-14)	G57	H-N-H asym torsion	84+85
G58		α(2-1-4)	G58	6-ring bend	$(12^{-1/2})$(2*75-76-80+2*81-82-83)
G59		α(3-1-4)	G59	6-ring	$(6^{-1/2})$(75-76+80-81+82-83)
G60	N-C-H i/p bend	α(1-2-8)	G60	6-ring twist	(2^{-1})(80-76+83-82)
G61	N=C-H i/p bend	α(5-2-8)	G61	5-ring twist	$(2^{-1/2})$(77-79)
G62	N-C=O i/p bend	α(12-9-11)	G62	5-ring bend	$(6^{-1/2})$(2*78-77-79)
G63	C-C=O i/p bend	α(6-9-11)	G63	butterfly	(2^{-1})(75+77+79+81)
G64	N-C-N i/p bend	α(12-10-13)	C64	6-ring bend	$(12^{-1/2})$(2*86-87-88+2*89-90-91)
G65	N=C-N i/p bend	α(7-10-13)	C65	6-ring	$(6^{-1/2})$(86-87+88-89+90-91)
G66	C-C-N ring bend	α(6-9-12)	C66	6-ring twist	(2^{-1})(88-87+91-90)
G67	N-C-N ring bend	α(9-12-10)	C67	H-N-H sym torsion	$(2^{-1/2})$(92-93)
G68	C-N-C ring bend	α(2-1-3)	C68	H-N-H asym torsion	$(2^{-1/2})$(92+93)
G69	C=C-N ring bend	α(6-3-7)	H69	H-O sym torsion	$(2^{-1/2})$(94+96)
G70	N=C-N ring bend	α(7-10-12)	H70	H-O asym torsion	$(2^{-1/2})$(94-96)
G71		α(5-2-1)	H71	H-N torsion	95
G72	C=N-C ring bend	α(10-7-3)	C72	N-H o/p bend	98
G73		α(2-5-6)	C73	C-H asym o/p bend	$(2^{-1/2})$(99-100)
G74	C=C-C ring bend	α(3-6-9)	C74	C-H sym o/p bend	$(2^{-1/2})$(99+100)
G75	C(10)-N(12) ring	τ(7-10-12-9)	C75	C=O o/p bend	101
G76	N(12)-C(9) ring	τ(10-12-9-6)	C76	H-N-H inversion	97
G77	C(9)-C(6) ring	τ(12-9-6-5)	G77	N(12)-H o/p bend	103
G78	C(6)-N(5) ring	τ(9-6-5-2)	G78	N(1)-H o/p bend	104
G79	N(5)=C(2) ring	τ(6-5-2-1)	G79	C-H o/p bend	105
G80	C(2)-N(1) ring	τ(5-2-1-3)	G80	C=O o/p bend	106
G81	N(1)-C(3) ring	τ(2-1-3-7)	G81	H-N-H inversion	102
G82	C(3)-N(7) ring	τ(1-3-7-10)			
G83	N(7)=C(10) ring	τ(3-7-10-12)			
G84	N(13)-H torsion	τ(7-10-13-16)			
G85		τ(12-10-13-15)			
C86	C(19)-N(17) ring	τ(20-19-17-18)			
C87	N(17)=C(18) ring	τ(19-17-18-22)			
C88	C(18)-C(22) ring	τ(17-18-22-24)			
C89	C(22)=C(24) ring	τ(18-22-24-20)			
C90	C(24)-N(20) ring	τ(22-24-20-19)			
C91	N(20)-C(19) ring	τ(24-20-19-17)			
C92	N(23)-H torsion	τ(17-18-23-27)			
C93		τ(22-18-23-28)			
H94	C-C-O-H torsion	τ(6-9-11-27)			

Table 4 (cont.)

Internal Valence Coordinates		
no.[a]	definition [b]	description [c]
H95	C-C-N-H torsion	τ(22-18-17-14)
H96	N-C-O-H torsion	τ(20-19-21-15)
C97	N-H_2 inversion	γ(18-27-28-23)
C98	N(1)-H o/p bend	γ(25-19-24-20)
C99	C-H o/p bend	γ(29-20-22-24)
C100		γ(26-24-18-22)
C101	C=O o/p bend	γ(21-20-17-19)
G102	N-H_2 inversion	γ(10-15-16-13)
G103	N(12)-H o/p bend	γ(14-9-10-12)
G104	N(1)-H o/p bend	γ(4-2-3-1)
G105	C-H o/p bend	γ(8-1-5-2)
G106	C=O o/p bend	γ(11-6-12-9)

[a] Internal valence coordinate numbers where C, G and H refer to cytosine, guanine and the hydrogen bond, respectively.

[b] i/p = in-plane, o/p = out-of-plane.

[c] Atom numbers of C and G in parenthesis see Figure 3, page 10; α = bending-in-plane, γ = bending-out-of-plane, τ = twisting.

[d] Local symmetry coordinate numbers where C, G and H refer to cytosine, guanine and the hydrogen bond, respectively.

[f] sym = symmetric, asym = antisymmetric, scis = scissors

[e] Normalization constants followed by internal valence coordinate numbers (both in parenthesis).

Table 5
Potential Energy Distribution of Deuterated Cytosine-Guanine Base-Pair

Mode [a]	Calculated B3-LYP/6-31G** $\bar{\nu}$ (cm^{-1}) x 0.95 [b]	A (km mol^{-1}) [c]	% (Local Symmetry Coordinate) [d]
Q11(cg)	1671	1310	17(C26), 14(C28), 13(C42), 12(C43)
Q12(cg)	1652	179	23(H31),15(G14), 11(C42), 10(G53)
Q13(cg)	1612	560	25(C41), 17(C30), 13(C29)
Q14(cg)	1541	585	42(G53), 10(G7), 10(G6)
Q15(cg)	1528	3	27(G9), 18(G17), 14(G52), 14(G44)
Q16(cg)	1493	56	18(C23), 17(C42), 14(C29)
Q17(cg)	1489	66	20(G8), 17(G44), 13(G52), 10(G53)
Q18(cg)	1462	168	38(C29), 20(C34), 18(C43)
Q19(cg)	1451	24	36(G8), 16(G44)
Q20(cg)	1351	34	30(G8), 24(G44), 16(G17)
Q21(cg)	1338	48	27(C34), 19(C29), 12(C40), 11(C38)
Q22(cg)	1298	45	25(G50), 17(G51), 13(G7), 12(G8), 10(G44)
Q23(cg)	1282	53	23(C40), 18(C26), 16(C34), 10(C25)
Q24(cg)	1268	7	26(G17), 21(G7)
Q25(cg)	1255	60	43(C26), 16(C40), 15(C29)
Q26(cg)	1245	19	35(G8), 31(G7)
Q27(cg)	1207	3	25(G44), 21(G7), 18(G9), 15(G8)
Q28(cg)	1151	20	28(C40), 22(C26), 13(C42)
Q29(cg)	1121	10	40(G7), 22(H33), 17(G50)
Q30(cg)	1114	52	34(G52), 20(H33), 20(G7), 12(G50)
Q31(cg)	1108	6	39(C42), 24(C39), 14(C40)
Q32(cg)	1050	7	40(G50), 18(G53), 18(H33), 13(G7)
Q33(cg)	986	35	34(C40), 32(H33), 14(C34)
Q34(cg)	962	8	24(G8), 13(G44), 12(H33), 11(G7)
Q35(cg)	933	4	42(H33), 42(C42)
Q36(cg)	912	1	76(C73), 11(C65)
Q37(cg)	896	5	35(H33), 22(G17), 13(G53), 10(G10)
Q38(cg)	884	10	30(H33), 23(C42), 22(C34), 11(C40)
Q39(cg)	850	1	47(H33), 11(G44), 11(G50), 10(G8)

[a] Q(cg) represents the normal modes of the deuterated C-G base-pair.

[b] Wavenumbers calculated with the B3-LYP/6-31G** procedure.

[c] Intensities calculated with the B3-LYP/6-31G** procedure.

[d] Local symmetry coordinates defined in Table 4.

Table 6
Internal and Symmetry Coordinates of Adenine-Thymine Base-Pair

Internal Valence Coordinates			Local Symmetry Coordinates		
no.[a]	definition [b]	description [c]	no.[d]	designation [e]	internal coordinate combination [f]
A1	N-H stretch	N(1) - H(4)	A1	-N–H stretch	1
A2		N(11) - H(14)	A2	$-NH_2$ asym stretch	$(2^{-1/2})(2-3)$
A3		N(11) - H(15)	A3	$-NH_2$ sym stretch	$(2^{-1/2})(2+3)$
A4	C-H stretch	C(2) - H(8)	A4	=C–H stretch	4
A5		C(10) - H(13)	A5	=C–H stretch	5
A6	C-N stretch	C(9) - N(11)	A6	-C–N(H_2) stretch	6
A7		C(3) - N(7)	A7	=C(C)–N= stretch	7
A8		C(10) - N(12)	A8	=C–N= stretch	8
A9		C(6) - N(5)	A9	=C(C)–N= stretch	9
A10		C(3) - N(1)	A10	=C(C)–N- stretch	10
A11		C(2) - N(1)	A11	=C–N- stretch	11
A12	C-C stretch	C(6) - C(9)	A12	=C(C)–C(NH_2) stretch	12
A13	C=N stretch	C(2) - N(5)	A13	-C(N)=N- stretch	13
A14		C(9) - N(12)	A14	-C(C)=N- stretch	14
A15		C(10) - N(7)	A15	-C(N)=N- stretch	15
A16	C=C stretch	C(3) - C(6)	A16	-C=C- stretch	16
T17	N-H stretch	N(16) - H(19)	T17	-N–H stretch	17
T18		N(21) - H(25)	T18	-N–H stretch	18
T19	C-H stretch	C(24) - H(27)	T19	=C–H stretch	19
T20		C(26) - H(28)	T20	$-CH_3$ asym stretch	$(6^{-1/2})(2*20-21-22)$
T21		C(26) - H(29)	T21	$-CH_3$ asym stretch	$(2^{-1/2})(21-22)$
T22		C(26) - H(30)	T22	$-CH_3$ sym stretch	$(3^{-1/2})(20+21+22)$
T23	C-N stretch	C(17) - N(21)	T23	-C(O) –N- stretch	23
T24		C(24) - N(21)	T24	=C–N(C)- stretch	24
T25		C(17) - N(16)	T25	-C(O)–N- stretch	25
T26		C(18) - N(16)	T26	-C(O)–N - stretch	26
T27	C-C stretch	C(22) - C(18)	T27	=C–C(O) stretch	27
T28		C(22) - C(26)	T28	=C–CH_3 stretch	28
T29	C=O stretch	C(17) - O(20)	T29	-C=O	29
T30		C(18) - O(23)	T30	-C=O	30
T31	C=C stretch	C(24) - C(22)	T31	-C=C-	31
H32	H-O stretch	H(14)-O(23)	H32	H-O stretch	32
H33	H-N stretch	H(19)-N(12)	H33	H-N stretch	33
H34	H-O stretch	H(13)-O(20)	H34	O-H stretch	34
T35	H-C-H bend	α(28-26-30)	T35	-C–H (Me) asym	$(6^{-1/2})(2*35-36-37)$
T36	H-C-H bend	α(28-26-29)	T36	-C–H (Me) asym	$(2^{-1/2})(36-37)$
T37	H-C-H bend	α(29-26-30)	T37	-C–H (Me) sym deform	$(3^{-1/2})(35+36+37)$
T38	C-N-H i/p bend	α(18-16-19)	T38	-N–H i/p bend	$(2^{-1/2})(38-39)$
T39		α(17-16-19)	T39	-N–H i/p bend	$(2^{-1/2})(40-41)$
T40		α(17-21-25)	T40	=C–H i/p bend	$(2^{-1/2})(42-43)$
T41		α(24-21-25)	T41	-C=O i/p wag	$(2^{-1/2})(44-47)$
T42	N-C-H i/p bend	α(21-24-27)	T42	-C=O i/p wag	$(2^{-1/2})(45-46)$
T43	C=C-H i/p bend	α(22-24-27)	T43	=C–CH_3 wag	$(2^{-1/2})(48-49)$
T44	N-C=O i/p bend	α(16-18-23)	T44	$-CH_3$ i/p rock	$(6^{-1/2})(2*50-51-52)$
T45		α(16-17-20)	T45	$-CH_3$ o/p rock	$(6^{-1/2})(2*52-50-51)$
T46		α(21-17-20)	T46	6-ring deform	$(12^{-1/2})(2*58-57-56+2*53-55-54)$

Table 6 (cont.)

Internal Valence Coordinates			Local Symmetry Coordinates		
no.[a]	definition [b]	description [c]	no.[d]	designation [e]	internal coordinate combination [f]
T47	C-C=O	α(22-18-23)	T47	6-ring deform	$(6^{-1/2})$(58-57+56-53+55-54)
T48	C-C-C	α(18-22-26)	T48	6-ring deform	(2^{-1})(56-57+54-55)
T49	C=C-C	α(24-22-26)	A49	-C-N(H_2) i/p wag	$(2^{-1/2})$(68-69)
T50	C-C-H (Me) bend	α(22-26-28)	A50	H-N-H scis	$(6^{-1/2})$(2*59-60-61)
T51		α(22-26-29)	A51	H-N-H rock	$(2^{-1/2})$(60-61)
T52		α(22-26-30)	A52	N-H i/p bend	$(2^{-1/2})$(62-63)
T53	C-N-C ring bend	α(17-21-24)	A53	=C(2)-H i/p bend	$(2^{-1/2})$(64-66)
T54		α(17-16-18)	A54	=C(10)-H i/p bend	$(2^{-1/2})$(65-67)
T55	N-C-N ring bend	α(21-17-16)	A55	6-ring deform	$(12^{-1/2})$(2*72-78-71+2*76-73-77)
T56	C=C-N ring bend	α(22-24-21)	A56	6-ring deform	$(6^{-1/2})$(72-78+71-76+73-77)
T57	C=C-C ring bend	α(24-22-18)	A57	6-ring deform	(2^{-1})(71-78+77-73)
T58	C-C-N ring bend	α(22-18-16)	A58	5-ring deform	$(2^{-1/2})$(75-70)
A59	H-N-H bend	α(14-11-15)	A59	5-ring deform	$(6^{-1/2})$(2*74-70-75)
A60	C-N-H i/p bend	α(9-11-14)	A60	6-ring bend	$(12^{-1/2})$(2*82-83-87+2*88-89-90)
A61		α(9-11-15)	A61	6-ring pseudorotation	$(6^{-1/2})$(82-83+87-88+89-90)
A62		α(2-1-4)	A62	6-ring twist	(2^{-1})(87-83+90-89)
A63		α(3-1-4)	A63	5-ring twist	$(2^{-1/2})$(84-86)
A64	N-C-H i/p bend	α(1-2-8)	A64	5-ring bend	$(6^{-1/2})$(2*85-84-86)
A65		α(12-10-13)	A65	butterfly	(2^{-1})(82+84+86+88)
A66	N=C-H i/p bend	α(5-2-8)	A66	H-N-H sym torsion	91-92
A67		α(7-10-13)	A67	H-N-H asym torsion	91+92
A68	N=C-N i/p bend	α(12-9-11)	T68	6-ring bend	$(12^{-1/2})$(2*93-94-95+2*96-97-98)
A69	C-C-N i/p bend	α(6-9-11)	T69	6-ring pseudoraotation	$(6^{-1/2})$(93-94+95-96+97-98)
A70	C-N-C ring bend	α(2-1-3)	T70	6-ring twist	(2^{-1})(95-94+98-97)
A71	C=C-N ring bend	α(6-3-7)	T71	H-C-H (Me) torsion	99
A72	N=C-C ring bend	α(12-9-6)	H72	C-C-O-H torsion	79
A73	N=C-N ring bend	α(7-10-12)	H73	C-C-O-H torsion	80
A74		α(5-2-1)	H74	N-C-O-H torsion	81
A75	C=N-C ring bend	α(2-5-6)	T75	C-CH_3 o/p bend	100
A76		α(10-7-3)	T76	N–H o/p bend	101
A77		α(9-12-10)	T77	N–H o/p bend	102
A78	C=C-C ring bend	α(3-6-9)	T78	C–H o/p bend	103
H79	C-C-O-H torsion	τ(22-18-23-14)	T79	C=O o/p bend	104
H80	C-C-N-H torsion	τ(6-9-12-19)	T80	C=O o/p bend	105
H81	N-C-O-H torsion	τ(21-17-20-13)	A81	N-H o/p bend	107
A82	C(10)=N(12) ring	τ(7-10-12-9)	A82	C-H o/p bend	108
A83	N(12)-C(9) ring	τ(10-12-9-6)	A83	C-H o/p bend	109
A84	C(9)=C(6) ring	τ(12-9-6-5)	A84	H-N-H inversion	106
A85	C(6)-N(5) ring	τ(9-6-5-2)			
A86	N(5)=C(2) ring	τ(6-5-2-1)			
A87	C(2)-N(1) ring	τ(5-2-1-3)			
A88	N(1)-C(3) ring	τ(2-1-3-7)			
A89	C(3)=N(7) ring	τ(1-3-7-10)			
A90	N(7)-C(10) ring	τ(3-7-10-12)			
A91	N(11)-H torsion	τ(6-9-11-15)			
A92		τ(12-9-11-14)			
T93	C(17)-N(16) ring	τ(21-17-16-18)			
T94	N(16)=C(18) ring	τ(17-16-18-22)			

Table 6 (cont.)

Internal Valence Coordinates		
no.[a]	definition [b]	description [c]
T95	C(18)-C(22) ring	τ(16-18-22-24)
T96	C(22)=C(24) ring	τ(18-22-24-21)
T97	C(24)-N(21) ring	τ(22-24-21-17)
T98	N(21)-C(17) ring	τ(24-21-17-16)
T99	$C-H_3$ torsion	τ(24-22-26-28)
		τ(18-22-26-29)
		τ(24-22-26-30)
T100	$C-CH_3$ o/p bend	γ(26-24-18-22)
T101	N-H o/p bend	γ(25-17-24-21)
T102		γ(19-17-18-16)
T103	C-H o/p bend	γ(27-21-22-24)
T104	C=O o/p bend	γ(20-21-16-17)
T105		γ(23-16-22-18)
A106	$N-H_2$ inversion	γ(9-14-15-11)
A107	N-H o/p bend	γ(4-2-3-1)
A108	C-H o/p bend	γ(8-1-5-2)
A109		γ(13-7-12-10)

[a] Internal valence coordinate numbers where A, T and H refer to adenine, thymine and the hydrogen bond, respectively.

[b] i/p = in-plane, o/p = out-of-plane.

[c] Atom numbers of A and T in parenthesis see Figure 3, page 10; α = bending-in-plane, γ = bending-out-of-plane, τ = twisting.

[d] Local symmetry coordinate numbers where A, T and H refer to adenine, thymine and the hydrogen bond, respectively.

[f] sym = symmetric, asym = antisymmetric, scis = scissors

[e] Normalization constants followed by internal valence coordinate numbers (both in parenthesis).

Table 7
Potential Energy Distribution of Adenine-Thymine Base-Pair

Mode [a]	Calculated B3-LYP/6-31G** $\bar{\nu}$ (cm^{-1}) x 0.95 [b]	A ($km\ mol^{-1}$) [c]	% (Local Symmetry Coordinate) [d]
Q12(at)	1719	476	49(T29), 15(T25), 12(T48)
Q13(at)	1643	595	37(T30), 14(T46), 12(T31)
Q14(at)	1618	24	47(T31), 19(T30)
Q15(at)	1581	423	17(A12), 15(A6), 13(A54), 12(A55)
Q16(at)	1544	63	24(A7), 19(A57), 13(A14), 10(A49)
Q17(at)	1479	32	36(A54), 12(A6), 12(H34)
Q18(at)	1447	47	25(A13), 19(A54), 10(A58)
Q19(at)	1435	26	46(T36), 15(T35), 10(T44)
Q20(at)	1410	6	69(T35), 23(T36)
Q21(at)	1404	136	26(T48), 14(T26), 13(T41)
Q22(at)	1383	14	43(A54), 21(H34), 11(A16)
Q23(at)	1362	2	89(T37)
Q24(at)	1332	13	38(A54), 28(H34)
Q25(at)	1311	37	22(T42), 22(T25), 12(T40)
Q26(at)	1307	23	33(A8), 15(A14), 14(A9), 10(A16)
Q27(at)	1292	73	36(H34), 16(A54), 12(A15)
Q28(at)	1289	46	23(T25)
Q29(at)	1272	51	17(A11), 15(A8), 12(A53)
Q30(at)	1231	4	38(T26), 17(T24), 14(T25), 10(T38)
Q31(at)	1187	10	24(H34), 17(A11), 12(A54)
Q32(at)	1163	6	18(T42), 16(T47), 13(T28), 12(T25)
Q33(at)	1158	23	24(H33), 21(A49), 12(A14), 10(A8)
Q34(at)	1146	57	39(A50), 22(A56)
Q35(at)	1082	28	23(T41), 21(T26), 12(T38), 10(T42)
Q36(at)	1064	22	21(A58), 10(A10), 10(A49)
Q37(at)	1017	2	73(T45)
Q38(at)	1002	22	44(T44), 11(T45)
Q39(at)	948	2	37(A83), 36(A60), 20(A65)
Q40(at)	902	2	19(T39), 16(T44), 11(T24)
Q41(at)	901	6	39(A59), 11(A11)
Q42(at)	873	33	49(H33), 22(A56)
Q43(at)	866	14	83(T78)
Q44(at)	861	21	21(T47), 20(A56)

[a] Q(at) represents the normal modes of the deuterated A-T base-pair.

[b] Wavenumbers calculated with the B3-LYP/6-31G** procedure.

[c] Intensities calculated with the B3-LYP/6-31G** procedure.

[d] Local symmetry coordinates defined in Table 4.

Table 8
Calculated wavenumbers for the DNA Sugar-Phosphate Backbone

1-Amino-Deoxyribose

Mode [a]	Calculated B3-LYP/6-31G**	
	$\bar{\nu}$ (cm^{-1}) x 0.95 [b]	A (km mol^{-1}) [c]
Q12(d)	1438	6
Q13(d)	1414	5
Q14(d)	1359	11
Q15(d)	1355	32
Q16(d)	1333	18
Q17(d)	1327	9
Q18(d)	1295	7
Q19(d)	1277	11
Q20(d)	1262	0.3
Q21(d)	1232	9
Q22(d)	1211	2
Q23(d)	1199	48
Q24(d)	1164	10
Q25(d)	1093	74
Q26(d)	1073	64
Q27(d)	1057	46
Q28(d)	1043	59
Q29(d)	1037	30
Q30(d)	998	67
Q31(d)	961	29
Q32(d)	922	34
Q33(d)	908	17
Q34(d)	885	5

Dimethyl Phosphate Anion

Mode [a]	Calculated B3-LYP/6-31G**	
	$\bar{\nu}$ (cm^{-1}) x 0.95 [b]	A (km mol^{-1}) [c]
Q7(dmp)	1443	3
Q8(dmp)	1439	1
Q9(dmp)	1428	1
Q10(dmp)	1424	6
Q11(dmp)	1412	11
Q12(dmp)	1408	3
Q13(dmp)	1255	237
Q14(dmp)	1149	7
Q15(dmp)	1143	10
Q16(dmp)	1125	1
Q17(dmp)	1122	0.3
Q18(dmp)	1057	20
Q19(dmp)	1044	293
Q20(dmp)	1038	237

[a] Q(d) and Q(dmp) represent the normal modes of 1-amino-deoxyribose and dimethyl phosphate, respectively.

[b] Wavenumbers calculated with the B3-LYP/6-31G** procedure.

[c] Intensities calculated with the B3-LYP/6-31G** procedure.

vibrational assignments which could be due to the difference in internal valence coordinate definitions. This work reveals more mixing between the C and G nucleotide base components in the C-G base-pair which can be considered to be more accurate since the B3-LYP procedure incorporates Becke's three parameter hybrid functional that consists of HF plus non-local exchange and correlation parts (Sponer *et al.*, 1996). The results of the dimethyl phosphate anion calculated with the B3-LYP/6-31G** method (see Table 8) compare favorably with those of the sodium dimethyl phosphate reported with B3-LYP/6-31G* studies (Florian *et al.*, 1996). At this level of theory, there is no literature available for a comparison of the 1-amino-deoxyribose (see Table 8) and the A-T base-pair. However, the efficiency of B3-LYP in evaluating molecular structure, vibrational wavenumbers and IR intensities (Sponer *et al.*, 1996) and the favorable correspondence with previous literature consolidates the reliability of calculations in this study.

5.1.3 Simulation of Infrared Absorption spectra

Due to the size of the deoxyoctanucleotide molecular systems, a component approach was adopted as a first approximation to generate the absorption spectra of the selected deoxyoctanucleotides which entailed summing the *ab initio* computed spectra of the separate nucleotide components, i.e. fourteen phosphate residues, sixteen deoxyribose residues and the appropriate number of nucleotide bases or base-pairs.

The wavenumbers labeling absorption positions in the calculated IR absorption spectra (see Figure 24, page 79 to Figure 27, page 82) have been picked with the Labcalc (Lab Calc C2.24, 1992) computer program, hence they may not correspond precisely with those calculated (see Table 5, page 71; Table 7, page 75 and Table 8, page 76). The above mentioned tables also list the vibrational assignments of the various fundamental modes. Certain deoxyoctanucleotides have an equivalent composition even though they differ in sequence. For example d(CGCATGCG).d(CGCATGCG) and d(CGCTAGCG). d(CGCTAGCG) (see Figure 25, page 80) produce indistinguishable simulated IR absorption spectra when calculated with the component approach. Similarly d(CGATATCG).d(CGATATCG), d(CGTATACG). d(CGTATACG) (see Figure 26,

page 81) and d(CGAATTCG).d(CGAATTCG) (see Figure 27, page 82) possess identical simulated IR absorption spectra. The last mentioned deoxyoctanucleotide is displayed separately because its experimental IR absorption spectrum differs significantly from the other two.

With the component approach IR absorption spectra can be calculated in two ways, i.e. on the basis of nucleotide *base* or *base-pair* components being added to the sugar-phosphate backbone components as illustrated in Figure 24, page 79 to Figure 27, page 82. The summation of the base-pairs rather than the single bases reproduce the experimental IR absorption spectra more accurately for all the deoxyoctanucleotides. This emphasizes the significance of taking into account the mechanical coupling between the nucleotide bases in a base-pair (chromophore), because there are several intense transition dipole moments in the base-pair which are close together and couple in a complicated manner. When applying the purely electrostatic NECO model for simulating IR/VCD spectra of deoxyoctanucleotides and their daunorubicin complexes, transition dipole moments between base-pairs rather than within base-pairs are coupled.

The A-T base-pair gives rise to a band at 1718 cm^{-1} in the calculated IR absorption spectra which is shifted in the experimental IR absorption spectra (see Figure 24, page 79 to Figure 27, page 82). This could probably be attributed to solvent effects in the experimental IR spectra, which cause the 1718 cm^{-1} peak to shift to a lower wavenumber, suggesting that the carbonyl group, $C_{(17)}=O_{(20)}$, in the A-T base-pair (see Figure 3, page 10) is hydrogen-bonded in the deoxyoctanucleotides. While gas phase calculations are not ideal for solution studies, for the most part IR spectra in the 1750-850 cm^{-1} region are relatively insensitive to environment. However, hydrogen bonds do cause wavenumbers to shift to lower energy but we assume that the electric transition dipole moments are transferable.

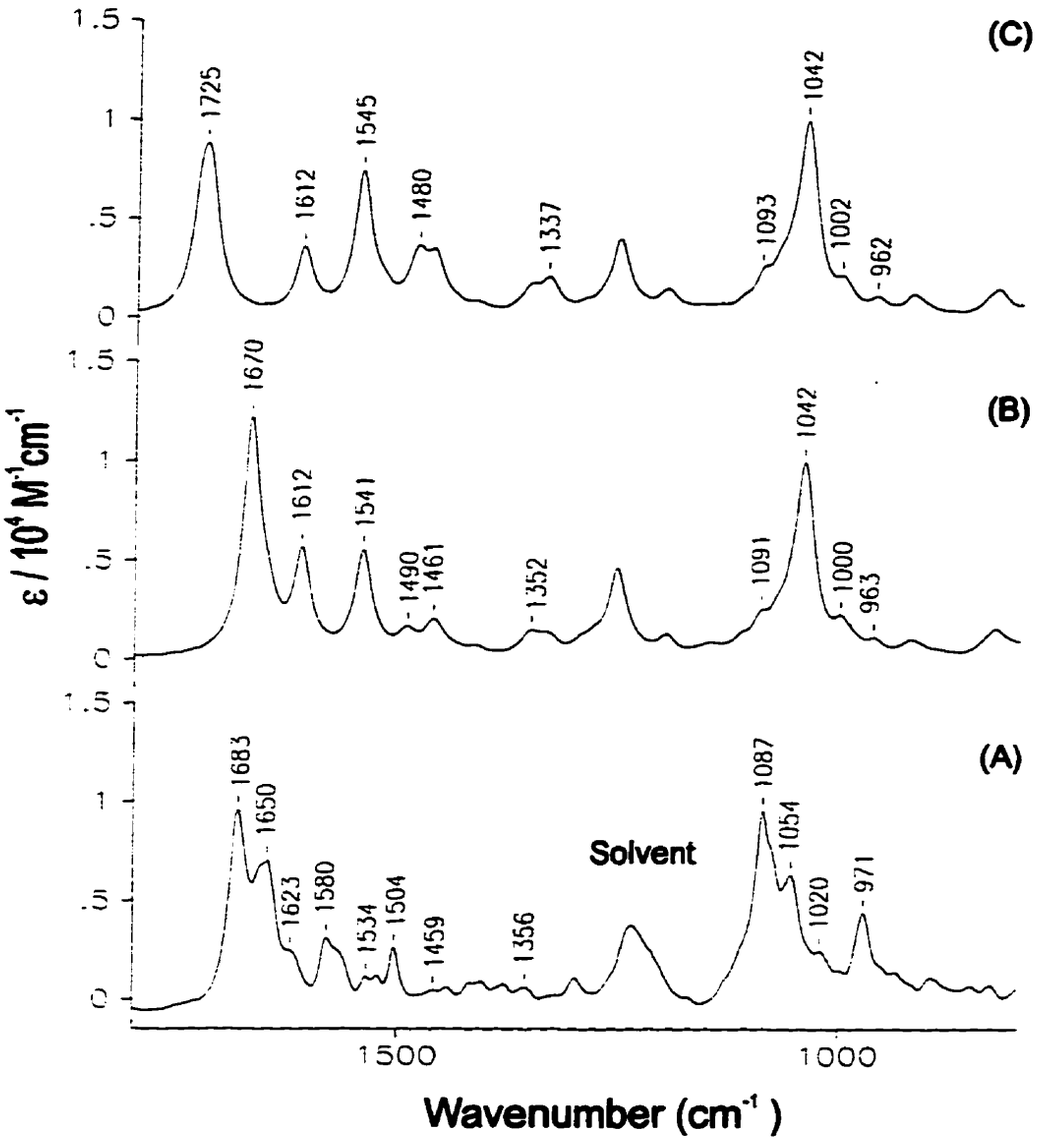

Figure 24
Experimental and Calculated IR Absorption Spectra of d(CGCGCGCG).d(CGCGCGCG)

Experimental IR absorption spectra (A) and calculated with base-pairs (B) and bases (C).

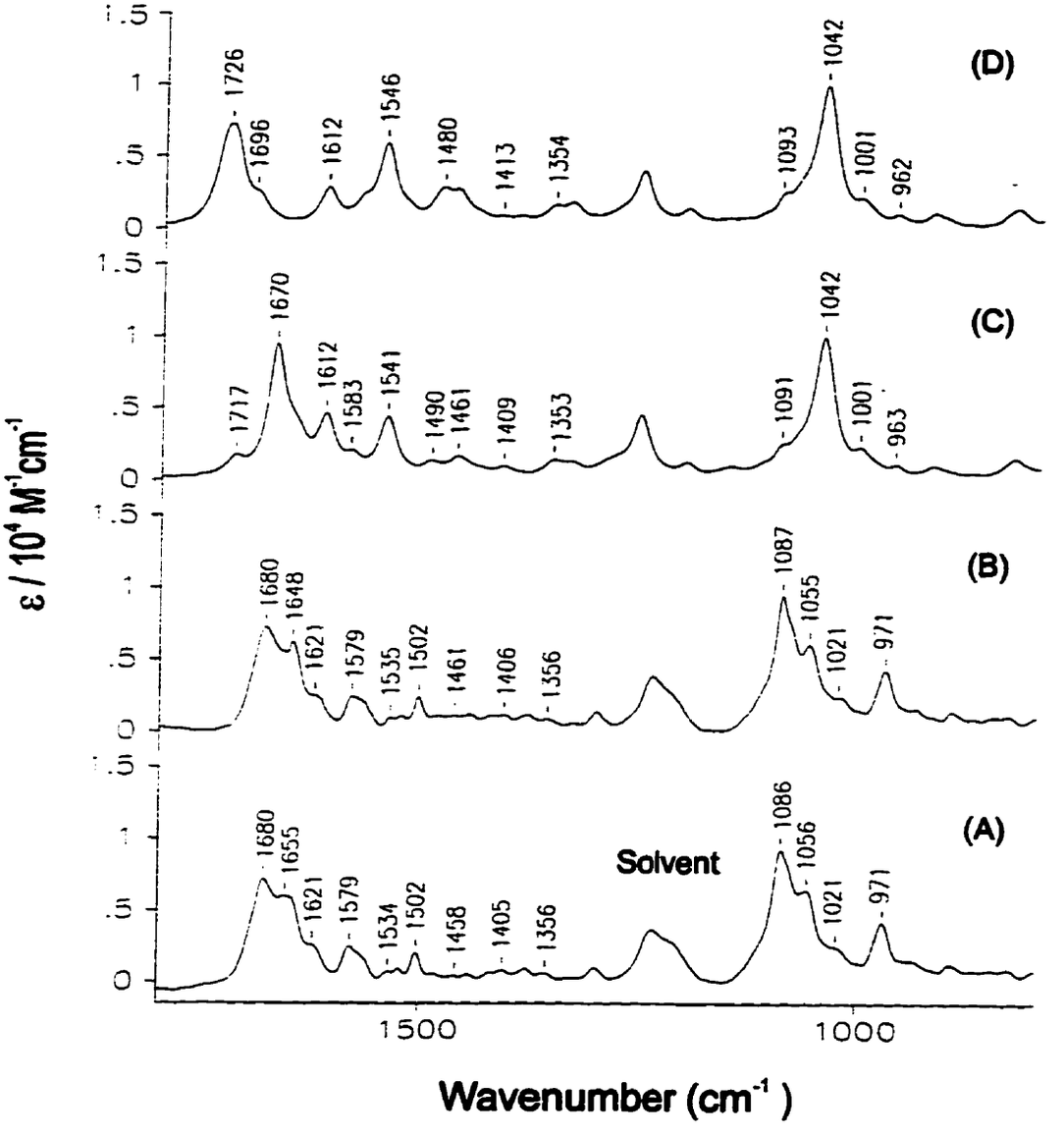

Figure 25
Experimental and Calculated IR Absorption Spectra of d(CGCTAGCG).d(CGCTAGCG) and d(CGCATGCG).d(CGCATGCG)

Experimental IR absorption spectra d(CGCTAGCG).d(CGCTAGCG) (A), d(CGCATGCG).d(CGCATGCG) (B) and calculated with base-pairs (C) and bases (D).

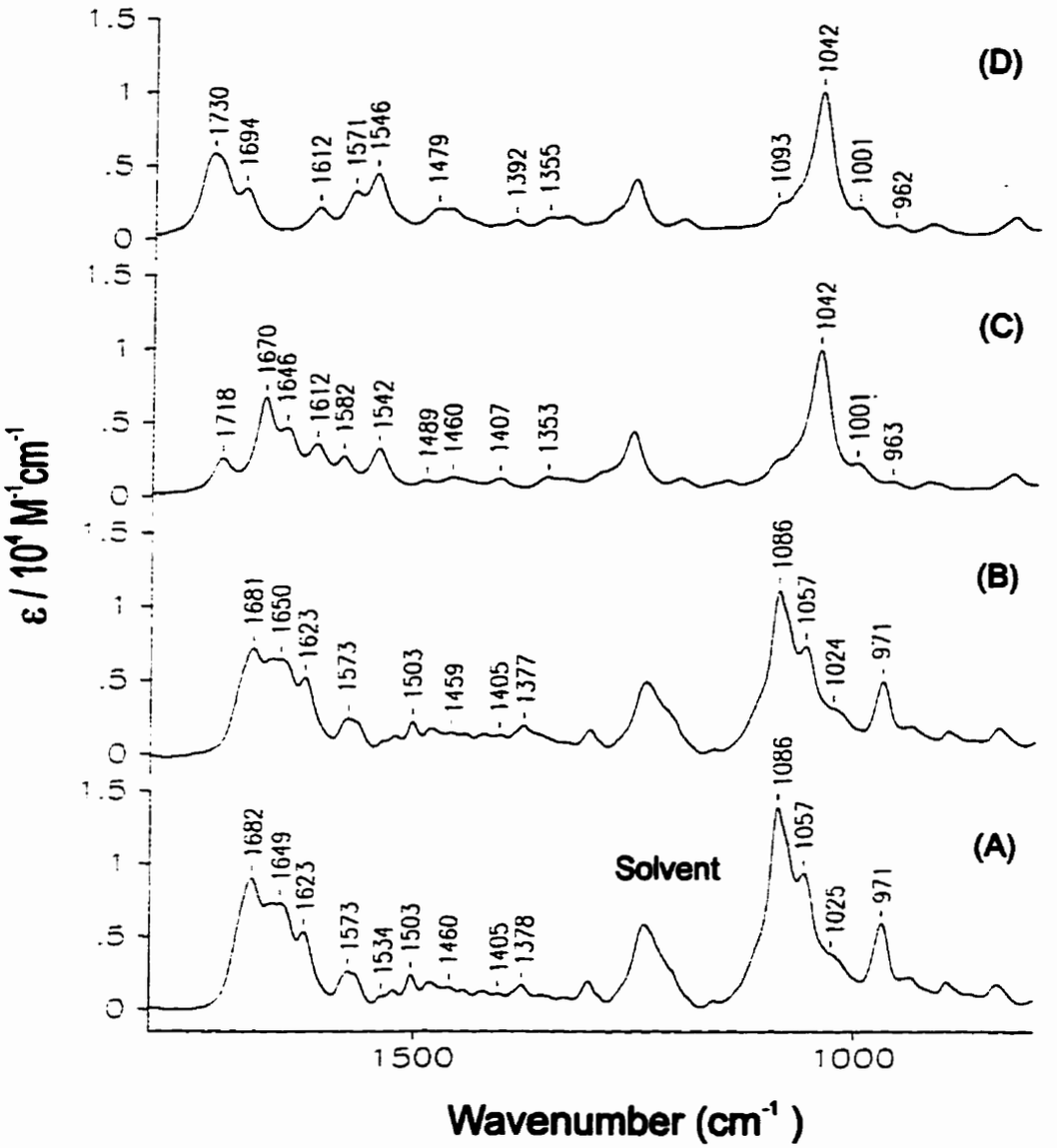

Figure 26
Experimental and Calculated IR Absorption Spectra of d(CGTATACG).d(CGTATACG) and d(CGATATCG).d(CGATATCG)

Experimental IR absorption spectra d(CGTATACG).d(CGTATACG) (A), d(CGATATCG).d(CGATATCG) (B) and calculated with base-pairs (C) and bases (D).

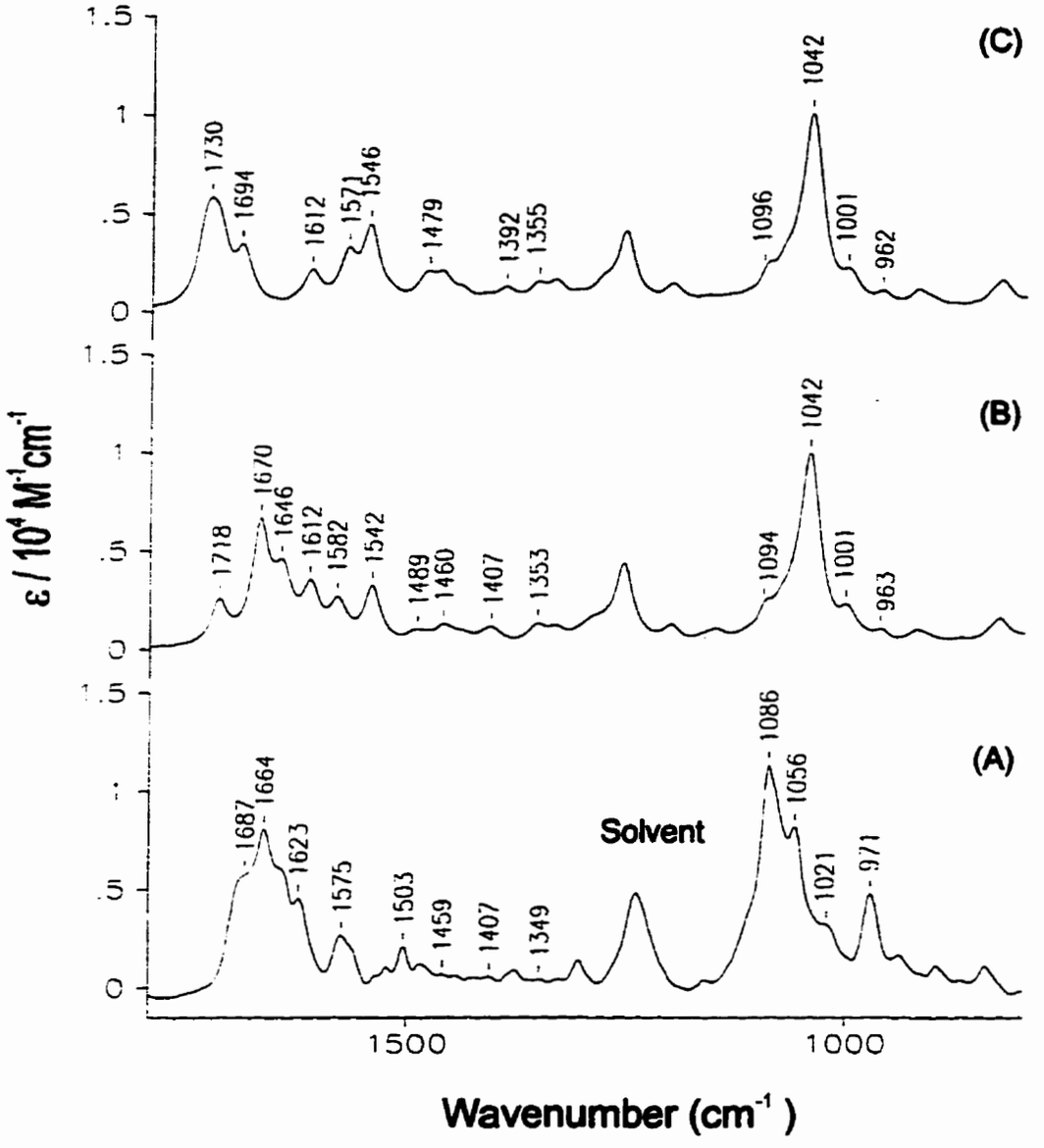

Figure 27
Experimental and Calculated IR Absorption Spectra of d(CGAATTCG).d(CGAATTCG)

Experimental IR absorption spectra (A) and calculated with base-pairs (B) and bases (C).

5.2 The Coupled Oscillator Model

The IR/UV absorption and VCD/ECD spectra are calculated using the approximate non-degenerate extended coupled oscillator (NECO) model. The coupled oscillator model and its modifications are described in detail elsewhere (Rauk & Freedman, 1994; Xiang *et al.*, 1993). The model was used to determine the optical activity of biopolymers consisting of degenerate or near degenerate chromophores (Xiang *et al.*, 1993). The underlying theory is based on the exciton model where the excited state of a polymer is delocalized over all the monomers. This delocalized excitation is referred to as an "exciton". The excited state wavefunction was written in terms of the dipolar interactions (Moffitt, 1956), and relevant equations were then applied to derive expressions for the dipole and rotational strengths for two and infinitely many interacting dipoles (Tinoco, 1963). The first application of the coupled oscillator method to VCD was demonstrated with diketopiperazines, formed by cyclic dimerization of amino acids (Holzwarth & Chabay, 1972).

Each fundamental vibrational mode of a monomer gives rise to an oscillator which can in principle couple intramolecularly with all other dipole oscillators in the polymer. This coupling depends on the separation and angles between the oscillators, and their relative magnitudes. It is essential, therefore, to know the magnitude and orientation of the transition dipole vectors explicitly. A non-linear, non-planar arrangement gives rise to magnetic dipole transition moments which are used to calculate rotational strengths. The NECO model was adopted in the more recent literature of nucleic acid VCD simulations (Gulotta *et al.*, 1989; Xiang *et al.*, 1993) and was therefore implemented in this study.

5.2.1 NECO Theory

In the NECO description of N interacting dipoles, the absorption intensities can be obtained from the dipole strength D [Debye^2], for the kth exciton component ($1 \leq k \leq N$), defined by:

$$D_k = \sum_{i=1}^{N}\sum_{j=1}^{N} c_{ik}c_{jk}\left(\bar{\mu}_i \cdot \bar{\mu}_j\right) \tag{12}$$

where c_{ij} are the eigenvector components of the dipolar interaction matrix, V_{ij} [cm^{-1}]:

$$V_{ij} = \frac{5034}{\varepsilon_d}\left\langle \frac{\bar{\mu}_i \cdot \bar{\mu}_j}{\left|\bar{T}_{ij}\right|^3} - \frac{3\left(\bar{\mu}_i \cdot \bar{T}_{ij}\right)\left(\bar{\mu}_j \cdot \bar{T}_{ij}\right)}{\left|\bar{T}_{ij}\right|^5} \right\rangle \tag{13}$$

where ε_d represents the dielectric constant.

$\bar{T}_{ij}$ [Å] is the distance vector between the electric dipole transition moment vectors $\bar{\mu}_i$ [Debye] and $\bar{\mu}_j$ [Debye],

$$\bar{T}_{ij} = X_j - X_i \tag{14}$$

and X_i [Å] is the coordinate of the midpoint of oscillator i, with dipole transition moment $\bar{\mu}_i$ [Debye].

The CD intensities can be obtained from the rotational strengths R [$Debye^2$], defined by:

$$R_k = -\left(\pi/c\right)\sum_{i=1}^{N}\sum_{j>i}^{N} c_{ik}c_{jk}\left[\left(\nu_j X_j - \nu_i X_i\right)\cdot \bar{\mu}_i \times \bar{\mu}_j\right] \tag{15}$$

where c [Å s^{-1}] is the velocity of light. The position vectors, X [Å], of the dipoles are weighted by the frequency, ν [s^{-1}], of the particular oscillation.

5.2.2 NECO Computational Details

The standard B-DNA helical geometry of the selected deoxyoctanucleotides was adopted as the best approximation to the true molecular geometry since geometry refinement using empirical force fields led to severe structural changes and IR/VCD spectra calculated from these large systems bore little resemblance to the experimental spectra. The parameters for a standard B-DNA helix (*Insight II* 95.0, 1995) include a rise of 3.4 Å and an unwinding angle of -36°, assigned with this convention for technical reasons (*Insight II* 95.0, 1995). Vibrational transitions were assigned on the basis of *ab initio*

harmonic wavenumbers and intensities, while electronic transitions were assigned on the basis of *ab initio* excitation energies.

IR and VCD spectra of the deoxyoctanucleotides and their daunorubicin complexes were simulated using the electric transition dipole moments corresponding to the three most intense IR absorptions of the dimethyl phosphate anion and the first seven consecutive wavenumbers of the nucleotide base-pairs in Table 5, page 71 and Table 7, page 75, which invariably contained the most intense IR absorptions, of which the most intense is illustrated in Figure 28. The UV and ECD spectra of the deoxyoctanucleotides, on the other hand, were simulated using the electric transition dipole moments corresponding to the most intense UV absorption(s) of the nucleotide bases (illustrated in Figure 29). In total, three electric transition dipole moments were chosen for dimethyl phosphate, seven for each of the C-G and A-T base-pairs (see Table 11, page 107) , one for C, T and A, and two for G (see Table 10, page 92). Coordinates of these electric transition dipole moments were transformed to the standard B-helical deoxyoctanucleotide orientation, illustrated for d(CGAATTCG).d(CGAATTCG) in Figure 23, page 67.

For the deoxyoctanucleotide-daunorubicin complexes, the standard B-DNA structures of the deoxyoctanucleotides were adjusted to incorporate the intercalated daunorubicin molecules. As a starting point, the parameters of the X-ray crystal structure of d(CGTACG).d(CGTACG)-2(daunorubicin) (Wang *et al.*, 1987), discussed in Chapter 3, were employed. The terminal two base-pairs on either end of the helix constitute the intercalation sites. At these sites the distance between the two terminal base-pairs from the adjacent base-pair was fixed at 6.8 Å and the unwinding angle of -36° was unchanged from the standard B-DNA geometry, whereas the base-pairs adjacent to the intercalation sites were unwound by 8° per daunorubicin (Wang *et al.*, 1987). Accordingly, the unwinding angle of one base-pair adjacent to the intercalation site had to increase or

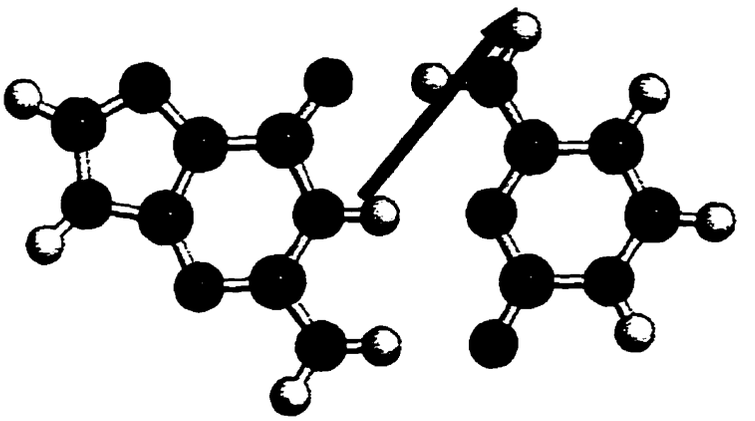

Cytosine-Guanine base-pair (C-G)

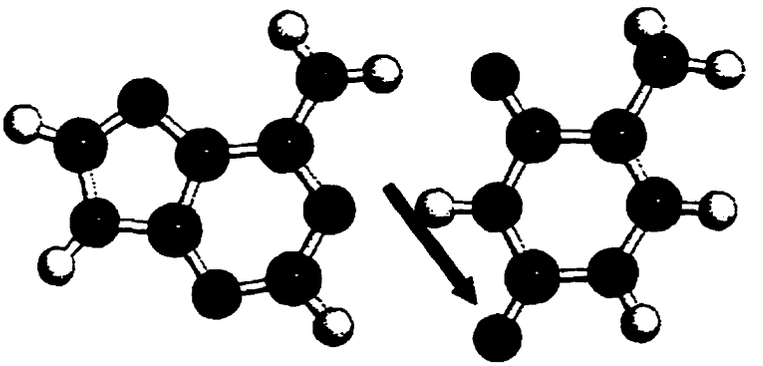

Adenine-Thymine base-pair (A-T)

Figure 28
Nucleotide Base-Pairs with Electric Transition Dipole Moments

Arrows represent the most intense electric transition moments which occur at 1671 cm^{-1} for C-G and 1719 cm^{-1} for A-T.

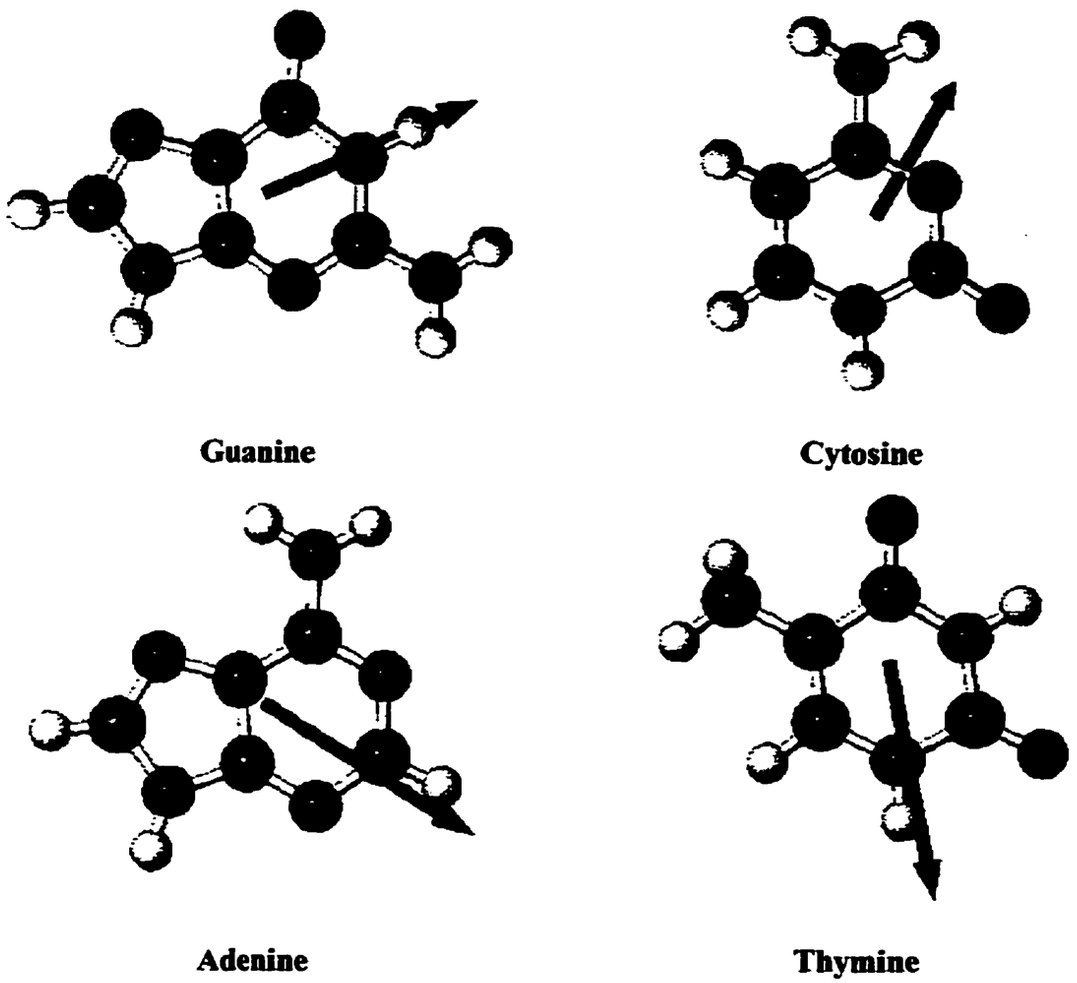

Figure 29
Nucleotide Bases with Electric Transition Dipole Moments

Arrows represent the most intense electric transition moments which occur at 40650 cm^{-1} for G; 37453 cm^{-1} for C; 38388 cm^{-1} for A and 37807 cm^{-1} for T.

decrease by 8° to give unwinding angles of -44° and -28°, respectively. On the other hand, the unwinding angles of two base-pairs adjacent to the intercalation site had to increase or decrease by 4° each, resulting in unwinding angles of -40° and -32°. The deoxyoctanucleotide-daunorubicin complex VCD spectra were simulated with the above mentioned unwinding angles. Those with unwinding angles less than -44° produced negative VCD features at higher wavenumbers than those evident in the experimental VCD spectra. Hence, an unwinding angle of -44° for the base-pair adjacent to the intercalation site reproduced the experimental spectra most satisfactorily. Even though -44° represents a winding of the helix which is contrary to the intercalation process, it should be emphasized that a concomitant shortening of the helix with winding is eliminated in these calculations by virtue of the distances between the base-pairs being fixed at 3.4 Å and 6.8 Å for the terminal base-pairs at the intercalation site. Therefore, the effect of rotating the base-pair(s) adjacent to the intercalation site is being modeled and not the associated lengthening of the helix with unwinding.

The model was tested further for various other attributes reported in the X-ray crystal structures of deoxyhexanucleotide-daunorubicin complexes (Frederick *et al.*, 1990; Wang *et al.*, 1987). These attributes include buckling, tilting and unwinding of the terminal base-pairs at the intercalation site. The effects of base-pair unwinding, buckling and tilting were tested by varying the terminal base-pairs unwinding, incline and tilt angles, respectively, in the ranges of -28 to -70° for unwinding and 0 to 20° for both buckling and tilting. These changes appeared to have no effect on the calculated VCD spectra of the deoxyoctanucleotide-daunorubicin complexes. Perhaps the large separation of the terminal base-pairs at the intercalation sites diminished the coupled oscillator interaction to a large extent.

Daunorubicin was examined for electric transition dipole moments that could appreciably contribute to the absorption and VCD spectra of the deoxyoctanucleotide-daunorubicin complexes. The band at 1706 cm^{-1} apparent in the daunorubicin absorption spectrum (illustrated in Figure 15, page 51) appears not to be coupling with the deoxyoctanucleotides since the deoxyoctanucleotide-daunorubicin complex spectra (see

Figure 16, page 55 to Figure 21, page 60) show no coupling-induced splitting at 1706 cm^{-1}, as indicated by the absence of bands at wavenumbers greater than 1706 cm^{-1}. The 1617 cm^{-1} band of daunorubicin can be assigned to the antisymmetric stretching vibrations of the carbonyl groups at $C_{(5)}$ and $C_{(12)}$ (see Figure 6, page 20) which are polarized in-plane perpendicular to the long axis of daunorubicin, while the bands at 1587 cm^{-1} and 1557 cm^{-1} may be attributed to resonance structures (Suarato, 1990). Daunorubicin exhibits a comparable extinction coefficient at 1617 cm^{-1} to that of the deoxyoctanucleotides on a per base-pair basis, hence suggesting that daunorubicin possesses a significant transition dipole moment at 1617 cm^{-1}. The magnitude of this transition dipole moment was realized by integrating the area under the 1617 cm^{-1} peak in the daunorubicin absorption spectrum. Incorporation of the daunorubicin transition dipole had no effect on the results of the calculated IR/VCD spectra of the deoxyoctanucleotide-daunorubicin complexes. Nonetheless, it was retained in the calculation.

For IR/VCD and UV/ECD spectral simulations, wavenumbers of the base-pairs were adjusted according to the experimental IR absorption spectra (see Table 11, page 107) of the selected deoxyoctanucleotides and previously reported experimental UV absorption spectra (see Table 9) of the nucleotide bases (Sorber, 1970), respectively. The partial resolution of the IR absorption spectra made it difficult to resolve wavenumber contributions from C-G and A-T base-pairs separately. For example, the appearance and the intensity of the IR absorption band at 1683 cm^{-1} in the deoxyoctanucleotides is maintained with A-T base-pair substitution (see Figure 36, page 101 to Figure 41, page 106). Therefore, the theoretical prediction of 1671 cm^{-1} for the C-G base-pair and 1719 cm^{-1} for the A-T base-pair (see Table 5, page 71 and Table 7, page 75) were both adjusted to 1683 cm^{-1} (see Table 11, page 107). The large shift of the 1719 cm^{-1} band to lower energy could probably be accounted for by the presence of a hydrogen-bonded carbonyl group in the A-T base-pair $C_{(17)}=O_{(20)}$ (see Figure 3, page 10) as a result of solvating the deoxyoctanucleotides. The simulated spectra assumed Lorentzian band shapes of 12 cm^{-1} half-width-at-half-height for IR/VCD and 2600 cm^{-1} for UV/ECD spectra.

5.2.3 Assumptions in the NECO Model

The following assumptions were made in the computations:

- The electric transition dipole moments are predicted accurately from *ab initio* calculations.
- The predominant interaction contributing to the ECD and VCD spectra are due to the coupled oscillator mechanism.
- The interactions between the helix backbone and the nucleotide vibrational modes are negligible.
- The nucleotide bases and base-pairs have a distance dependent dielectric of 4d, where d is the distance (Å) between chromophores, in contrast to the phosphate backbone which has the dielectric of bulk water because it is directly exposed to an aqueous environment.

5.2.4 Intrinsic Chirality of Base-Pairs

The VCD signals in the NECO computations originate from the interaction among base-pairs, rather than solely from intrinsic chirality. However, the base-pairs are never ideally planar in natural DNA sequences. The base-pairs show a propellor twist, caused by the bases rotating clockwise relative to their hydrogen bonded partner around the long axis, C8 of the purine and C6 of the pyrimidine, see Figure 3 on page 10. In many model crystalline oligonucleotides, a deviation from planarity was found in the range of 5° to 25°, with a slightly greater variance for A-T than for C-G base-pairs (Blackburn, 1990). MSI's molecular modeling system (*Insight II* 95.0, 1995) generates a B-DNA helix with a propellor twist of 3° to 5°.

5.2.5 Simulation of UV/ECD Spectra of Deoxyoctanucleotides

Three factors inspired the measurement of the UV/ECD spectra of the selected deoxyoctanucleotides:

a) to confirm the right-handed conformation of the deoxyoctanucleotides

b) to illustrate that VCD spectra give more detail than ECD spectra

c) to validate the NECO model implementation

The UV absorption and ECD spectra of the selected deoxyoctanucleotides were measured in the 31250-50000 cm^{-1} range. Particularly prominent ECD features occur between 33300-42500 cm^{-1}, which are ascribed to the $\pi \rightarrow \pi^*$ electronic transitions of the nucleotide bases (Bush, 1974). The bisignate couplets present in the experimental ECD spectra, suggest the effect of a coupled oscillator mechanism rather than intrinsic chirality. In order to aid interpretation of the experimental UV/ECD spectra, previously reported experimental UV wavenumbers and extinction coefficients of the nucleotide bases at pH 7.0 are listed in Table 9 (Sorber, 1970).

Table 9
Experimental UV wavenumbers and Extinction Coefficients of Nucleotide Bases at pH 7.0

Nucleotide Bases	λ_{max} (nm)	‡ $\bar{\nu}_{max}$ (cm^{-1})	‡ ε_{max} (x 10^{-3}) (M^{-1} cm^{-1})
Cytosine	267	37453	6.1
Thymine	264.5	37807	7.9
Guanine	246	40650	10.7
Guanine	276	36232	8.15
Adenine	260.5	38388	13.4

‡ Experimental UV absorption wavenumbers and extinction coefficients of nucleotide bases at pH 7.0 (Sorber, 1970).

The electric transition dipole moments of the nucleotide bases calculated with the CIS approach and the 6-31+G* basis set are listed in Table 10 and employed for simulating UV/ECD spectra of the deoxyoctanucleotides. The perturbation of the magnitude and orientation of an oscillator by the complementary base, included as point charges, in the base-pair was found to be negligible. The dipole contributions of the nucleotide bases differ in calculation (oscillator strengths) and experiment (extinction coefficients), with

adenine and thymine having the strongest experimental and calculated dipole contributions, respectively. This difference is probably due to some combination of error in the predicted orientation and separation of the oscillators.

Table 10
Electric Transition Dipole Moments Employed for UV/ECD Simulations

Nucleotide Bases	$\bar{\nu}$ (cm^{-1}) [a]	x [b]	y [b]	z [b]	f(Au) [d]
cytosine [c]	37453	0.577	0.920	0.000	0.1749
thymine [c]	37807	0.312	-1.674	0.000	0.4482
guanine [c]	40650	-1.396	-0.735	0.000	0.3959
guanine	36232	-0.349	1.344	0.000	0.2859
adenine [c]	38388	-1.658	0.249	0.000	0.4279

[a] Experimental UV wavenumbers of nucleotide bases at pH 7.0 (Sorber, 1970).

[b] Coordinates of the calculated electric transition moments , with reference to standard orientation (see Appendix 1), used to simulate UV/ECD spectra.

[c] Electric transition dipole moments illustrated in Figure 29, page 87.

[d] Calculated oscillator strengths (in atomic units) of nucleotide bases.

All the deoxyoctanucleotides display a bisignate ECD couplet with the negative ECD band at higher wavenumber and the positive ECD band at lower wavenumber (see Figure 30, page 94 to Figure 35, page 99) characterizing a right-handed conformation. The experimental negative ECD features are more intense than the positive ECD features. The NECO model reproduces the overall features of the UV/ECD spectra.

UV and ECD bands are inherently broad with overlapping bands thus causing details to be less evident in comparison to IR/VCD (see Figure 36, page 101 to Figure 41, page 106). For example switching the order of nucleotide bases in the deoxyoctanucleotide sequences cause subtle wavenumber shifts in the UV/ECD spectra. Nonetheless, the extent to which bases contribute most to various regions of the UV/ECD spectra can be derived by taking into account the magnitudes (extinction coefficients) and positions of the transition dipole moments which in turn provide information regarding

their interaction. The thrust of this research, however, is the study of IR/VCD spectra and as such a detailed analysis of the UV/ECD spectra is beyond the scope of this work.

5.2.6 Simulation of IR/VCD Spectra of Deoxyoctanucleotides

The NECO model reproduces the overall features of the IR/VCD spectra (see Figure 36, page 101 to Figure 41, page 106). However, as the bisignate couplet diminishes in the 1700-1600 cm^{-1} region of the experimental VCD spectra upon increasing substitution of the principal deoxyoctanucleotide, the NECO model simulates these spectra with less success. This is not surprising in view of the assumption that the coupled oscillator mechanism is the predominant interaction in the NECO model, which is not exclusively so according to the experimental results.

The simulated VCD spectra of the various deoxyoctanucleotides exhibit similar wavenumbers but vastly varying intensities, which constitute the distinguishing features among the selected deoxyoctanucleotides. The correlation between experimental and calculated IR/VCD features and their assignments (see Table 12, page 108 to Table 17, page 113) are tentative and based on the correspondence of experimental wavenumbers. For example, in Table 12 on page 108 the experimental IR absorption band at 1683 cm^{-1} corresponding to the observed VCD couplet at 1692(-)/1679(+) cm^{-1} is assigned to the simulated IR absorption band at 1686 cm^{-1} affiliated with the VCD couplet at 1697(-)/1686(+) cm^{-1}, in an attempt to match wavenumbers. However, if one were to match intensities then the corresponding simulated VCD couplet should be assigned to 1676(-)/1651(+). The fact that the experimental VCD couplet, 1692(-)/1679(+) cm^{-1}, is not centered at 1683 cm^{-1} suggests that contributions other than those exclusively attributed to the coupled oscillator mechanism are involved, or perhaps intrinsic chirality is responsible considering that all the selected deoxyoctanucleotide sequences are chiral.

An interesting observation in the case of d(CGCGCGCG).d(CGCGCGCG) for example (see Figure 36, page 101) is that the most intense simulated IR absorption band at 1686 cm^{-1} results in a weak VCD couplet at 1697(-)/1686(+) cm^{-1}. The largest oscillator

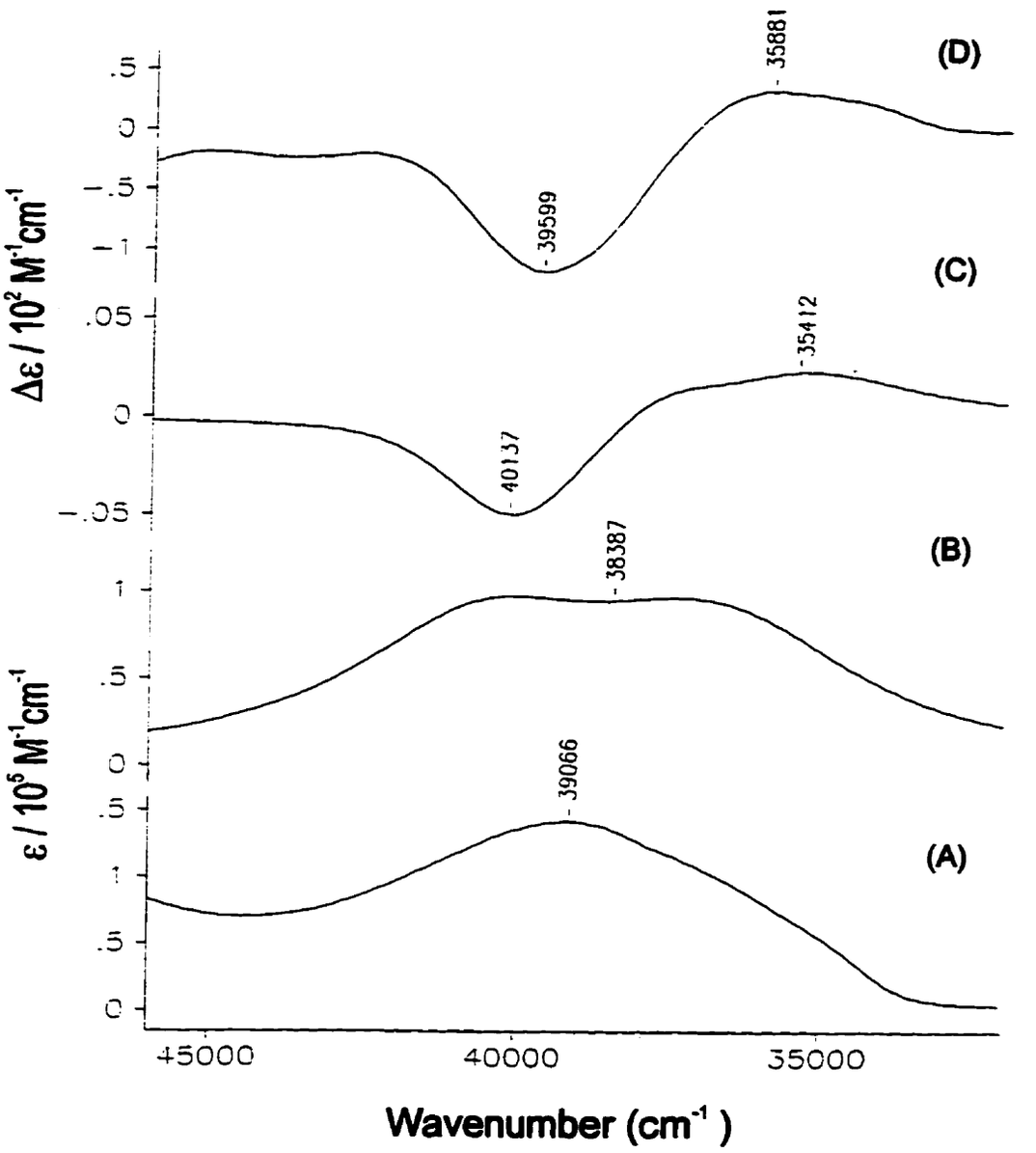

Figure 30
Experimental and Calculated UV Absorption and ECD Spectra of d(CGCGCGCG).d(CGCGCGCG)

Experimental UV absorption (A), calculated UV absorption (B), calculated ECD (C) and experimental ECD (D) spectra.

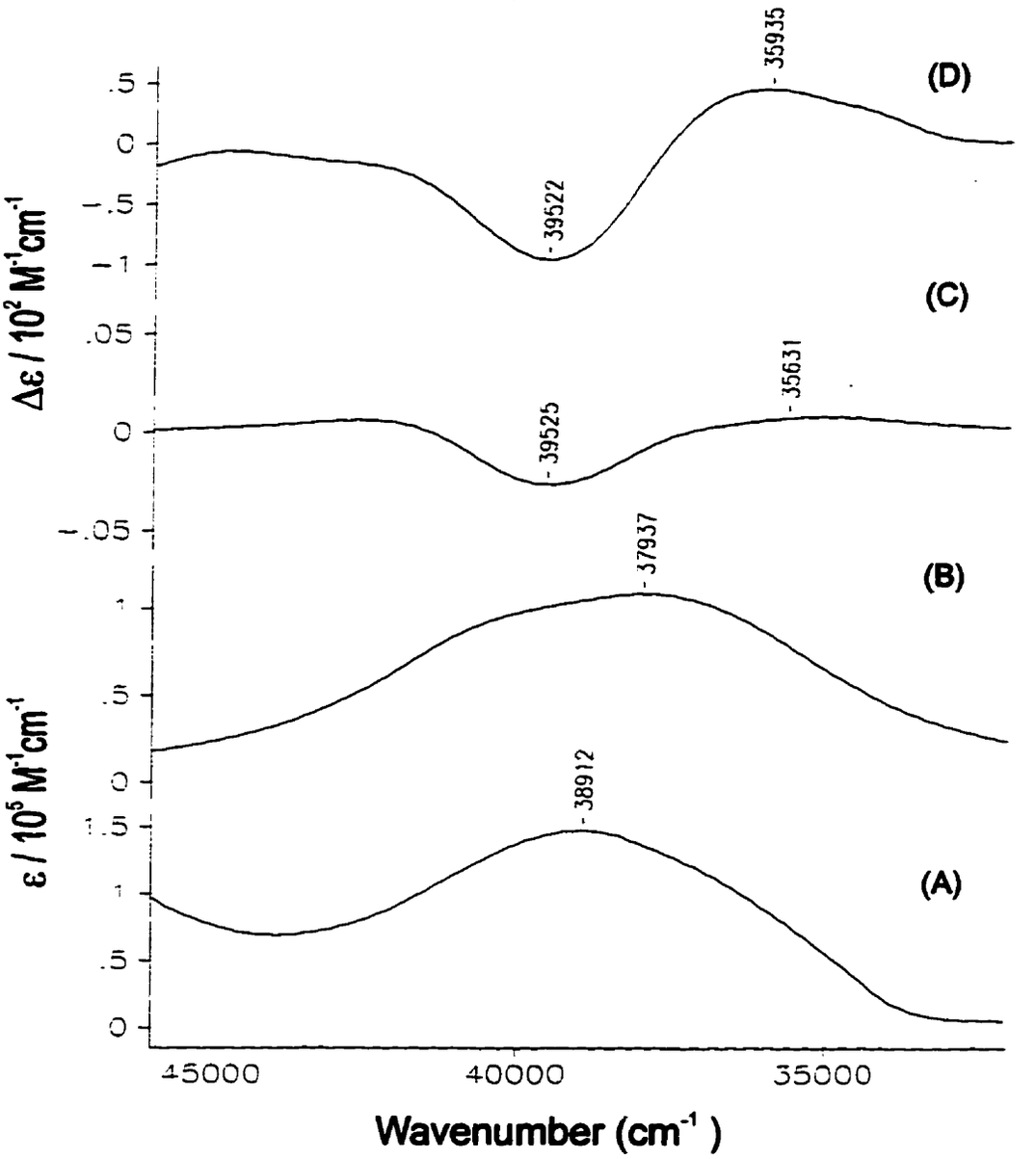

Figure 31
Experimental and Calculated UV Absorption and ECD Spectra of d(CGCATGCG).d(CGCATGCG)

Experimental UV absorption (A), calculated UV absorption (B), calculated ECD (C) and experimental ECD (D) spectra.

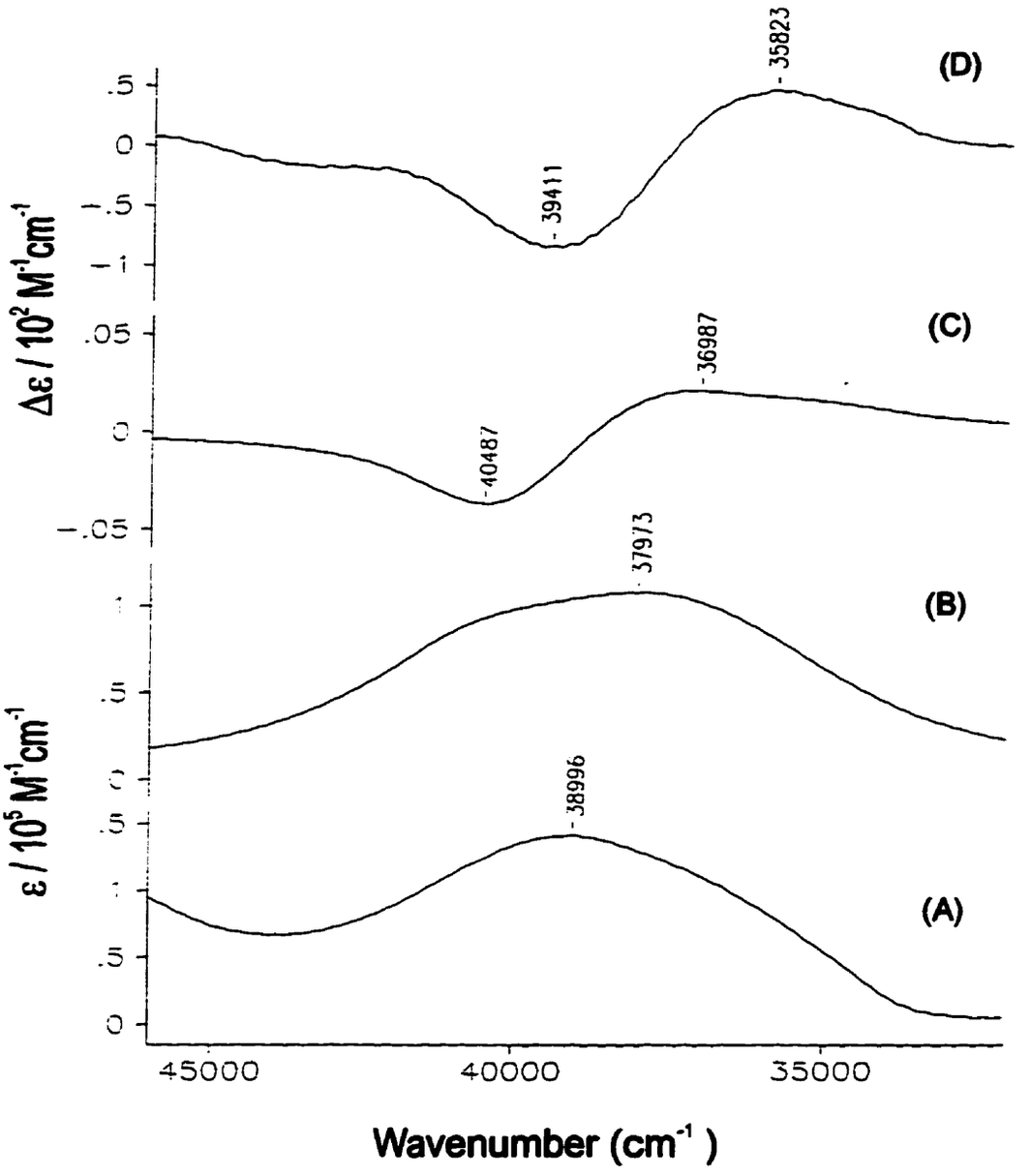

Figure 32
Experimental and Calculated UV Absorption and ECD Spectra of d(CGCTAGCG).d(CGCTAGCG)

Experimental UV absorption (A), calculated UV absorption (B), calculated ECD (C) and experimental ECD (D) spectra.

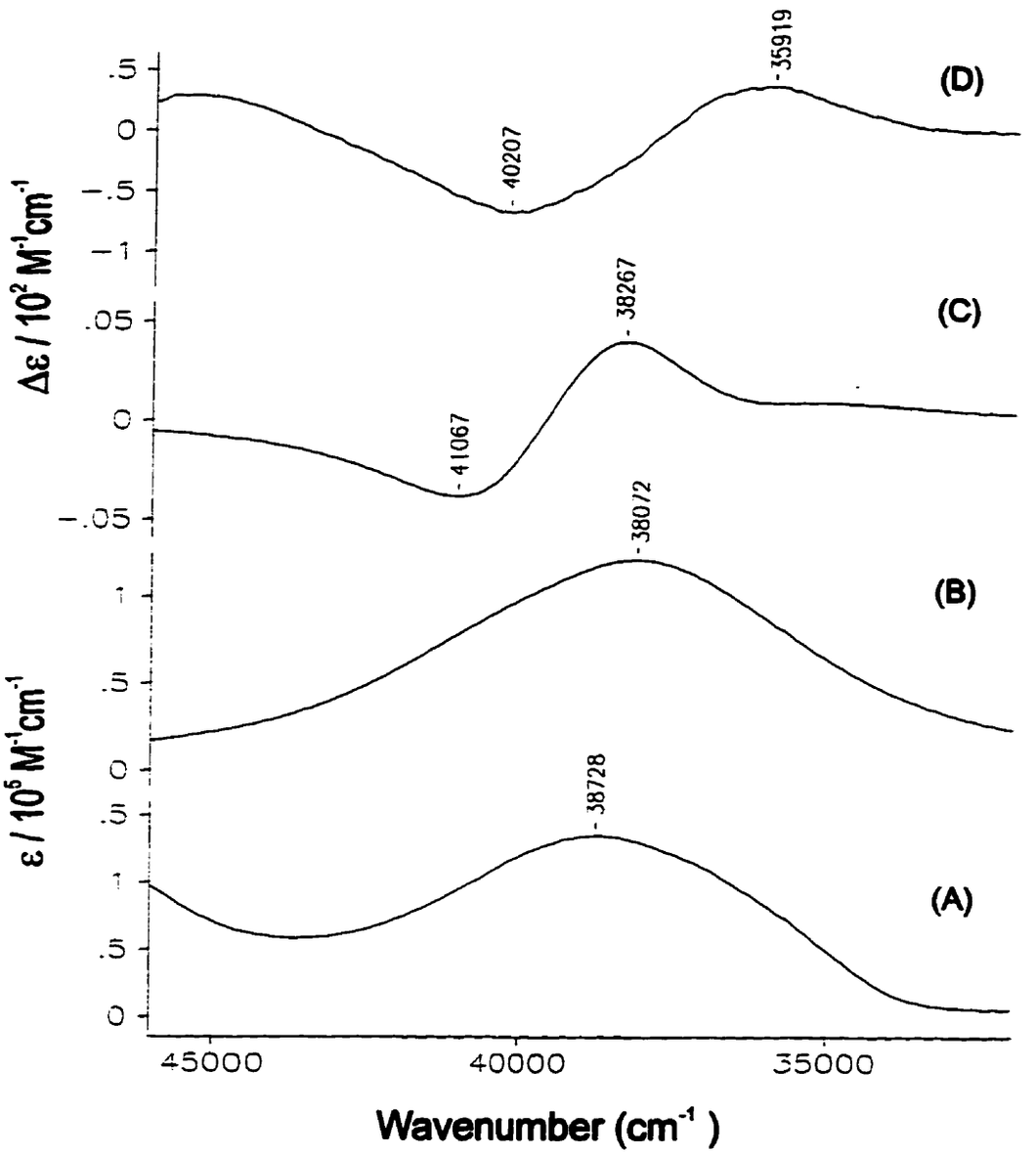

Figure 33
Experimental and Calculated UV Absorption and ECD Spectra of d(CGATATCG).d(CGATATCG)

Experimental UV absorption (A), calculated UV absorption (B), calculated ECD (C) and experimental ECD (D) spectra.

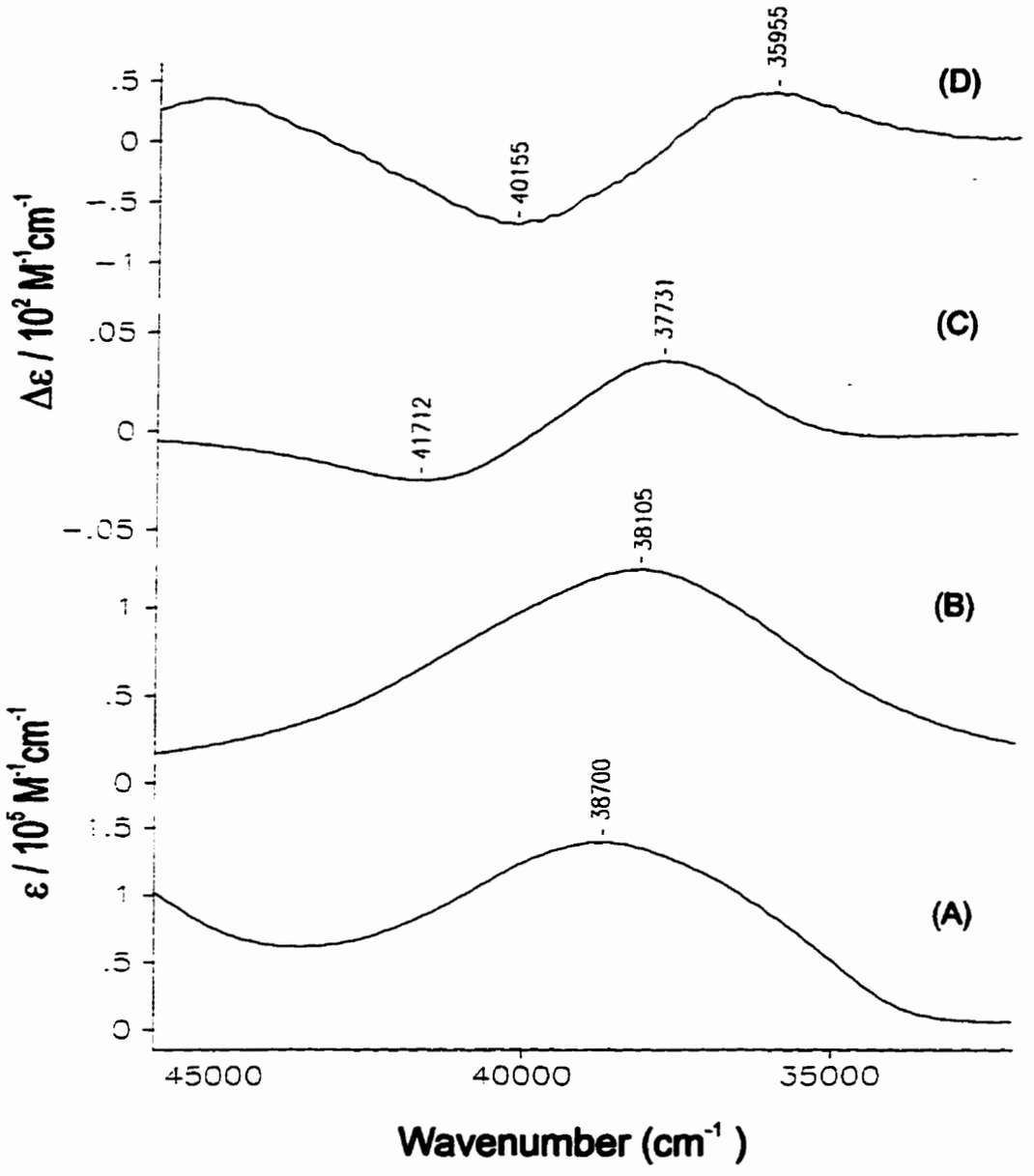

Figure 34
Experimental and Calculated UV Absorption and ECD Spectra of d(CGTATACG).d(CGTATACG)

Experimental UV absorption (A), calculated UV absorption (B), calculated ECD (C) and experimental ECD (D) spectra.

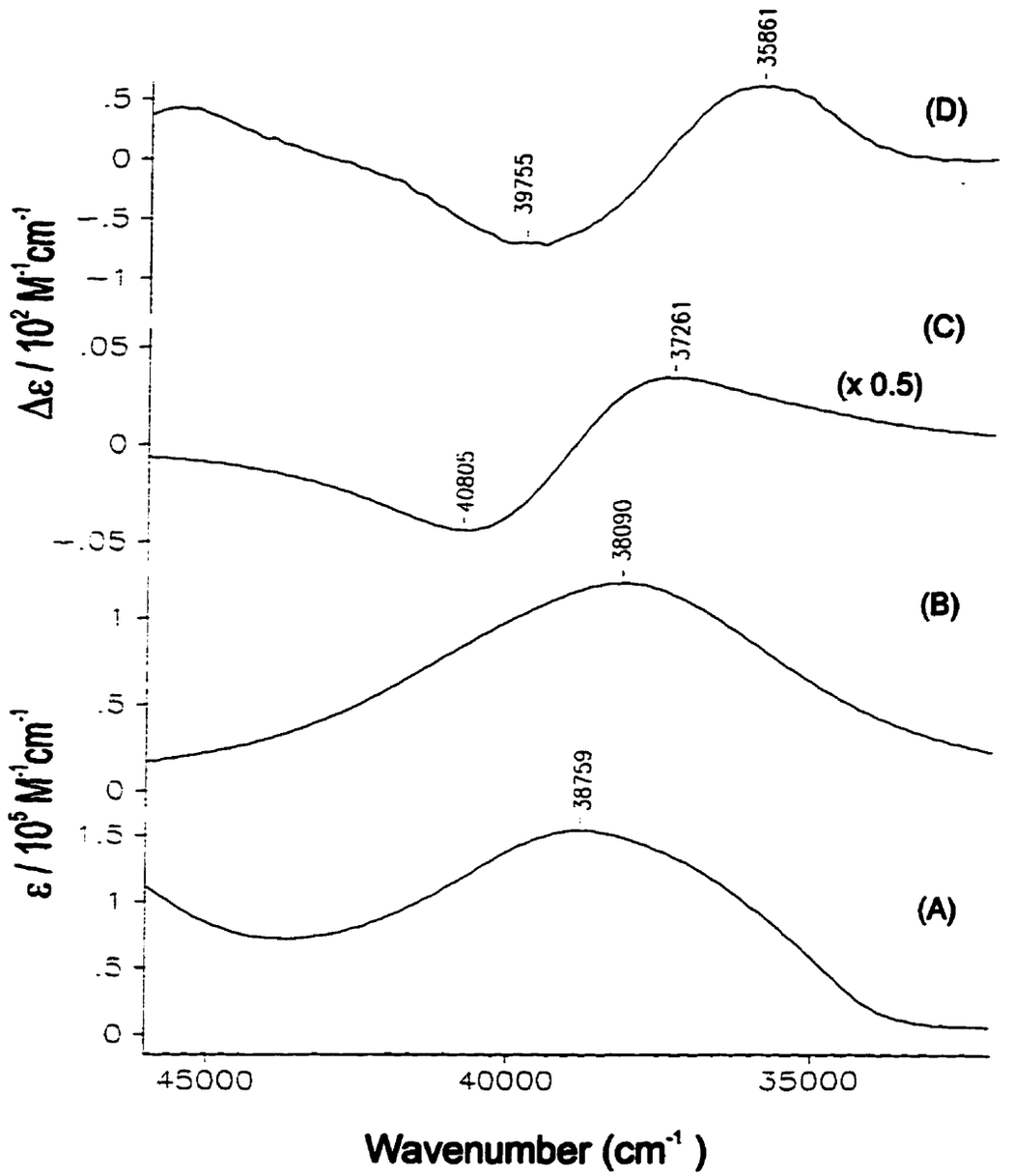

Figure 35
Experimental and Calculated UV Absorption and ECD Spectra of d(CGAATTCG).d(CGAATTCG)

Experimental UV absorption (A), calculated UV absorption (B), calculated ECD (C) and experimental ECD (D) spectra.

in the C-G base-pair (see Table 11, page 107) at 1683 cm^{-1} with a calculated intensity of 1310 km mol^{-1} is theoretically expected to give rise to the strongest VCD couplet, since the average angle (pitch) and distance (rise) between all the base-pairs of the deoxyoctanucleotides in standard B-DNA conformation are fixed at 3.4 Å and -36°, respectively (*Insight II* 95.0, 1995). The contradiction to this prediction in the simulated spectra indicates that the primary oscillator is not coupling with itself on adjacent base-pairs but coupling with a minor oscillator where the cross moments are closer to 90°. The tendency of the most intense simulated IR absorption band corresponding to a weak VCD couplet is evident in all the simulated deoxyoctanucleotide spectra (see Figure 36, page 101 to Figure 41, page 106).

Minor oscillators with relatively weak calculated intensities, in the region of 1600-1400 cm^{-1}, were included in the NECO model to investigate whether the smaller experimental VCD couplets did reveal themselves in the simulated spectra but as anticipated they did not. The 1635(+)/1620(-) cm^{-1} and 1090(-)/1072(+) cm^{-1} couplets in the simulated VCD spectra are consistent for all the selected deoxyoctanucleotides and the latter is attributed to the symmetric stretching vibration of the PO_2^- in the sugar-phosphate backbone of the deoxyoctanucleotides.

The wavenumbers calculated by the B3-LYP procedure for the base-pairs, were uniformly scaled by 0.95 and as such were in the correct order, so that the most intense calculated wavenumbers could be adjusted to the most intense experimental wavenumbers. However, the correct assignment of gas phase calculations to partially resolved IR absorption spectra is extremely difficult. This is evident in the imperfect correlation between the experimental and calculated IR absorption spectra of all the deoxyoctanucleotides. There is also a danger in varying several parameters in order to match simulated spectra with experimental since this can result in the loss of the *ab initio* information.

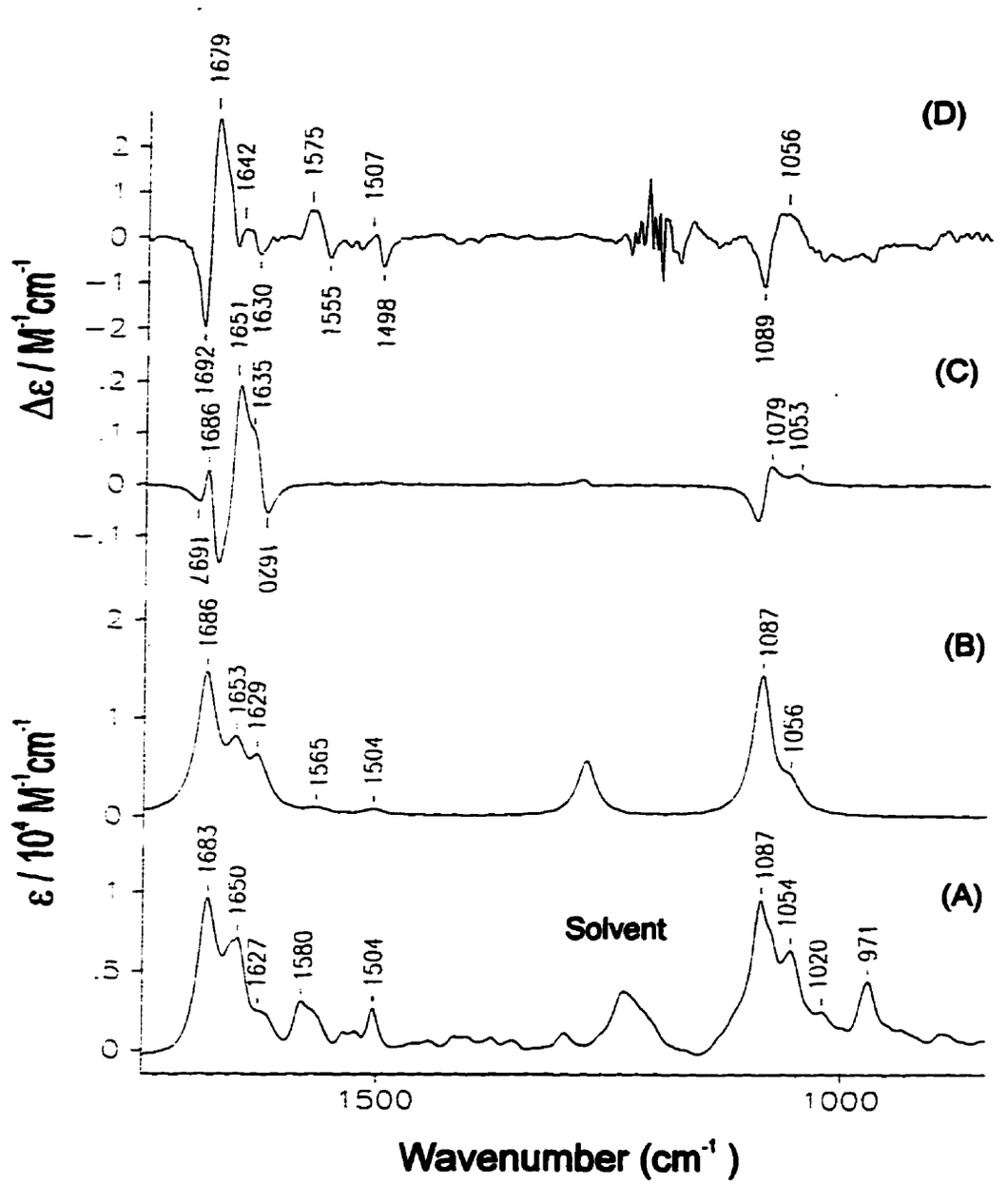

Figure 36
Experimental and Calculated IR Absorption and VCD Spectra of d(CGCGCGCG).d(CGCGCGCG)

Experimental IR absorption (A), calculated IR absorption (B), calculated VCD (C) and experimental VCD (D) spectra.

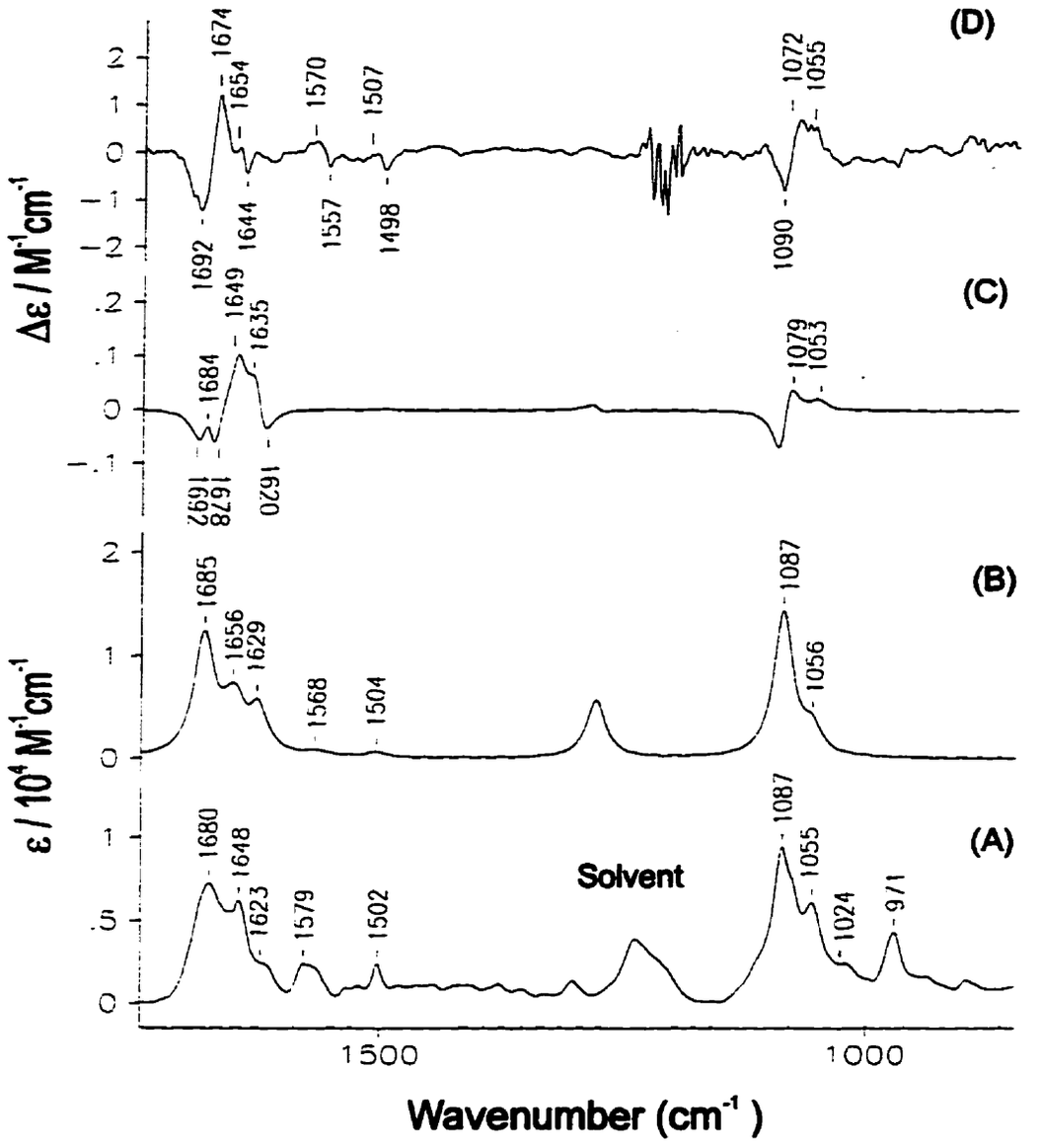

Figure 37
Experimental and Calculated IR Absorption and VCD Spectra of d(CGCATGCG).d(CGCATGCG)

Experimental IR absorption (A), calculated IR absorption (B), calculated VCD (C) and experimental VCD (D) spectra.

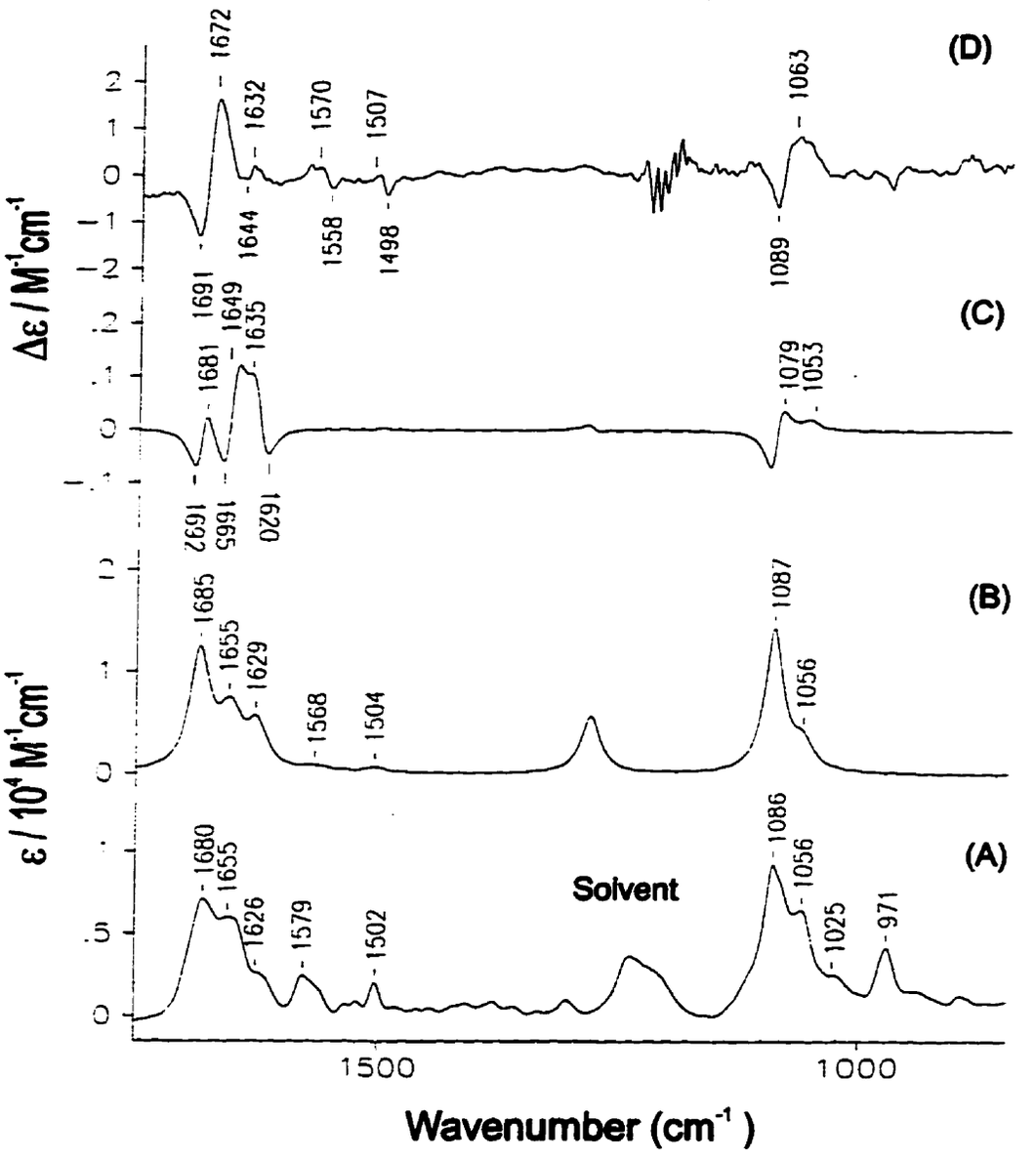

Figure 38
Experimental and Calculated IR Absorption and VCD Spectra of d(CGCTAGCG).d(CGCTAGCG)

Experimental IR absorption (A), calculated IR absorption (B), calculated VCD (C) and experimental VCD (D) spectra.

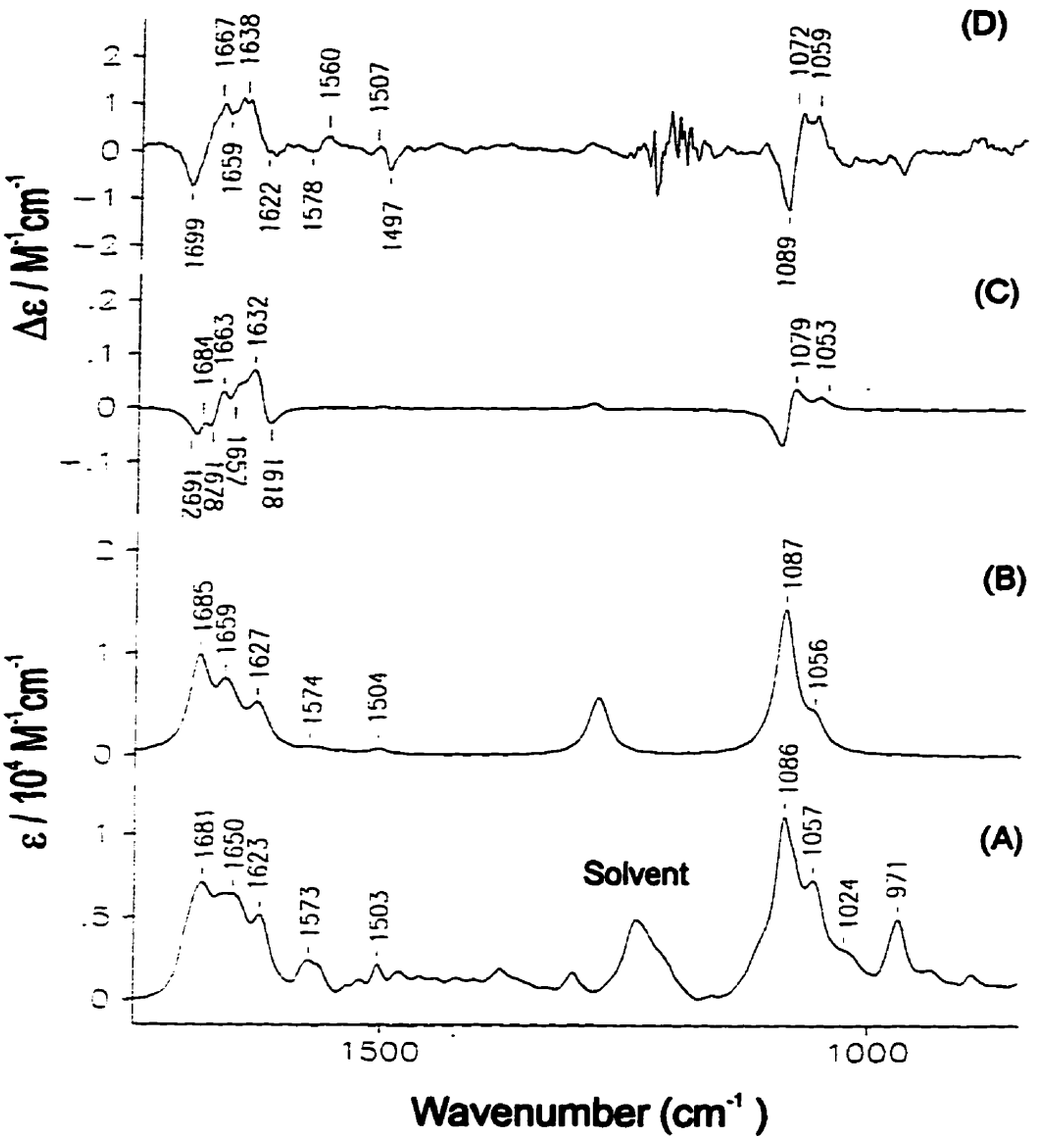

Figure 39
Experimental and Calculated IR Absorption and VCD Spectra of d(CGATATCG).d(CGATATCG)

Experimental IR absorption (A), calculated IR absorption (B), calculated VCD (C) and experimental VCD (D) spectra.

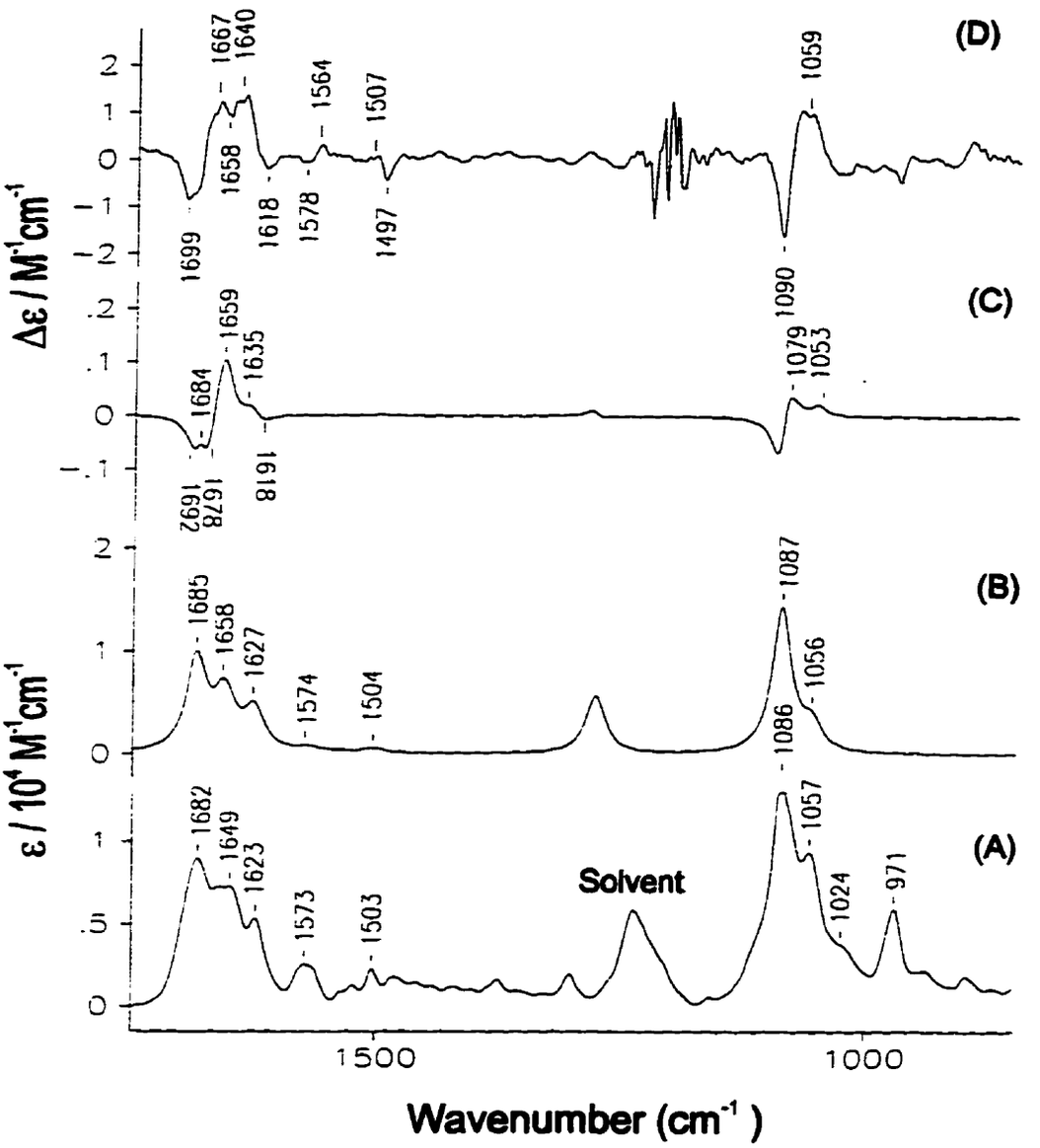

Figure 40
Experimental and Calculated IR Absorption and VCD Spectra of d(CGTATACG).d(CGTATACG)

Experimental IR absorption (A), calculated IR absorption (B), calculated VCD (C) and experimental VCD (D) spectra.

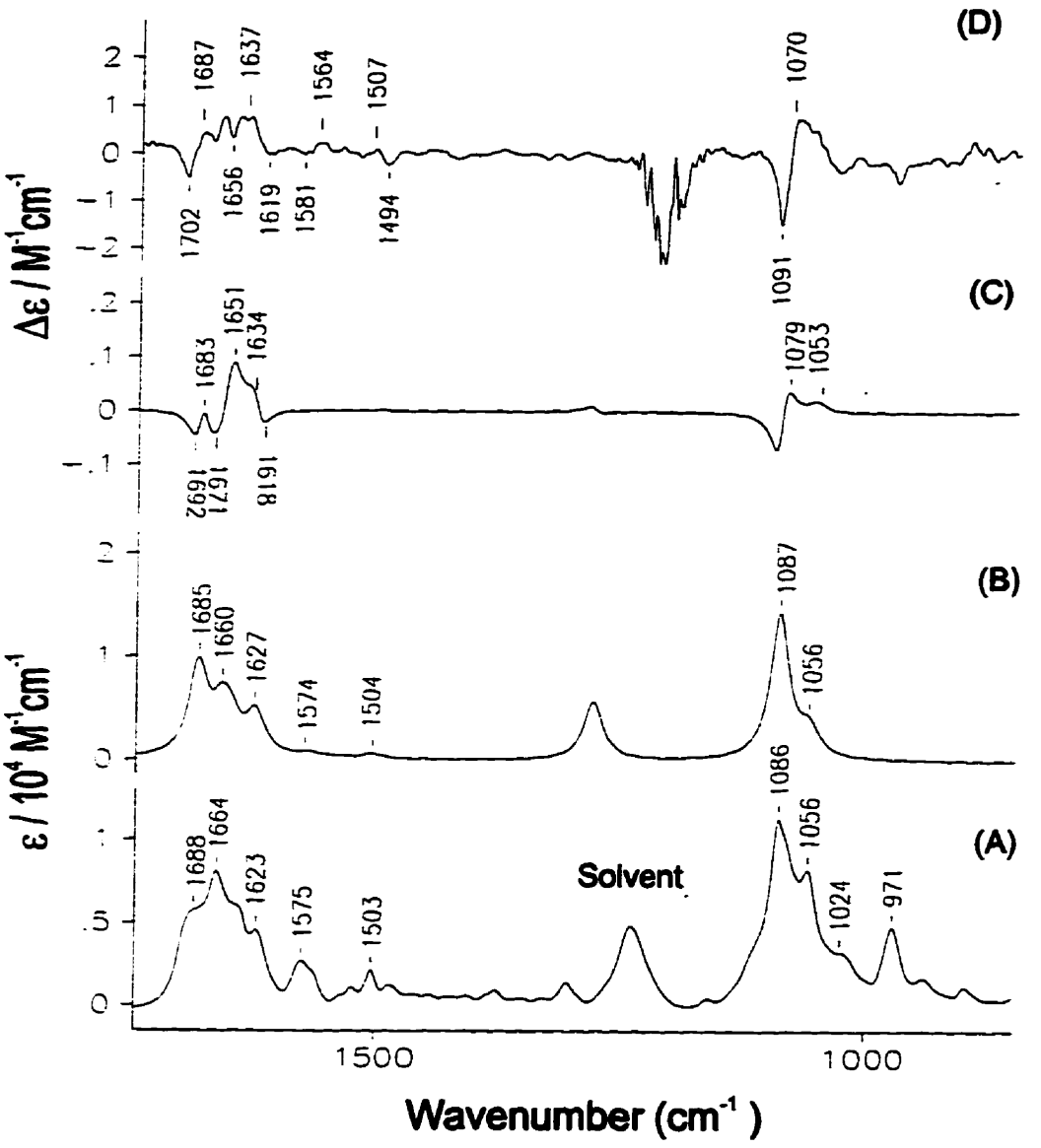

Figure 41
Experimental and Calculated IR Absorption and VCD Spectra of d(CGAATTCG).d(CGAATTCG)

Experimental IR absorption (A), calculated IR absorption (B), calculated VCD (C) and experimental VCD (D) spectra.

Table 11
Electric Transition Dipole Moments Used for IR/VCD Simulations

Assignments [a]	$\bar{\nu}$ (cm^{-1}) [b]	$\bar{\nu}$ (cm^{-1}) [c]	x [d]	y [d]	z [d]	A (km mol^{-1}) [f]
		cytosine-guanine				
Q11(cg) [e]	1671	1683	36.184	0.574	0.000	1310
Q13(cg)	1652	1659	7.674	10.957	0.000	179
Q14(cg)	1612	1650	1.343	-23.632	0.000	560
Q15(cg)	1541	1627	-11.854	21.073	0.000	585
Q16(cg)	1528	1580	-0.594	1.536	0.000	3
Q17(cg)	1493	1564	-5.647	4.902	0.000	56
Q18(cg)	1489	1504	7.826	-2.140	0.000	65
		adenine-thymine				
Q12(at)	1719	1683	21.816	0.211	0.000	476
Q13(at) [e]	1643	1659	-16.044	18.382	0.000	595
Q14(at)	1618	1650	4.701	-1.368	0.000	24
Q15(at)	1581	1623	17.150	10.802	0.000	423
Q16(at)	1544	1574	-1.095	7.863	0.000	63
Q17(at)	1479	1540	4.652	-3.224	0.000	32
Q19(at)	1447	1503	6.227	-2.886	0.000	47
		dimethyl phosphate anion				
Q13(dmp)	1255	1280	-8.832	-1.475	12.515	237
Q19(dmp)	1044	1086	-12.256	11.653	2.644	293
Q20(dmp)	1038	1056	6.660	13.700	-2.184	237

[a] Vibrational assignments see Table 5, page 71; Table 7, page 75 and Table 8, page 76.

[b] Wavenumbers calculated by the B3-LYP/6-31G** procedure and scaled by 0.95.

[c] Wavenumbers scaled according to experimental FTIR absorption spectra and implemented in the NECO model.

[d] Coordinates of the calculated electric transition dipole moments, with reference to standard orientation (see Appendix 1), used to simulate IR/VCD spectra.

[e] Electric transition dipole moments illustrated in the Figure 28, page 86.

[f] Calculated intensities listed in Table 5, page 71; Table 7, page 75 and Table 8, page 76..

Table 12
Calculated and Experimental wavenumbers of IR Absorption and VCD of d(CGCGCGCG).d(CGCGCGCG)

† Tentative Assignments	‡ $IR_{experimental}$ (cm^{-1})	‡ $IR_{calculated}$ (cm^{-1})	‡ $VCD_{calculated}$ (cm^{-1})	‡ $VCD_{experimental}$ (cm^{-1})
Q11(cg)	1683	1686	1697(-) 1686(+)	1692(-) 1679(+)
Q12(cg)	1659	-	1676(-) 1651(+)	1667(+?) 1655(-)
Q13(cg)	1650	1653	-	-
Q14(cg)	1627	1629	1635(+) 1620(-)	1642(+) 1630(-)
Q15(cg)	1580	-	-	-
Q16(cg)	1564	1565	- -	1575(+) 1555(-)
Q17(cg)	1504	1504	-	1507(+) 1498(-)
Q19(dmp)	1087	1087	1095(-) 1079(+)	1089(-) 1072(+)
Q20(dmp)	1054	1056	1053(+)	1056(+)
Q30(d)?	1020	-	-	-
Q32(d)?	971	-	-	-

† Refer to Table 5, page 71; Table 8, page 76 and Table 11, page 107.

‡ See Figure 36, page 101.

Table 13
Calculated and Experimental wavenumbers of IR Absorption and VCD of d(CGCATGCG).d(CGCATGCG)

[†] Tentative Assignments	[‡] $IR_{experimental}$ (cm^{-1})	[‡] $IR_{calculated}$ (cm^{-1})	[‡] $VCD_{calculated}$ (cm^{-1})	[‡] $VCD_{experimental}$ (cm^{-1})
-	-	-	-	1699(-?)
Q11(cg), Q12(at)	1680	1685	1692(-) 1684(+)	1692(-) 1674(+)
Q12(cg), Q13(at), Q13(cg), Q14(at)	1648	1656	1678(-) 1649(+)	1654(+) 1644(-)
Q14(cg), Q15(at)	1623	1629	1635(+) 1620(-)	1634(+?) -
Q15(cg), Q16(at)?	1579	-	-	-
Q16(cg)	1564	1568	- -	1570(+) 1557(-)
Q17(cg), Q18(at)	1502	1504	- -	1507(+) 1498(-)
Q19(dmp)	1087	1087	1095(-) 1079(+)	1090(-) 1072(+)
Q20(dmp)	1055	1056	1053(+)	1055(+)
Q30(d)?	1027	-	-	-
Q32(d)?	971	-	-	-

[†] Refer to Table 5, page 71; Table 7, page 75; Table 8, page 76 and Table 11, page 107.

[‡] See Figure 37, page 102.

Table 14
Calculated and Experimental wavenumbers of IR Absorption and VCD of d(CGCTAGCG).d(CGCTAGCG)

† Tentative Assignments	‡ $IR_{experimental}$ (cm^{-1})	‡ $IR_{calculated}$ (cm^{-1})	‡ $VCD_{calculated}$ (cm^{-1})	‡ $VCD_{experimental}$ (cm^{-1})
Q11(cg), Q12(at)	1680	1685	1692(-) 1681(+)	1691(-) 1672(+)
Q12(cg), Q13(at)	1655	1655	1665(-) 1649(+)	1655(-?) -
Q13(cg), Q14(at)	1647	-	- -	1644(-?) 1636(+)
Q14(cg), Q15(at)	1626	1629	1635(+) 1620(-)	- -
Q15(cg), Q16(at)	1579	-	-	-
Q16(cg)	1564	1568	-	1570(+) 1558(-)
Q17(cg), Q18(at)	1502	1504	- -	1507(+) 1498(-)
Q19(dmp)	1086	1087	1095(-) 1079(+)	1089(-) 1074(+)
Q20(dmp)	1056	1056	1053(+)	1058(+)
Q30(d)?	1022	-	-	-
Q32(d)?	971	-	-	-

† Refer to Table 5, page 71; Table 7, page 75; Table 8, page 76 and Table 11, page 107.

‡ See Figure 38, page 103.

Table 15
Calculated and Experimental wavenumbers of IR Absorption and VCD of d(CGATATCG).d(CGATATCG)

† Tentative Assignments	‡ $IR_{experimental}$ (cm^{-1})	‡ $IR_{calculated}$ (cm^{-1})	‡ $VCD_{calculated}$ (cm^{-1})	‡ $VCD_{experimental}$ (cm^{-1})
Q11(cg), Q12(at)	1681	1685	1692(-) 1684(+)	1699(-) 1667(+)
Q12(cg), Q13(at)	1658	1659	1678(-) 1659(+)	- -
Q13(cg), Q14(at)	1650	-	1657(-) 1641(-?)	1659(-) 1647(+)
Q14(cg), Q15(at)	1623	1627	1632(+) 1618(-)	1638(+) 1622(-)
Q16(at)	1573	1574	- -	1578(-?) 1560(+)
Q16(cg)	1564	-	-	-
Q17(cg), Q18(at)	1503	1504	- -	1507(+) 1497(-)
Q19(dmp)	1086	1087	1095(-) 1079(+)	1089(-) 1072(+)
Q20(dmp)	1057	1056	1053(+)	1059(+)
Q30(d)?	1023	-	-	-
Q32(d)?	971	-	-	-

† Refer to Table 5, page 71; Table 7, page 75; Table 8, page 76 and Table 11, page 107.

‡ See Figure 39, page 104.

Table 16
Calculated and Experimental wavenumbers of IR Absorption and VCD of d(CGTATACG).d(CGTATACG)

† Tentative Assignments	‡ $IR_{experimental}$ (cm^{-1})	‡ $IR_{calculated}$ (cm^{-1})	‡ $VCD_{calculated}$ (cm^{-1})	‡ $VCD_{experimental}$ (cm^{-1})
Q11(cg), Q12(at)	1682	1685	1692(-) 1684(+)	1699(-) 1667(+)
Q12(cg), Q13(at)	1658	1658	1678(-) 1659(+)	- -
Q13(cg), Q14(at)	1649	-	- -	1658(-) 1647(+?)
Q14(cg), Q15(at)	1623	1627	1635(+) 1618(-)	1640(+) 1618(-)
Q16(at)	1573	1574	- -	1578(-?) 1564(+)
Q16(cg)	1564	-	-	-
Q17(cg), Q18(at)	1503	1504	- -	1507(+) 1497(-)
Q19(dmp)	1086	1087	1095(-) 1079(+)	1090(-) 1070(+)
Q20(dmp)	1057	1056	1053(+)	1059(+)
Q30(d)?	1024	-	-	-
Q32(d)?	971	-	-	-

† Refer to Table 5, page 71; Table 7, page 75; Table 8, page 76 and Table 11, page 107.

‡ See Figure 40, page 105.

Table 17
Calculated and Experimental wavenumbers of IR Absorption and VCD of d(CGAATTCG).d(CGAATTCG)

† Tentative Assignments	‡ $IR_{experimental}$ (cm^{-1})	‡ $IR_{calculated}$ (cm^{-1})	‡ $VCD_{calculated}$ (cm^{-1})	‡ $VCD_{experimental}$ (cm^{-1})
Q11(cg), Q12(at)	1688	1685	1692(-) 1683(+)	1702(-) 1687(+)
Q12(cg), Q13(at)	1664	1660	1671(-) 1651(+)	1674(-?) 1665(+)
Q13(cg), Q14(at)	1651	-	- -	1656(-?) 1647(+)
Q14(cg), Q15(at)	1623	1627	1634(+) 1618(-)	1637(+) 1619(-?)
Q16(at)	1575	1574	- -	1578(-) 1564(+)
Q16(cg)	1564	-	-	-
Q17(cg), Q18(at)	1503	1504	- -	1507(+) 1497(-)
Q19(dmp)	1086	1087	1095(-) 1079(+)	1091(-) 1070(+)
Q20(dmp)	1056	1056	1053(+)	1055(+)
Q30(d)?	1024	-	-	-
Q32(d)?	971	-	-	-

† Refer to Table 5, page 71; Table 7, page 75; Table 8, page 76 and Table 11, page 107.

‡ See Figure 41, page 106.

5.2.7 Simulation of IR/VCD Spectra of Deoxyoctanucleotide-Daunorubicin Complexes

As in the case of the free deoxyoctanucleotide, the NECO model reproduces the overall features of the IR/VCD spectra (see Figure 42, page 116 to Figure 47, page 121). Experimental VCD spectra of deoxyoctanucleotide-daunorubicin complexes with increased substitution of the principal sequence exhibit less intense bisignate couplets if any, thus suggesting the breakdown or reduction of the coupled oscillator mechanism in comparison to other contributions, as in the case of the free deoxyoctanucleotides.

The correlation between experimental and calculated IR/VCD features and their assignments (see Table 18, page 122 to Table 23, page 127) are tentative and based on the correspondence of wavenumbers. Visually, however, the simulated VCD couplet at 1678(-)/1651(+) cm^{-1} compares with the d(CGCGCGCG).d(CGCGCGCG)-2(daunorubicin) experimental couplet at 1692(-)/1679(+) cm^{-1} more convincingly than the couplet chosen on the basis of wavenumber matching. Nonetheless, the prominent VCD couplets with their corresponding IR absorption bands for both the experimental and simulated IR/VCD spectra of the deoxyoctanucleotide-daunorubicin complexes, and their tentative assignments are listed in Table 18, page 122 to Table 23, page 127. Similar to the free deoxyoctanucleotides, the most intense simulated IR absorption band does not correspond to a strong VCD couplet in all the deoxyoctanucleotide-daunorubicin spectra.

The more informative variations in the simulated IR/VCD spectra of the selected deoxyoctanucleotides (see Figure 36, page 101 to Figure 41, page 106) upon intercalation with daunorubicin (see Figure 42, page 116 to Figure 47, page 121) shall now be qualitatively discussed.

The simulated IR absorption band at 1686 cm^{-1} corresponding to the VCD couplet at 1697(-)/1686(+) cm^{-1} in the free d(CGCGCGCG).d(CGCGCGCG) is significantly diminished upon intercalation with daunorubicin. However, the associated shift of the most intense VCD couplet to lower energy is not reproduced by the NECO model. A consequence of intercalation in d(CGCATGCG).d(CGCATGCG) is the broadening of the negative VCD feature in the most intense couplet, which is reproduced by the NECO

model. Daunorubicin intercalation of d(CGATATCG).d(CGATATCG) experimentally results in the loss of the 1699(-)/1667(+) cm^{-1} VCD couplet. The simulated VCD spectra changes substantially and somewhat resembles the overall VCD features of the experimental spectrum (-)/(+)/(-)/(+)/(-) with exaggerated intensities. Intercalation with daunorubicin appears to have reduced the intensity of the VCD couplet at 1702(-)/1687(+) cm^{-1} and rearranged the intensity of the other VCD features in the experimental d(CGAATTCG).d(CGAATTCG) spectrum . The simulated VCD spectrum reproduces the experimental spectrum very satisfactorily. The simulated IR absorption band at 1086 cm^{-1} corresponding to the simulated VCD couplet at 1095(-)/1080(+) cm^{-1} remains virtually unchanged in all the intercalated deoxyoctanucleotides and retains their wavenumber and band shape upon intercalation with daunorubicin.

The NECO model simulated the deoxyoctanucleotide-daunorubicin complexes with greater success than the free deoxyoctanucleotides. This may be in part attributed to the end fraying effects experienced by the deoxyoctanucleotides in solution, which cause the pitch and rise of the terminal base-pairs to be different from the other base-pairs in a more protected environment. For the calculations, a constrained standard B-geometry was imposed on the deoxyoctanucleotides where the pitch and rise of all the base-pairs were treated equivalently. In the case of the deoxyoctanucleotide-daunorubicin complexes, the standard B-geometry of the deoxyoctanucleotides were modified to accommodate the drug, by increasing the rise of the terminal base-pairs and the pitch of the base-pair adjacent to the intercalation site. This scenario probably resembles that in solution more closely therefore the simulated spectra exhibit better correspondence with the experimental spectra of the deoxyoctanucleotide-daunorubicin complexes than the free deoxyoctanucleotides.

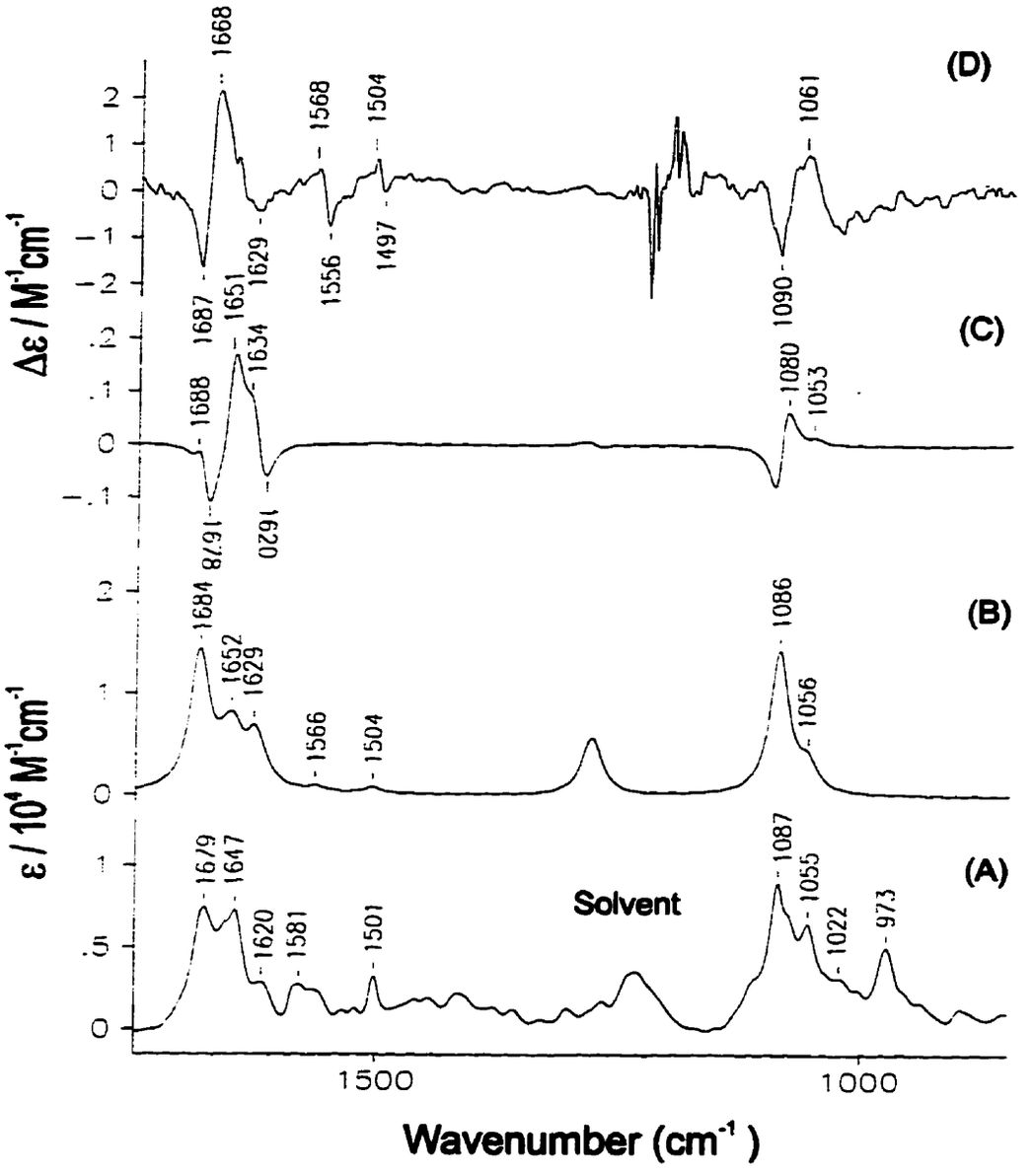

Figure 42
Experimental and Calculated IR Absorption and VCD Spectra of d(CGCGCGCG).d(CGCGCGCG)-2(Daunorubicin)

Experimental IR absorption (A), calculated IR absorption (B), calculated VCD (C) and experimental VCD (D) spectra.

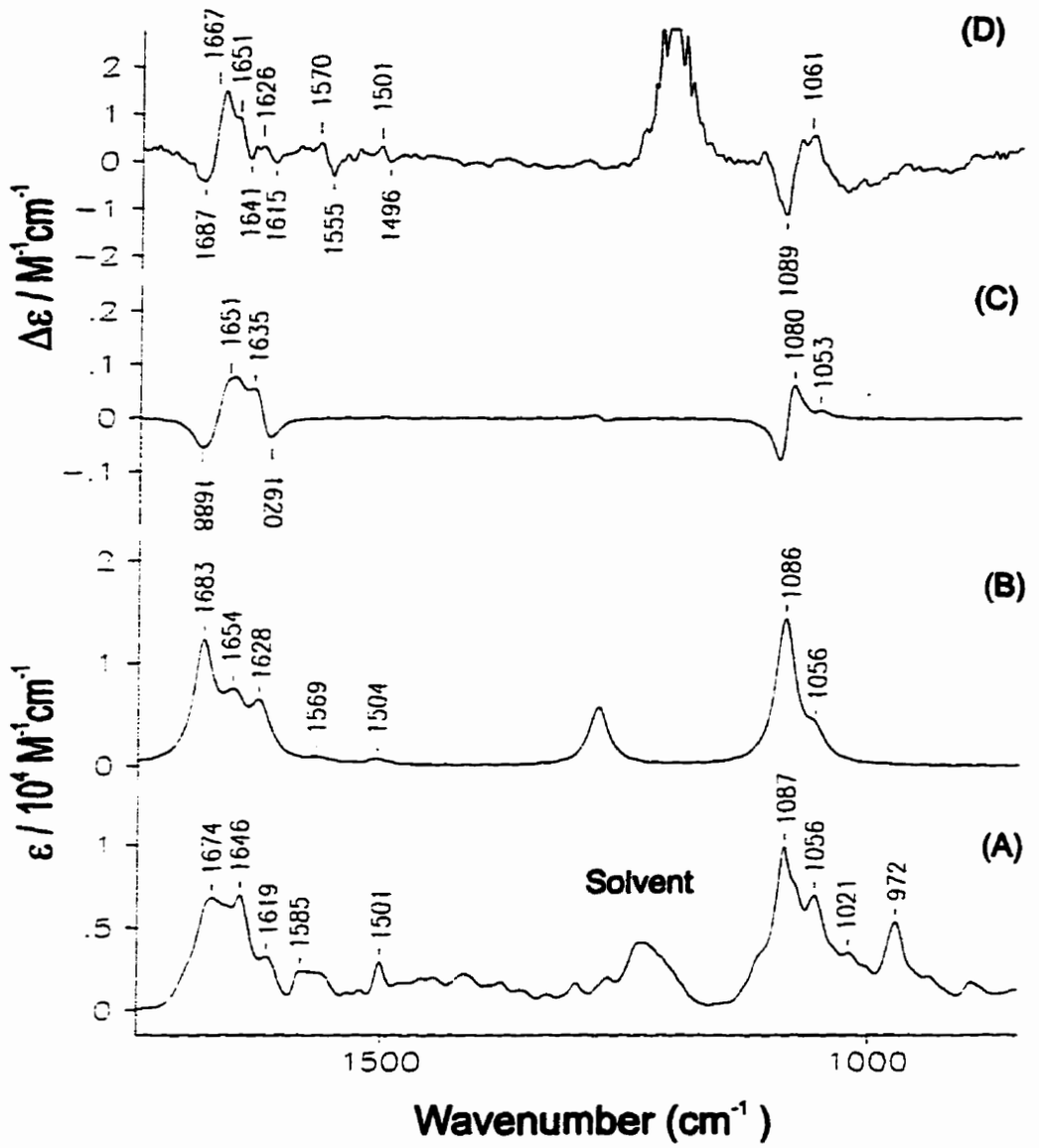

Figure 43
Experimental and Calculated IR Absorption and VCD Spectra of d(CGCATGCG).d(CGCATGCG)-2(Daunorubicin)

Experimental IR absorption (A), calculated IR absorption (B), calculated VCD (C) and experimental VCD (D) spectra.

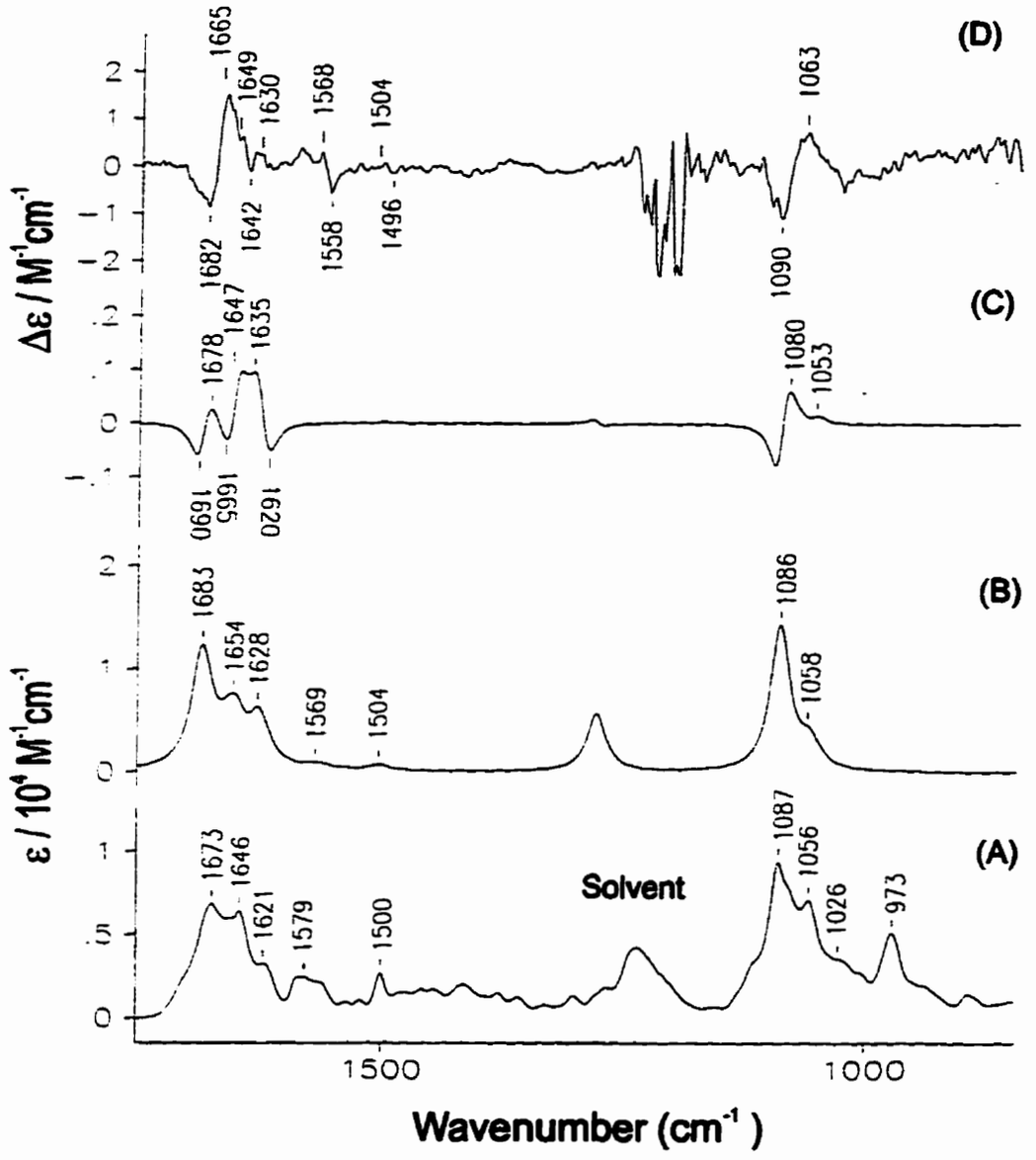

Figure 44
Experimental and Calculated IR Absorption and VCD Spectra of d(CGCTAGCG).d(CGCTAGCG)-2(Daunorubicin)

Experimental IR absorption (A), calculated IR absorption (B), calculated VCD (C) and experimental VCD (D) spectra.

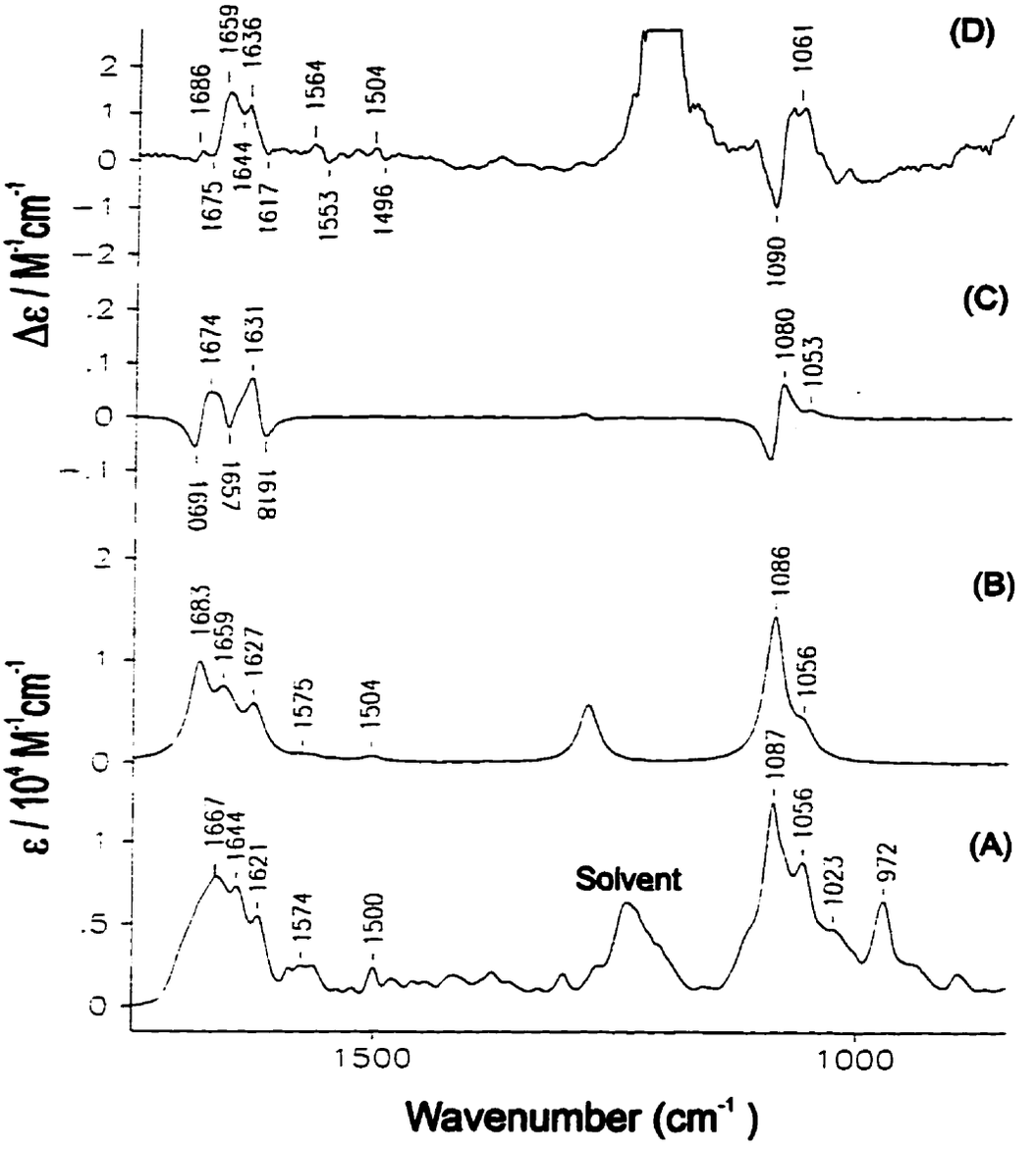

Figure 45
Experimental and Calculated IR Absorption and VCD Spectra of d(CGATATCG).d(CGATATCG)-2(Daunorubicin)

Experimental IR absorption (A), calculated IR absorption (B), calculated VCD (C) and experimental VCD (D) spectra.

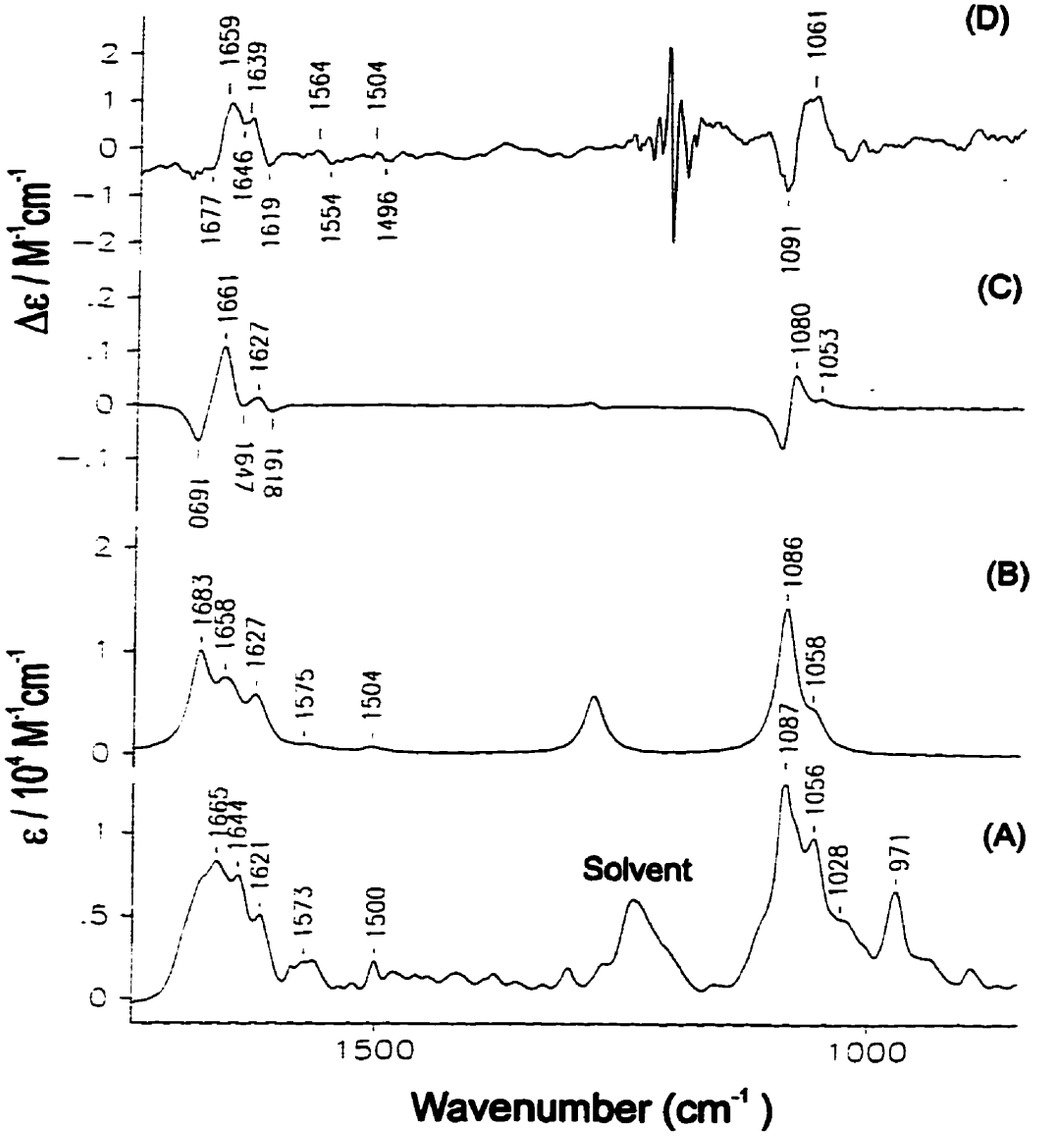

Figure 46
Experimental and Calculated IR Absorption and VCD Spectra of d(CGTATACG).d(CGTATACG)-2(Daunorubicin)

Experimental IR absorption (A), calculated IR absorption (B), calculated VCD (C) and experimental VCD (D) spectra.

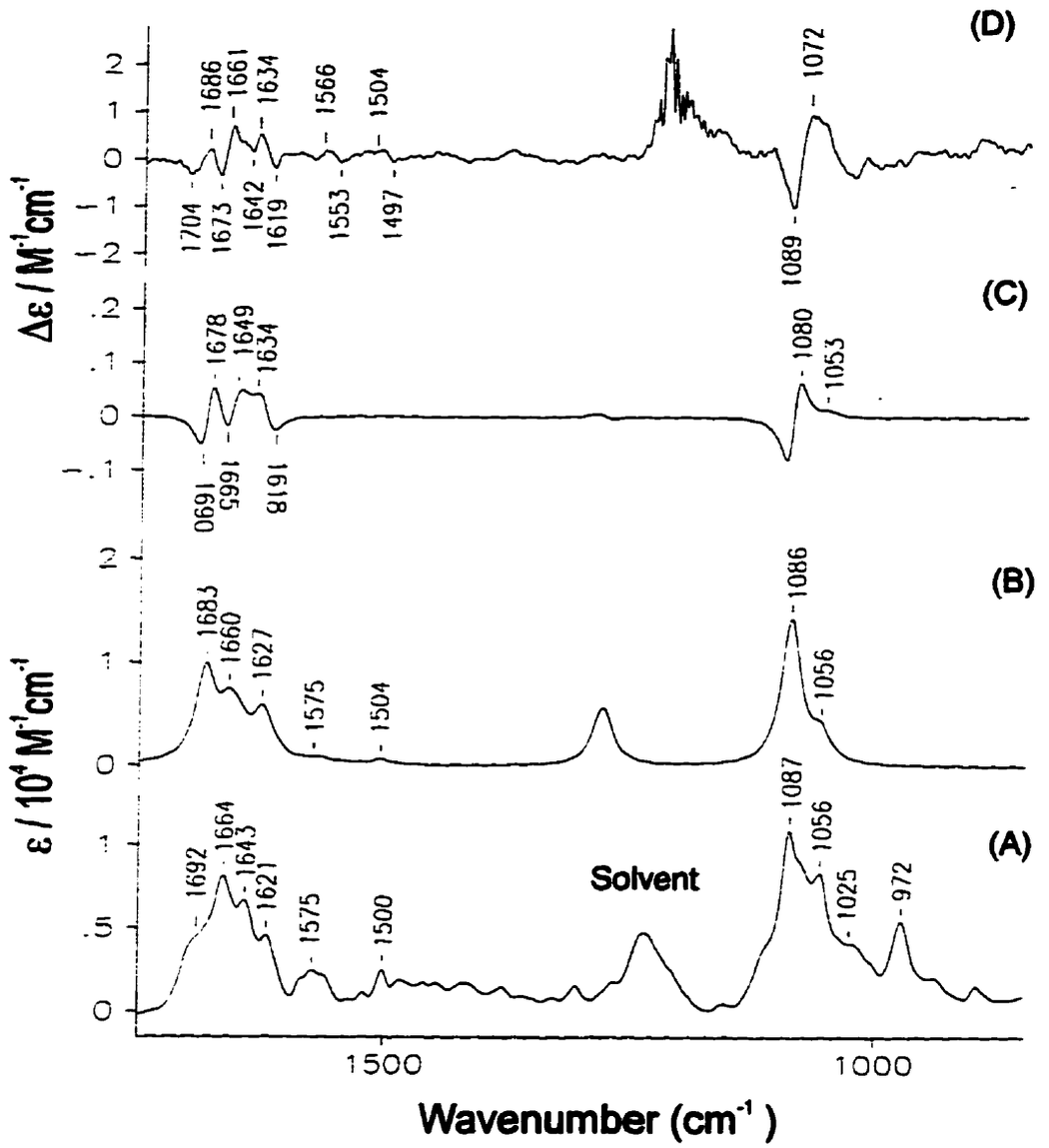

Figure 47
Experimental and Calculated IR Absorption and VCD Spectra of d(CGAATTCG).d(CGAATTCG)-2(Daunorubicin)

Experimental IR absorption (A), calculated IR absorption (B), calculated VCD (C) and experimental VCD (D) spectra.

Table 18
Calculated and Experimental wavenumbers of IR Absorption and VCD of d(CGCGCGCG).d(CGCGCGCG)-2(Daunorubicin)

† Tentative Assignments	‡ $IR_{experimental}$ (cm^{-1})	‡ $IR_{calculated}$ (cm^{-1})	‡ $VCD_{calculated}$ (cm^{-1})	‡ $VCD_{experimental}$ (cm^{-1})
Q11(cg)	1679	1684	1695(-?) 1688(+)	1687(-) 1668(+)
Q12(cg)	1659	-	1678(-) 1651(+)	- -
Q13(cg)	1647	1652	- -	1651(+?) 1640(-)
Q14(cg)	1620	1629	1634(+) 1620(-)	- -
Q15(cg)	1581	-	-	-
Q16(cg)	1562	1566	- -	1568(+) 1556(-)
Q17(cg)	1501	1504	- -	1504(+) 1497(-)
Q19(dmp)	1087	1086	1095(-) 1080(+)	1090(-) 1076(+)
Q20(dmp)	1055	1056	1053(+)	1061(+)
Q30(d)?	1022	-	-	-
Q32(d)?	973	-	-	-

† Refer to Table 5, page 71, Table 8, page 76 and Table 11, page 107.

‡ See Figure 42, page 116.

Table 19
Calculated and Experimental wavenumbers of IR Absorption and VCD of d(CGCATGCG).d(CGCATGCG)-2(Daunorubicin)

† Tentative Assignments	‡ $IR_{experimental}$ (cm^{-1})	‡ $IR_{calculated}$ (cm^{-1})	‡ (cm^{-1})	‡ $VCD_{experimental}$ (cm^{-1})
Q11(cg), Q12(at)	1674	1683	1688(-) 1651(+)	1687(-) 1667(+)
Q13(cg), Q14(at)	1646	1654	- -	1651(+) 1641(-)
Q14(cg), Q15(at)	1619	1628	1635(+) 1620(-)	1636(+?) -
Q15(cg)	1585	-	-	-
Q16(cg)	1562	1569	- -	1570(+) 1555(-)
Q17(cg), Q18(at)	1501	1504	- -	1501(+) 1497(-)
Q19(dmp)	1087	1086	1095(-) 1080(+)	1089(-) 1074(+)
Q20(dmp)	1056	1056	1053(+)	1061(+)
Q30(d)?	1021	-	-	-
Q32(d)?	972	-	-	-

† Refer to Table 5, page 71, Table 7, page 75, Table 8, page 76 and Table 11, page 107.

‡ See Figure 43, page 117.

Table 20
Calculated and Experimental wavenumbers of IR Absorption and VCD of d(CGCTAGCG).d(CGCTAGCG)-2(Daunorubicin)

† Tentative Assignments	‡ $IR_{experimental}$ (cm^{-1})	‡ $IR_{calculated}$ (cm^{-1})	‡ $VCD_{calculated}$ (cm^{-1})	‡ $VCD_{experimental}$ (cm^{-1})
Q11(cg), Q12(at)	1673	1683	1690(-) 1678(+)	1682(-) 1665(+)
Q12(cg), Q13(at)	1651	1654	1665(-) 1647(+)	1649(+) 1642(-)
Q13(cg), Q14(at)	1646	-	-	-
Q14(cg), Q15(at)	1621	1628	1635(+) 1620(-)	1636(+?) -
Q15(cg), Q16(at)	1579	1569	-	-
Q16(cg)	1562	-	-	1568(+) 1558(-)
Q17(cg), Q18(at)	1500	1504	- -	1504(+) 1497(-)
Q19(dmp)	1087	1086	1095(-) 1080(+)	1090(-) 1072(+)
Q20(dmp)	1056	1058	1053(+)	1063(+)
Q30(d)?	1024	-	-	-
Q32(d)?	973	-	-	-

† Refer to Table 5, page 71; Table 7, page 75; Table 8, page 76 and Table 11, page 107.

‡ See Figure 44, page 118.

Table 21
Calculated and Experimental wavenumbers of IR Absorption and VCD of d(CGATATCG).d(CGATATCG)-2(Daunorubicin)

† Tentative Assignments	‡ $IR_{experimental}$ (cm^{-1})	‡ $IR_{calculated}$ (cm^{-1})	‡ $VCD_{calculated}$ (cm^{-1})	‡ $VCD_{experimental}$ (cm^{-1})
Q11(cg), Q12(at)	1667	1683	1690(-) 1674(+)	1675(-) 1659(+)
Q12(cg), Q13(at)	1644	1659	1657(-)	1644(-?)
Q14(cg), Q15(at)	1621	1627	1631(+) 1618(-)	1636(+) 1617(-)
Q16(at)	1574	1575	-	-
Q16(cg)	1564	-	-	1564(+) 1553(-)
Q17(cg), Q18(at)	1500	1504	- -	1504(+) 1496(-)
Q19(dmp)	1087	1086	1095(-) 1080(+)	1090(-) 1072(+)
Q20(dmp)	1056	1056	1053(+)	1061(+)
Q30(d)?	1023	-	-	-
Q32(d)?	972	-	-	-

† Refer to Table 5, page 71; Table 7, page 75; Table 8, page 76 and Table 11, page 107.

‡ See Figure 45, page 119.

Table 22
Calculated and Experimental wavenumbers of IR Absorption and VCD of d(CGTATACG).d(CGTATACG)-2(Daunorubicin)

† Tentative Assignments	‡ $IR_{experimental}$ (cm^{-1})	‡ $IR_{calculated}$ (cm^{-1})	‡ $VCD_{calculated}$ (cm^{-1})	‡ $VCD_{experimental}$ (cm^{-1})
Q11(cg), Q12(at)	1665	1683	1690(-) 1661(+)	1677(-) 1659(+)
Q12(cg), Q13(at)	1644	1658	1647(-?)	1646(-?) -
Q14(cg), Q15(at)	1621	1627	1627(+) 1618(-)	1639(+) 1619(-)
Q16(at)	1573	1575	-	-
Q16(cg)	1564	-	-	1564(-?) 1554(+)
Q17(cg), Q18(at)	1500	1504	- -	1504(+) 1496(-)
Q19(dmp)	1087	1086	1095(-) 1080(+)	1090(-) 1074(+)
Q20(dmp)	1056	1058	1053(+)	1061(+)
Q30(d)?	1025	-	-	-
Q32(d)?	971	-	-	-

† Refer to Table 5, page 71; Table 7, page 75; Table 8, page 76 and Table 11, page 107.

‡ See Figure 46, page 120.

Table 23
Calculated and Experimental wavenumbers of IR Absorption and VCD of d(CGAATTCG).d(CGAATTCG)-2(Daunorubicin)

† Tentative Assignments	‡ $IR_{experimental}$ (cm^{-1})	‡ $IR_{calculated}$ (cm^{-1})	‡ $VCD_{calculated}$ (cm^{-1})	‡ $VCD_{experimental}$ (cm^{-1})
Q11(cg), Q12(at)	1692	1683	1690(-) 1678(+)	1704(-) 1686(+)
Q12(cg), Q13(at)	1664	1660	1665(-) 1649(+)	1673(-) 1661(+)
Q13(cg), Q14(at)	1643	-	1640(-?)	1642(-?)
Q14(cg), Q15(at)	1621	1627	1634(+) 1618(-)	1634(+) 1619(-)
Q16(at)	1575	1575	- -	1566(+) 1553(-)
Q16(cg)	1564	-	-	-
Q17(cg), Q18(at)	1500	1504	- -	1504(+) 1497(-)
Q19(dmp)	1087	1086	1095(-) 1080(+)	1089(-) 1072(+)
Q20(dmp)	1056	1056	1053(+)	1057(+)
Q30(d)?	1025	-	-	-
Q32(d)?	972	-	-	-

† Refer to Table 5, page 71; Table 7, page 75; Table 8, page 76 and Table 11, page 107.

‡ See Figure 47, page 121.

6. Summary and Future Work

6.1 Summary

Vibrational circular dichroism (VCD) spectroscopy identifies the three dimensional conformation and absolute configuration of optically active systems for it is a differential measurement of circularly polarized infrared radiation. VCD spectra by their nature offer information and detail additional to their parent IR spectra. The desire to understand DNA-drug interactions inspired this research project, to investigate whether VCD was capable of revealing sequence specificity in the selected self-complementary deoxyoctanucleotides of the type d(CGNNNNCG).d(CGNNNNCG) where N could be A, C, G or T, and subsequently to examine interactions with the anti-tumor drug daunorubicin. Currently, daunorubicin is clinically used for the treatment of acute leukemia.

The primary objectives of this study were achieved, viz.

a) Systematic relationships between deoxyoctanucleotide structural characteristics and spectral features arising from VCD spectroscopy were established.

b) The utility of VCD spectroscopy as an analytic method for probing conformational changes accompanying deoxyoctanucleotide-daunorubicin complexes interactions were demonstrated.

The selected deoxyoctanucleotides were synthesized by using automated phosphoramidite chemistry on a DNA synthesizer, purified using the principle of molecular weight exclusion, assessed by polyacrylamide gel electrophoresis and analyzed by ultraviolet (UV), electronic circular dichroism (ECD) and melting temperature (T_m) measurements. Daunorubicin is an anti-tumor intercalating drug which inserts itself between two stacked C-G base-pairs. In order to accommodate the daunorubicin the DNA helix unwinds and

lengthens, hence profoundly changing the DNA topology which inhibits DNA replication and transcription processes, thereby stopping cell proliferation. Daunorubicin does exhibit DNA sequence preference as reported previously in the literature.

The UV absorption and ECD spectra of the selected deoxyoctanucleotides were measured in the 31250-50000 cm^{-1} range. Particularly prominent ECD features occur between 33300-42500 cm^{-1} (300-235 nm) and are ascribed to the $\pi \rightarrow \pi^*$ electronic transitions of the stacked nucleotide bases. The FT-IR absorption and VCD spectra of the selected deoxyoctanucleotides and their daunorubicin complexes were measured in the continuous 1750-850 cm^{-1} range, which has not been reported previously. The most prominent VCD features occur between 1750-1600 cm^{-1}, resulting from the dipolar coupling of carbonyl and/or skeletal stretching vibrations of the stacked nucleotide bases, and 1100-1050 cm^{-1} due to the symmetric PO_2^- stretching vibrations of the sugar-phosphate backbone. For the deoxyoctanucleotides with varying sequences the structural changes were monitored by shifted wavenumbers and varied intensities in the VCD spectra. The nucleotide base modes appear to reveal sequence specificity in contrast to the phosphate backbone vibrations, which show the handedness of the helix. VCD features seem to give more detailed sequence specificity compared to conventional IR absorption and ECD spectra. Upon intercalation with daunorubicin, deoxyoctanucleotides containing the most preferred daunorubicin triplet sequences revealed markedly diminished C-G base-pair contributions in the VCD spectra, thus suggesting that the dipolar coupling between the C-G base-pairs is extensively disrupted, which is consistent with daunorubicin intercalating between the C-G base-pairs, according to previous literature.

An approximate computational method, viz. the non-degenerate extended coupled oscillator (NECO) model was used to simulate the two regions of interest concurrently for both the FTIR/VCD spectra of the selected deoxyoctanucleotides and their daunorubicin complexes, and the single region of interest for the UV/ECD spectra of the deoxyoctanucleotides. The NECO model assumes that the predominant interaction is due

to dipolar coupling of the stacked nucleotide bases and the phosphate backbone in the helical orientation. The vibrational transitions are assigned on the basis of *ab initio* harmonic wavenumbers and intensities while the electronic transitions are assigned on the basis of *ab initio* excitation energies. Optimized geometries, harmonic force fields and atomic polar tensors (electric transition dipole moments) of the nucleotide bases (C, G, A and T), nucleotide base pairs (C-G and A-T) and the dimethyl phosphate anion were calculated using density functional theory (DFT) with B3-LYP functionals and the 6-31G** basis set. Atomic polar tensors of the nucleotide bases were also calculated with single point calculations using configuration interaction singles (CIS) with the 6-31+G* basis set, for simulating UV/ECD spectra of the deoxyoctanucleotides. The standard B-DNA conformation of the selected deoxyoctanucleotides were generated using MSI's molecular modeling system and were modified to incorporate daunorubicin at the terminal base-pairs. Accordingly, the parameters required by the NECO model, viz. the vibrational wavenumbers and the electric transition dipole moments (magnitude and orientation), were derived from *ab initio* calculations and the latter was transformed to helical coordinates while the former was adjusted according to experimental IR spectra before implementation into the NECO model.

For a simplistic model, the NECO model simulates the overall features of the FTIR/VCD spectra of the deoxyoctanucleotides and their daunorubicin complexes adequately. The overall features of ECD spectra agree reasonably well with those simulated by the NECO model for the deoxyoctanucleotides.

6.2 Future Work

The study of DNA with VCD spectroscopy constitutes a relatively new field and it therefore appeared most appropriate to consider prominent occurrences rather than subtleties, which are not considered trivial, but less informative without the broader picture.

6.2.1 Variations in Environmental Conditions

DNA conformation is known to be susceptible to environmental conditions, e.g. salt concentration, extent of hydration and temperature (Blackburn, 1990).

DNA structure changes with pH hence deoxyoctanucleotides at physiological pH will reproduce *in vivo* occurrences most appropriately. The fact that protonation and deprotonation of nucleotide bases occur within 2 pH units from neutrality (Saenger, 1984) in conjunction with the knowledge that VCD exhibits pH sensitivity (Zuk *et al.*, 1989), suggests that the pH range between 5 and 9 could prove useful in identifying VCD features.

Varying salt concentrations, dehydrating (alcohol) conditions and temperature are associated with the different phase transitions in DNA. The salt concentration required for a particular transition depends upon the type of salt used, e.g. NaCl, $MgCl_2$ and $MnCl_2$ require successively lower salt concentrations for the B- to Z- transition of DNA. The first row transition metals can induce Z-conformations of poly(dG-dC).poly(dG-dC) at submillimolar concentrations and in the absence of a dehydrating solvent (van de Sande *et al.*, 1982). It has been suggested than Mn^{2+} reacts with the lone pairs on the nitrogen atom of bases, viz. N7 of G, in addition to the phosphate group which is the major reaction site of monovalent and divalent cations (excluding the first row transition metals). This can be substantiated by the major groove determinants of G (including N7) in Z- but not B-DNA being completely exposed to the environment. A dehydrating solvent (alcohol) causes a B- to A- or Z-DNA phase transition (Blackburn, 1990), whereas heat generally accelerates the DNA phase transitions.

The effects of the environmental conditions, namely pH, ionic (salt concentration), dehydration and temperature, can therefore be investigated.

6.2.2 Polarity of DNA

A-, B- and Z-DNA duplexes possess the antiparallel orientation of the complementary strands and the exclusive occurrence of Watson-Crick type base-pairing. Parallel-stranded (PS) structural components originate as a prerequisite in triple- and tetra-stranded nucleic acid helices (Germann *et al.*, 1995). The ability of certain DNA sequences to form PS duplexes with A-T base-pairing in which both strands have the same 5′→ 3′ orientation is well established (Rippe & Jovin, 1992). The spectroscopic, thermodynamic and biochemical properties of PS-DNA differ from those of conventional antiparallel (APS) B-DNA, nonetheless the former are remarkably stable under physiological conditions.

Stable PS-DNA were formed with sequences containing reverse Watson-Crick A-T base-pairs, whose hydrogen bonding potential is analogous to the conventional Watson-Crick structure. The incorporation of C-G base-pairs, on the other hand, results in a reduced stability of the PS duplex structure due to the loss of at least one hydrogen bond per reverse Watson-Crick C-G base-pair (van de Sande *et al.*, 1988). However, an α-anomeric nucleotide inserted into an APS-DNA sequence in a parallel orientation via 3′→ 3′ and 5′→ 5′ phosphodiester bonds exhibit normal Watson-Crick type base-pairing and as such displays the coexistence of PS- and APS-DNA (Aramini *et al.*, 1996). Apart from A-T and C-G base-pairs, homo base-pairs such as G-G and A-A have also been incorporated into nucleotide sequences to form stable PS-DNA (Rippe *et al.*, 1992).

Initially, PS-DNA structures were formed from DNA hairpins containing the homooligomeric self-complementary sequence d(AAAAAAAAAA).d(TTTTTTTTTT), connected by a four-nucleotide hairpin loop (either C or G) with either 3′→ 3′ or a 5′→ 5′ phosphodiester linkage which served to selectively stabilize intramolecular PS-DNA formation (van de Sande *et al.*, 1988). Such structural constraints were not prerequisite as

conventional deoxyoligonucleotides with appropriate sequence homology could also form PS-DNA (Germann *et al.*, 1988).

Melting temperature measurements of various PS- and conventional APS-DNA duplexes, with and without hairpin loops revealed that both, PS- and APS-DNA, underwent a thermally induced helix to coil transition, but the T_m for the PS-DNA was 22° lower (Germann *et al.*, 1988). The minor groove binding drug, Hoechst 33258, which requires approximately four A-T base-pair determinants, showed a reduced affinity for the homooligomeric PS dA.dT hairpin due to the difference in groove dimensions and the presence of thymine methyl groups at the binding site (Zhou *et al.*, 1993). Replacement of the methyl group with hydrogen, i.e. thymine substituted with uracil, exhibited an approximately two-fold stronger Hoechst 33258 binding to the homooligomeric PS dU.dT hairpin, whereas the binding affinity was similar for both APS dA.dT and APS dA.dU hairpins (Germann *et al.*, 1996).

A VCD investigation of PS- versus APS-DNA with A-T base-pairs (homooligomeric versus alternating), the introduction of C-G base-pairs to examine the destabilization of the PS-DNA helices, and the incorporation G-G and A-A homo base-pairs, should prove to be most fascinating. In addition, the coexistence of short PS- and APS-DNA in the presence of α-anomeric nucleotides can be considered, which has potential relevance in the area of antisense therapy (Aramini *et al.*, 1996).

6.2.3 DNA-Drug Interactions

Upon binding intercalating drugs cause unwinding and lengthening of the DNA helix whereas groove-binding drugs displace the spine of hydration in the DNA minor groove and reproduce its coordination, hence the former changes the DNA conformation more profoundly than the latter upon binding. Since daunorubicin has been extensively studied in this research it could provide a guideline for the VCD investigation of other intercalating drugs such as nogalamycin, an anthracycline antibiotic used as a cytostatic

agent, whose intercalation with deoxyhexanucleotides has recently been reported with FTIR spectroscopy (Missailidis & Hester, 1995). It will be of interest to examine the type of information, if any, that arises from VCD spectroscopy regarding the effects of groove-binding drugs such as netropsin and distamycin on DNA.

Parallel-stranded DNA drug interactions (e.g. Hoechst 33258) will definitely be worth investigating for both the 1100-1050 cm^{-1} region attributed to the PO_2^- symmetric stretching vibration and the 1750-1600 cm^{-1}region arising from carbonyl and/or skeletal stretching vibrations of the nucleotide bases will be affected in comparison to the conventional antiparallel-stranded DNA.

6.2.4 Computations

Purely *ab intio* computations are ideally desired, however, the computer limitations make such calculations impossible for the large systems used in this study. The vibronic coupling theory (VCT) and the magnetic field perturbation (MFP) constitute non-empirical calculations which have successfully simulated IR and VCD spectra (Freedman & Nafie, 1994), however they are exclusive to small molecules. Empirical parameters are therefore used in conjunction with *ab initio* computed components, for large molecular systems. As an example, the empirical parameter of the NECO model was the adjustment of *ab initio* computed base-pair wavenumbers (in the gas-phase) to experiment (in solution), which is extremely challenging when making assignments from partially resolved IR absorption spectra. Adopting more parameters in order to fit calculated results with experiment, has the danger of losing *ab initio* information. However, correct frequency analysis of a large system like the deoxyoctanucleotides is possible if one were to derive reasonable harmonic force fields built from smaller subunits (Bour *et al.*, 1996). The future of calculating deoxyoctanucleotides and their daunorubicin complexes might reside in a combined quantum mechanical and molecular mechanical (QM/MM) approach .

Bibliography

Annamalai, A. and Keiderling, T.A. (1987) *J. Am. Chem. Soc.* **109**, 3125-3132.

Aramini, J.M.; Kalisch, B.W.; Pon, R.T.; van de Sande, J.H. and Germann, M.W. (1996) *Biochemistry* **35**, 9355-9365.

Arcamone, F. *DOXORUBICIN Anticancer Antibiotics*, **Vol. 17**, Academic Press Inc. New York (1981a) pp 1-47.

Arcamone, F. *DOXORUBICIN Anticancer Antibiotics*, **Vol. 17**, Academic Press Inc. New York (1981b) pp 93-125.

Becke, A.D. (1993) *J. Chem. Phys.* **98**, 5648-5652.

Birke, S.S.; Moses, M.; Kagalovsky, B.; Jano, D.; Gulotta, M. and Diem, M. (1993) *Biophys. J.* **65**, 1262-1271.

Birke, S.S. and Diem, M. (1995) *Biophys. J.* **68**, 1045-1049.

Blackburn, G.M. and Gait, M.J. *Nucleic Acids in Chemistry and Biology* (G.M.Blackburn and M.J.Gait, Eds.) Oxford University Press, New York (1990) pp 106-123.

Blackburn, G.M. *Nucleic Acids in Chemistry and Biology* (G.M.Blackburn and M.J.Gait, Eds.) Oxford University Press, NY (1990) pp 17-52.

Bour, P. and Keiderling, T.A. (1993) *J. Am. Chem. Soc.* **115**, 9602-9607.

Bour, P.; Maharaj, V.; Rauk, A. and Wieser, H. (work in progress).

Branden, C. and Tooze, J. *Introduction to Protein Structure* (C.Branden, Ed.) Garland Publishing Inc. New York (1991) pp 269-285.

Broyde, S.; Hingerty, B. and Stellman, S. *Discipline Biomolecular Stereodynamics*, **Vol. II** (R.H.Sarma, Ed.) Adenine Press, New York (1981) pp 455-467.

Bush, C.A.*Basic Principles in Nucleic Acid Chemistry*, **Vol. 2** (P.O.P.Ts'o, Ed.) Academic Press Inc. New York (1974) pp 91-169.

Caruthers, M.H. (1985) *Science* **230**, 281-285.

Chaires, J.B. (1983) *Biochemistry* **22**, 4204-4211.

Chaires, J.B. (1990) *Biophys. Chem.* **35**, 191-202.

Chaires, J.B.; Fox, K.R.; Herrera, J.E.; Britt, M. and Waring, M.J. (1987) *Biochemistry* **26**, 8227-8236.

Chaires, J.B.; Herrera, J.E. and Waring, M.J. (1990) *Biochemistry* **29**, 6145-6153.

Chen, K.-X.; Gresh, N. and Pullman, B. (1985) *J. Biomol. Struct. & Dyn.* **3**, 445-466.

Crothers, D.M. (1968) *Biopolymers* **6**, 575-584.

Dickerson, R.E.*Structure & Methods*, **Vol. 3** (R.H.Sarma and M.H.Sarma, Eds.) Adenine Press, New York (1990) pp 1-39.

Diem, M. (1991) *SPIE Biomolec. Spectrosc.* **1432**, 28-36.

Florian, J. and Leszczynski, J. (1995) *Int. J. Quant. Chem.* **22**, 207-225.

Florian, J.; Baumruk, V.; Strajbl, M.; Bednarova, L. and Stepanek, J. (1996) *J. Phys. Chem.* **100**, 1559-1568.

Fogarasi, G. and Pulay, P.*Vibrational Spectra and Structure*, **Vol. 14** (J.R.Durig, Ed.) Elsevier, Amsterdam (1985) pp 125-219.

Frederick, C.A.; Williams, L.D.; Ughetto, G.; van der Marel, G.A.; van Boom, J.H.; Rich, A. and Wang, A.H.-J. (1990) *Biochemistry* **29**, 2538-2549.

Freedman, T.B. and Nafie, L.A. (1993) *Methods Enzymol.* **226**, 306-319.

Freedman, T.B. and Nafie, L.A. *Modern Nonlinear Optics, Part 3*, **Vol. 135** (M.Evans and S.Kielich, Eds.) John Wiley & Sons Inc. New York (1994) pp 207-263.

Freedman, T.B. and Nafie, L.A. *Topics in Stereochemistry*, **Vol. 17** (E.L.Eliel and S.H.Wilen, Eds.) Wiley, New York (1987) pp 113-206.

Frisch, M.J.; Trucks, G.W.; Schlegel, H.B.; Gill, P.M.W.; Johnson, B.G.; Robb, M.A.; Cheeseman, J.R.; Keith, T.; Petersson, G.A.; Montgomery, J.A.; Raghavachari, R.; Al-Laham, M.A.; Zakrzewski, V.G.; Ortiz, J.V.; Foresman, J.B.; Peng, C.Y.; Ayala, P.Y.; Chen, W.; Wong, M.W.; Andres, J.L.; Replogle, E.S.; Gomperts, R.; Martin, R.L.; Fox, D.J.; Binkley, J.S.; Defrees, D.J.; Baker, J.; Stewart, J.P.; Head-Gordon, M.; Gonzalez, C. and Pople, J.A. , *Gaussian 94, Revision B.3* (1995) Gaussian Inc. Pittsburgh, PA.

Germann, M.W. (1989) Thesis/Dissertation. *Unusual DNA Structures.* pp.36-39. University of Calgary, Canada.

Germann, M.W.; Kalisch, B.W. and van de Sande, J.H. (1988) *Biochemistry* **27**, 8302-8306.

Germann, M.W.; Kalisch, B.W. and van de Sande, J.H. (1996) *J. Biomol. Struct. & Dyn.* **13**, 953-961.

Germann, M.W.; Zhou, N.; van de Sande, J.H. and Vogel, H.J. (1995) *Methods Enzymol.* **261**, 207-225.

Gould, I.R.; Vincent, M.A. and Hillier, I.H. (1993) *Spectrochim. Acta* **49A**, 1727-1734.

Gould, I.R.; Vincent, M.A.; Hillier, I.H.; Lapinski, L. and Nowak, M.J. (1992) *Spectrochim. Acta* **48A**, 811-818.

Gulotta, M.; Goss, D.J. and Diem, M. (1989) *Biopolymers* **28**, 2047-2058.

Ho, P.S.; Frederick, C.A.; Quigley, G.J.; van der Marel, G.A.; van Boom, J.H.; Wang, A.H.-J. and Rich, A. (1985) *EMBO J.* **4**, 3617-3623.

Holzwarth, G. and Chabay, I. (1972) *J. Chem. Phys.* **57**, 1632-1635.

Insight II , 95.0 (1995) Molecular Simulations Inc. San Diego.

Jorgenson, K.F. (1981) Thesis/Dissertation. *Probes for Chromosome Structure.* University of Calgary, Canada.

Keiderling, T.A. and Pancoska, P. *Advances in Spectroscopy*, **Vol. 21** (R.J.H.Clark and R.E.Hester, Eds.) John Wiley & Sons, New York (1993) pp 267-315.

Keiderling, T.A.; Yasui, S.C.; Pancoska, P.; Dukor, R.K. and Yang, L. (1989) *SPIE Biomolec. Spectrosc.* **1057**, 7-14.

Keiderling, T.A. *Practical Fourier Transform Infrared Spectroscopy* (J.R.Ferraro and K.Krishnan, Eds.) Academic Press Inc. San Diego (1990) pp 203-284.

Kennard, O. and Hunter, W.N. (1991) *Angew. Chem. Int. Ed. Engl.* **30**, 1254-1277.

Krogh, C.M.E.*CPS: Compendium of Pharmaceuticals and Specialties* (C.M.E. Krogh, Ed.) Canadian Pharmaceutical Association, Ottawa (1995) pp.243-244.

Lab Calc , C2.24 (1992) Galactic Industries Coporation, New Hampshire, USA.

Lal, B.B. and Nafie, L.A. (1982) *Biopolymers* **21**, 2161-2183.

Les, A.; Adamowica, L.; Nowak, M.J. and Lapinski, L. (1992) *Spectrochim. Acta* **48A**, 1385-1395.

Leszczynski, J. (1992) *Int. J. Quant. Chem.* **19**, 43-55.

Maharaj, V.; Tsankov, D.; van de Sande, J.H. and Wieser, H. (1995) *J. Molec. Struct.* **349**, 25-28.

Manfait, M. and Theophanides, T. *Advances in Spectroscopy*, (R.J.H.Clark and R.E.Hester, Eds.) John Wiley & Sons Inc. New York (1986) pp 311-346.

Manfait, M.; Bernard, L. and Theophanides, T. (1981) *J. Raman Spectrosc.* **11**, 68-74.

Manfait, M.; Theophanides, T.; Alix, A.J.P. and Jeannesson, P. *Spectroscopy of Biological Molecules* (C.Sandorfy and T.Theophanides, Eds.) D. Reidal Publishing Company, Dordrecht, Holland (1984) pp 113-116.

Maniatis, T.; Fritsch, E.F. and Sambrook, J.*Molecular Cloning*, Cold Spring Harbor Laboratory, New York (1982)

McGhee, J.D. and von Hippel, P.H. (1974) *J. Mol. Biol.* **86**, 469-489.

Missailidis, S. and Hester, R.E. (1995) *Biospectroscopy* **1**, 91-99.

Moffitt, W. (1956) *J. Chem. Phys.* **25**, 467-478.

Nafie, L.A. and Diem, M. (1979) *Appl. Spectrosc.* **33**, 130-135.

Nafie, L.A. and Freedman, T.B. (1987) *Spectroscopy* **2**, 24-29.

Neidle, S. *X-ray Crystallography and Drug Design* (A.S.Horn and C.J.De Ranter, Eds.) Claredon Press, Oxford, U.K (1984) pp 129-150.

Nishimura, Y. and Tsuboi, M.*Advances in Spectroscopy*, **Vol. 13** (R.J.H.Clark and R.E.Hester, Eds.) John Wiley & Sons Ltd. New York (1986) pp 177-232.

Nowak, M.J.; Rostkowska, H.; Lapinski, L.; Kwiatkowski, J.S. and Leszczynski, J. (1994) *Spectrochim. Acta* **50A**, 1081-1094.

Pancoska, P. and Keiderling, T.A. (1991) *Biochemistry* **30**, 6885-6895.

Pancoska, P.; Yasui, S.C. and Keiderling, T.A. (1989) *Biochemistry* **28**, 5917-5923.

Pancoska, P.; Yasui, S.C. and Keiderling, T.A. (1991) *Biochemistry* **30**, 5089-5103.

Patel, D.J.; Kozlowski, S.A. and Rice, J.A. (1981) *Proc. Natl. Acad. Sci. (U. S. A.)* **78**, 3333-3337.

Pindur, U.; Haber, M. and Sattler, K. (1993) *J. Chem. Ed.* **70**, 263-272.

Pohle, W. and Flemming, J.*Spectroscopy of Biological Molecules*, (A.J.P.Alix, L.Bernard, and M.Manfait, Eds.) Wiley, Chichester (1985) pp 254-256.

Rauhut, G. and Pulay, P. (1995) *J. Phys. Chem.* **99**, 3093-3100.

Rauk, A. and Freedman, T.B. (1994) *Int. J. Quant. Chem.* **28**, 315-338.

Rauk, A. *New Developments in Molecular Chirality*, (P.G.Mezey, Ed.) Kluwer Academic Publishers, Netherlands (1991) pp 57-92.

Rauk, A. *Orbital Interaction Theory of Organic Chemistry*, (A.Rauk, Ed.) John Wiley & Sons Inc. New York (1994) pp 18-56.

Rippe, K. and Jovin, T.M. (1992) *Methods Enzymol.* **211**, 199-220.

Rippe, K.; Fritsch, V.; Westhof, E. and Jovin, T.M. (1992) *EMBO J.* **11**, 3777-3786.

Saenger, W. *Principles of Nucleic Acid Structure*, (C.R.Cantor, Ed.) Spring-Verlag Inc. New York (1984) pp 105-115.

Saenger, W. *Principles of Nucleic Acid Structure*, (C.R.Cantor, Ed.) Springer-Verlag Inc. New York (1984a) pp 116-158.

Saenger, W. *Principles of Nucleic Acid Structure*, (C.R.Cantor, Ed.) Spring-Verlag Inc. New York (1984b) pp 220-241.

Sen, A.C. and Keiderling, T.A. (1984) *Biopolymers* **23**, 1519-1532.

Sheardy, R.D. (1991) *Spectroscopy* **6**, 14-17.

Sorber, H.A. *Handbook of Biochemistry* (H.A.Sorber, Ed.) CRC Press, Cleveland (1970) pp.G-8

Sponer, J.; Leszczynski, J. and Hobza, P. (1996) *J. Biomol. Struct. & Dyn.* **14**, 117-135.

Sprecher, C.A. and Johnson, W.C., Jr. (1977) *Biopolymers* **16**, 2243-2264.

Suarato, A. *The Chemistry of Antitumor Agents* (D.E.V.Wilman, Ed.) Blackie and Son Ltd. (1990) pp 30-62.

Suarato, A. *The Chemistry of Antitumor Agents* (D.E.V.Wilman, Ed.) Blackie and Son Ltd. (1990) pp 30-62.

Taillandier, E.; Liquier, J. and Taboury, J.A. *Advances in Infrared and Raman Spectroscopy*, **Vol. 12** (R.J.H.Clark and R.E.Hester, Eds.) Wiley Heyden, New York (1985) pp 65-114.

Taillandier, E. *Structure & Methods*, **Vol. 3** (R.H.Sarma and M.H.Sarma, Eds.) Adenine Press, New York (1990) pp 73-78.

Tinoco Jr., I. (1963) *Radiat. Res.* **20**, 133-139.

Tsankov, D.; Eggimann, T. and Wieser, H. (1995) *Appl. Spectrosc.* **49**, 132-138.

Tsuboi, M.; Takahashi, S. and Harada, I. *Physico-Chemical Properties of Nucleic Acids*, **Vol. 2** (J.Duchesne, Ed.) Academic Press Inc. New York (1973) pp 91-145.

Tsuboi, M. *Basic Principles in Nucleic Acid Chemistry*, **Vol. 1** (P.O.P.Ts'o, Ed.) Academic Press Inc. New York (1974) pp 399-452.

van de Sande, J.H.; McIntosh, L.P. and Jovin, T.M. (1982) *EMBO J.* **1**, 777-782.

van de Sande, J.H.; Ramsing, N.B.; Germann, M.W.; Elhorst, W.; Kalisch, B.W.; Kitzing, E.V.; Pon, R.T.; Clegg, R.C. and Jovin, T.M. (1988) *Science* **241**, 551-557.

Wang, A.H.-J. and Gao, Y.-G. (1990) *Methods* **1**, 91-99.

Wang, A.H.-J.; Ughetto, G.; Quigley, G.J. and Rich, A. (1987) *Biochemistry* **26**, 1152-1163.

Wang, L. and Keiderling, T.A. (1992) *Biochemistry* **31**, 10265-10271.

Wang, L.; Pancoska, P. and Keiderling, T.A. (1994a) *Biochemistry* **33**, 8428-8435.

Wang, L.; Yang, L. and Keiderling, T.A. (1994b) *Biophys. J.* **67**, 2460-2467.

Wang, Y.; Thomas, G.A. and Peticolas, W.L. (1987) *J. Biomol. Struct. & Dyn.* **5**, 249-274.

Wilson, W.D. *Nucleic Acids in Chemistry and Biology* (G.M.Blackburn and M.J.Gait, Eds.) Oxford University Press, New York (1990) pp 295-336.

Wyssbrod, H.R. and Diem, M. (1992) *Biopolymers* **32**, 1237-1242.

Xiang, T.; Goss, D.J. and Diem, M. (1993) *Biophys. J.* **65**, 1255-1261.

Xie, P. and Diem, M. (1995) *J. Am. Chem. Soc.* **117**, 429-437.

Yang, D. and Rauk, A. *Reviews in Computational Chemistry*, **Vol. 7** (K.B.Lipkowitz and D.B.Boyd, Eds.) VCH Publishers, Inc. New York (1996) pp 261-301.

Yang, L. and Keiderling, T.A. (1993) *Biopolymers* **33**, 315-327.

Zhong, W.; Gulotta, M.; Goss, D.J. and Diem, M. (1990) *Biochemistry* **29**, 7485-7491.

Zhou, N.; Germann, M.W.; van de Sande, J.H.; Pattabiraman, N. and Vogel, H.J. (1993) *Biochemistry* **32**, 646-656.

Zuk, W.M.; Freedman, T.B. and Nafie, L.A. (1989) *J. Phys. Chem.* **93**, 1771-1779.

Appendices

Appendix 1: Standard Geometry Coordinates

Table 24
Standard Geometry Coordinates of the Purines

Adenine

No.	Atom	x	y	z
1	N	-2.153	0.126	0.000
2	C	-1.907	1.484	0.000
3	C	-0.925	-0.499	0.000
4	H	-3.050	-0.336	0.000
5	N	-0.631	1.784	0.000
6	C	0.000	0.551	0.000
7	N	-0.654	-1.811	0.000
8	H	-2.716	2.202	0.000
9	C	1.360	0.173	0.000
10	C	0.665	-2.029	0.000
11	N	2.361	1.082	0.000
12	N	1.670	-1.137	0.000
13	H	0.974	-3.072	0.000
14	H	3.314	0.758	0.000
15	H	2.152	2.066	0.000

Guanine

No.	Atom	x	y	z
1	N	2.176	0.728	0.000
2	C	1.835	2.070	0.000
3	C	1.002	0.021	0.000
4	H	3.101	0.326	0.000
5	N	0.542	2.265	0.000
6	C	0.000	0.993	0.000
7	N	0.891	-1.331	0.000
8	H	2.589	2.845	0.000
9	C	-1.375	0.568	0.000
10	C	-0.362	-1.732	0.000
11	O	-2.417	1.200	0.000
12	N	-1.431	-0.872	0.000
13	N	-0.630	-3.067	0.000
14	H	-2.379	-1.229	0.000
15	H	-1.564	-3.436	0.000
16	H	0.153	-3.697	0.000

Table 25
Standard Geometry Coordinates of the Pyrimidines

Cytosine

No.	Atom	x	y	z
1	N	-1.207	-0.992	0.000
2	C	-1.225	0.438	0.000
3	C	-0.067	-1.725	0.000
4	H	-2.118	-1.429	0.000
5	O	-2.308	0.999	0.000
6	N	0.000	1.057	0.000
7	C	1.141	-1.102	0.000
8	H	-0.177	-2.805	0.000
9	C	1.108	0.340	0.000
10	H	2.067	-1.661	0.000
11	N	2.283	1.022	0.000
12	H	2.242	2.029	0.000
13	H	3.173	0.557	0.000

Thymine

No.	Atom	x	y	z
1	N	0.149	-1.667	0.000
2	C	1.362	-0.989	0.000
3	C	-1.082	-1.043	0.000
4	H	0.224	-2.673	0.000
5	O	2.441	-1.552	0.000
6	N	1.200	0.388	0.000
7	C	-1.218	0.302	0.000
8	H	-1.936	-1.712	0.000
9	C	0.000	1.123	0.000
10	C	-2.538	1.014	0.000
11	H	2.056	0.929	0.000
12	O	0.022	2.344	0.000
13	H	-3.372	0.306	0.000
14	H	-2.630	1.663	0.877
15	H	-2.630	1.663	-0.877

Table 26
Standard Geometry Coordinates of the Nucleotide Base-Pairs

Cytosine-Guanine

No.	Atom	x	y	z
1	N	-2.685	-3.850	0.000
2	C	-1.647	-4.770	0.000
3	C	-2.111	-2.604	0.000
4	H	-3.676	-4.037	0.000
5	N	-0.468	-4.208	0.000
6	C	-0.733	-2.849	0.000
7	N	-2.770	-1.427	0.000
8	H	-1.837	-5.835	0.000
9	C	0.146	-1.720	0.000
10	C	-1.945	-0.389	0.000
11	O	1.387	-1.705	0.000
12	N	-0.575	-0.510	0.000
13	N	-2.441	0.866	0.000
14	H	0.000	0.349	0.000
15	H	-1.851	1.701	0.000
16	H	-3.443	0.954	0.000
17	N	1.113	1.885	0.000
18	C	2.450	1.796	0.000
19	C	0.487	3.090	0.000
20	N	1.303	4.240	0.000
21	O	-0.739	3.245	0.000
22	C	3.288	2.972	0.000
23	N	2.992	0.575	0.000
24	C	2.663	4.175	0.000
25	H	0.813	5.124	0.000
26	H	4.368	2.899	0.000
27	H	2.390	-0.271	0.000
28	H	3.993	0.469	0.000
29	H	3.194	5.120	0.000

Adenine-Thymine

No.	Atom	x	y	z
1	N	-2.664	-4.245	0.000
2	C	-1.549	-5.060	0.000
3	C	-2.207	-2.947	0.000
4	H	-3.632	-4.529	0.000
5	N	-0.420	-4.395	0.000
6	C	-0.814	-3.068	0.000
7	N	-2.924	-1.812	0.000
8	H	-1.638	-6.138	0.000
9	C	-0.079	-1.859	0.000
10	C	-2.131	-0.742	0.000
11	N	1.262	-1.815	0.000
12	N	-0.784	-0.704	0.000
13	H	-2.612	0.233	0.000
14	H	1.753	-0.918	0.000
15	H	1.775	-2.682	0.000
16	N	0.458	1.855	0.000
17	C	-0.400	2.937	0.000
18	C	1.846	1.890	0.000
19	H	0.000	0.912	0.000
20	O	-1.618	2.850	0.000
21	N	0.259	4.164	0.000
22	C	2.457	3.223	0.000
23	O	2.508	0.846	0.000
24	C	1.629	4.293	0.000
25	H	-0.344	4.973	0.000
26	C	3.954	3.319	0.000
27	H	2.000	5.313	0.000
28	H	4.284	4.361	0.000
29	H	4.377	2.819	0.877
30	H	4.377	2.819	-0.877

Table 27
Standard Geometry Coordinates of the Sugar-Phosphate Backbone Components

1-Amino-Deoxyribose

No.	Atom	x	y	z
1	H	-3.168	-1.407	-0.419
2	N	-2.312	-1.363	0.118
3	H	-2.528	-1.429	1.104
4	C	-1.509	-0.212	-0.200
5	C	-0.809	0.408	1.012
6	H	-0.443	-0.396	1.660
7	H	-1.458	1.072	1.596
8	H	-2.094	0.554	-0.734
9	O	-0.420	-0.598	-1.063
10	C	0.749	0.173	-0.770
11	C	0.385	1.127	0.385
12	O	0.019	2.381	-0.199
13	H	1.215	1.253	1.089
14	H	-0.587	2.825	0.408
15	H	1.008	0.777	-1.651
16	C	1.924	-0.763	-0.476
17	H	2.856	-0.235	-0.727
18	O	1.932	-1.157	0.899
19	H	1.837	-1.636	-1.136
20	H	2.849	-1.252	1.178

Dimethyl Phosphate

No.	Atom	x	y	z
1	H	-2.923	1.263	-0.409
2	C	-1.881	1.227	-0.061
3	O	-1.194	0.239	-0.801
4	P	0.008	-0.625	0.002
5	O	0.813	0.664	0.736
6	C	1.938	1.184	0.057
7	H	1.776	1.266	-1.025
8	H	-1.897	0.997	1.011
9	H	-1.429	2.222	-0.194
10	O	0.879	-1.209	-1.069
11	O	-0.618	-1.391	1.128
12	H	2.149	2.183	0.465
13	H	2.827	0.554	0.202

Appendix 2: Potential Energy Distributions

Table 28
Internal and Symmetry Coordinates of Adenine

No.[a]	Internal Valence Coordinates definition [b]	description [c]	Local Symmetry Coordinates designation [d]	internal coordinate combination [e]
1	N-H stretch	N(1) - H(4)	-N–H stretch	1
2		N(11) - H(14)	-NH_2 asym stretch	$(2^{-1/2})$(2-3)
3		N(11) - H(15)	-NH_2 sym stretch	$(2^{-1/2})$(2+3)
4	C-H stretch	C(2) - H(8)	=C–H stretch	4
5		C(10) - H(13)	=C–H stretch	5
6	C-N stretch	C(9) - N(11)	-C–N(H_2) stretch	6
7		C(3) - N(7)	=C(C)–N= stretch	7
8		C(10) - N(12)	=C–N= stretch	8
9		C(6) - N(5)	=C(C)–N= stretch	9
10		C(3) - N(1)	=C(C)–N- stretch	10
11		C(2) - N(1)	=C–N- stretch	11
12	C-C stretch	C(6) - C(9)	=C(C)–C(NH_2) stretch	12
13	C=N stretch	C(2) - N(5)	-C(N)=N- stretch	13
14		C(9) - N(12)	-C(C)=N- stretch	14
15		C(10) - N(7)	-C(N)=N- stretch	15
16	C=C stretch	C(3) - C(6)	-C=C- stretch	16
17	H-N-H bend	α(14-11-15)	N-H i/p bend	$(2^{-1/2})$(20-21)
18	C-N-H i/p bend	α(9-11-14)	=C(2)-H i/p bend	$(2^{-1/2})$(22-24)
19		α(9-11-15)	=C(10)-H i/p bend	$(2^{-1/2})$(23-25)
20		α(2-1-4)	6-ring deform	$(12^{-1/2})$(2*30-36-29+2*34-31-35)
21		α(3-1-4)	6-ring deform	$(6^{-1/2})$(30-36+29-34+31-35)
22	N-C-H i/p bend	α(1-2-8)	6-ring deform	(2^{-1})(29-36+35-31)
23		α(12-10-13)	6-ring bend	$(12^{-1/2})$(2*37-38-42+2*43-44-45)
24	N=C-H i/p bend	α(5-2-8)	6-ring pseudorotation	$(6^{-1/2})$(37-38+42-43+44-45)
25		α(7-10-13)	6-ring twist	(2^{-1})(42-38+45-44)
26	N=C-N i/p bend	α(12-9-11)	5-ring deform	$(2^{-1/2})$(33-28)
27	C-C-N i/p bend	α(6-9-11)	5-ring deform	$(6^{-1/2})$(2*32-28-33)
28	C-N-C ring bend	α(2-1-3)	5-ring twist	$(2^{-1/2})$(39-41)
29	C=C-N ring bend	α(6-3-7)	5-ring bend	$(6^{-1/2})$(2*40-39-41)
30	N=C-C ring bend	α(12-9-6)	butterfly	(2^{-1})(37+39+41+43)
31	N=C-N ring bend	α(7-10-12)	N-H o/p bend	49
32		α(5-2-1)	C-H o/p bend	50
33	C=N-C ring bend	α(2-5-6)	C-H o/p bend	51
34		α(10-7-3)	-C-N(H_2) i/p wag	$(2^{-1/2})$(26-27)
35		α(9-12-10)	H-N-H scis	$(6^{-1/2})$(2*17-18-19)
36	C=C-C ring bend	α(3-6-9)	H-N-H rock	$(2^{-1/2})$(18-19)
37	C(10)=N(12) ring	τ(7-10-12-9)	H-N-H inversion	48
38	N(12)-C(9) ring	τ(10-12-9-6)	H-N-H sym torsion	46-47
39	C(9)=C(6) ring	τ(12-9-6-5)	H-N-H asym torsion	46+47
40	C(6)-N(5) ring	τ(9-6-5-2)		
41	N(5)=C(2) ring	τ(6-5-2-1)		
42	C(2)-N(1) ring	τ(5-2-1-3)		

Table 28 (cont.)

No.[a]	Internal Valence Coordinates definition [b]	description [c]
43	N(1)-C(3) ring	τ(2-1-3-7)
44	C(3)=N(7) ring	τ(1-3-7-10)
45	N(7)-C(10) ring	τ(3-7-10-12)
46	N(11)-H torsion	τ(6-9-11-15)
47		τ(12-9-11-14)
48	$N-H_2$ inversion	γ(9-14-15-11)
49	N-H o/p bend	γ(4-2-3-1)
50	C-H o/p bend	γ(8-1-5-2)
51		γ(13-7-12-10)

[a] Internal valence and local symmetry coordinate numbers

[b] i/p = in-plane; o/p = out-of-plane.

[c] Atom numbers of adenine in parenthesis see Figure 2, page 9; α = bending-in-plane; γ = bending-out-of-plane; τ = twisting

[d] sym = symmetric; asym = antisymmetric; scis = scissors.

[e] Normalization constants followed by internal valence coordinate numbers (both in parenthesis).

Table 29
Potential Energy Distribution of Undeuterated Adenine

Mode [a]	Calculated B3-LYP/6-31G** (cm^{-1}) x 0.95 [b]	A (km mol^{-1}) [c]	% (Local Symmetry Coordinate) [d]
Q6	1592	630	26(6), 24(35), 20(12)
Q7	1567	109	27(7), 11(12), 10(10)
Q8	1535	4	45(35), 12(16)
Q9	1454	13	40(13), 21(26), 15(18)
Q10	1442	55	23(14), 23(19), 13(15), 13(6), 11(35)
Q11	1375	16	28(10), 25(16), 10(19)
Q12	1357	11	23(19), 22(17), 15(11), 14(10)
Q13	1308	33	16(11), 10(18)
Q14	1302	36	27(9), 26(8)
Q15	1277	69	37(15), 15(9), 13(8)
Q16	1211	31	34(18), 16(13), 11(17)
Q17	1188	12	29(9), 22(36)
Q18	1094	20	28(26), 19(10)
Q19	1032	17	52(11), 27(17), 10(26)
Q20	961	4	49(36), 27(14)
Q21	925	2	38(23), 35(33), 20(30)
Q22	896	15	69(27)

Table 30
Potential Energy Distribution of Deuterated Adenine

Mode [a]	Calculated B3-LYP/6-31G** (cm^{-1}) x 0.95 [b]	A (km mol^{-1}) [c]	% (Local Symmetry Coordinate) [d]
Q6	1572	524	31(12), 18(6), 14(16)
Q7	1552	93	40(7), 10(14), 10(10)
Q8	1470	35	21(6), 15(13), 11(19), 11(26)
Q9	1444	77	35(13), 13(26), 12(18)
Q10	1378	15	25(16), 22(10), 19(19), 13(6), 11(35)
Q11	1330	19	29(19), 25(10), 11(14)
Q12	1308	42	28(9), 28(8), 14(16), 10(14)
Q13	1283	51	31(15), 15(11)
Q14	1270	34	15(11), 14(9), 13(8), 13(13), 12(18), 10(15)
Q15	1187	25	32(11), 18(18)
Q16	1157	16	22(9), 15(8), 15(14), 14(15)
Q17	1130	48	36(35), 15(21), 14(26), 14(18)
Q18	1044	9	28(35), 27(26), 14(10)
Q19	925	2	38(23), 35(33), 20(30)
Q20	899	4	55(27), 17(11)
Q21	857	8	37(21), 16(26), 10(17)

[a] Q represents the normal modes of the adenine base.

[b] Wavenumbers calculated with the B3-LYP/6-31G** procedure.

[c] Intensities calculated with the B3-LYP/6-31G** procedure.

[d] Local symmetry coordinates defined in Table 28, page 145.

Table 31
Internal and Symmetry Coordinates of Guanine

No.[a]	Internal Valence Coordinates		Local Symmetry Coordinates	
	definition [b]	description [c]	designation [d]	internal coordinate combination [e]
1	N-H stretch	N(13) - H(15)	-NH_2 asym stretch	$(2^{-1/2})$(1-2)
2		N(13) - H(16)	-NH_2 sym stretch	$(2^{-1/2})$(1+2)
3		N(12) - H(14)	-N(12)–H stretch	3
4		N(1) - H(4)	-N(1)–H stretch	4
5	C-H stretch	C(2) - H(8)	=C–H stretch	5
6	C-N stretch	C(10) - N(13)	-C–N(H_2) stretch	6
7		C(9) - N(12)	-C(O)–N- stretch	7
8		C(10) - N(12)	=C–N- stretch	8
9		C(3) - N(7)	-C(C)–N= stretch	9
10		C(3) - N(1)	=C(C)–N- stretch	10
11		C(2) - N(1)	=C(C)–N- stretch	11
12		C(6) - N(5)	=C(C)–N=	12
13	C-C stretch	C(6) - C(9)	=C(C)–C(O)	13
14	C=O stretch	C(9) - O(11)	-C=O stretch	14
15	C=N stretch	C(10) - N(7)	-C(N)=N- stretch	15
16		C(2) - N(5)	-C=N- stretch	16
17	C=C stretch	C(3) - C(6)	-C=C- stretch	17
18	H-N-H bend	α(15-13-16)	N(12)-H i/p bend	$(2^{-1/2})$(21-22)
19	C-N-H i/p bend	α(10-13-15)	N(1)-H i/p bend	$(2^{-1/2})$(23-24)
20		α(10-13-16)	=C-H i/p bend	$(2^{-1/2})$(25-26)
21		α(9-12-14)	-C=O i/p wag	$(2^{-1/2})$(27-28)
22		α(10-12-14)	6-ring deform	$(12^{-1/2})$(2*31-39-34+2*37-35-32)
23		α(2-1-4)	6-ring deform	$(6^{-1/2})$(31-39+34-37+35-32)
24		α(3-1-4)	6-ring deform	(2^{-1})(34-39+32-35)
25	N-C-H i/p bend	α(1-2-8)	6-ring bend	$(12^{-1/2})$(2*40-41-45+2*46-47-48)
26	N=C-H i/p bend	α(5-2-8)	6-ring pseudorotation	$(6^{-1/2})$(40-41+45-46+47-48)
27	N-C=O i/p bend	α(12-9-11)	6-ring twist	(2^{-1})(45-41+48-47)
28	C-C=O i/p bend	α(6-9-11)	5-ring deform	$(2^{-1/2})$(38-33)
29	N-C-N i/p bend	α(12-10-13)	5-ring deform	$(6^{-1/2})$(2*36-33-38)
30	N=C-N i/p bend	α(7-10-13)	5-ring twist	$(2^{-1/2})$(42-44)
31	C-C-N ring bend	α(6-9-12)	5-ring bend	$(6^{-1/2})$(2*43-42-44)
32	N-C-N ring bend	α(9-12-10)	butterfly	(2^{-1})(40+42+44+46)
33	C-N-C ring bend	α(2-1-3)	N(12)-H o/p bend	52
34	C=C-N ring bend	α(6-3-7)	N(1)-H o/p bend	53
35	N=C-N ring bend	α(7-10-12)	C-H o/p bend	54
36		α(5-2-1)	C=O o/p bend	55
37	C=N-C ring bend	α(10-7-3)	-C-N(H_2) i/p wag	$(2^{-1/2})$(29-30)
38		α(2-5-6)	H-N-H scis	$(6^{-1/2})$(2*18-19-20)
39	C=C-C ring bend	α(3-6-9)	H-N-H rock	$(2^{-1/2})$(19-20)
40	C(10)-N(12) ring	τ(7-10-12-9)	H-N-H inversion	51
41	N(12)-C(9) ring	τ(10-12-9-6)	H-N-H sym torsion	49-50
42	C(9)-C(6) ring	τ(12-9-6-5)	H-N-H asym torsion	49+50
43	C(6)-N(5) ring	τ(9-6-5-2)		
44	N(5)=C(2) ring	τ(6-5-2-1)		

Table 31 (cont.)

No.[a]	Internal Valence Coordinates definition [b]	description [c]
45	C(2)-N(1) ring	τ(5-2-1-3)
46	N(1)-C(3) ring	τ(2-1-3-7)
47	C(3)-N(7) ring	τ(1-3-7-10)
48	N(7)=C(10) ring	τ(3-7-10-12)
49	N(11)-H torsion	τ(7-10-13-16)
50		τ(12-10-13-15)
51	$N\text{-}H_2$ inversion	γ(10-15-16-13)
52	N(12)-H o/p bend	γ(14-9-10-12)
53	N(1)-H o/p bend	γ(4-2-3-1)
54	C-H o/p bend	γ(8-1-5-2)
55	C=O o/p bend	γ(11-6-12-9)

[a] Internal valence and local symmetry coordinate numbers

[b] i/p = in-plane; o/p = out-of-plane.

[c] Atom numbers of guanine in parenthesis see Figure 2, page 9; α = bending-in-plane; γ = bending-out-of-plane; τ = twisting

[d] sym = symmetric; asym = antisymmetric; scis = scissors.

[e] Normalization constants followed by internal valence coordinate numbers (both in parenthesis).

Table 32
Potential Energy Distribution of Undeuterated Guanine

Mode [a]	Calculated B3-LYP/6-31G** (cm^{-1}) x 0.95 [b]	A (km mol^{-1}) [c]	% (Local Symmetry Coordinate) [d]
Q6	1738	583	71(14), 15(13)
Q7	1590	683	36(38), 28(6), 21(15)
Q8	1542	272	32(9), 14(17), 13(10)
Q9	1530	48	33(38), 28(15), 10(17)
Q10	1489	74	14(16), 12(8)
Q11	1451	2	39(16), 15(28)
Q12	1371	21	24(17), 20(10), 15(8), 11(16)
Q13	1322	14	29(19), 28(11), 10(29)
Q14	1300	11	27(12), 19(13), 14(10)
Q15	1272	50	40(18), 16(12), 11(6)
Q16	1250	0.4	36(20), 14(16), 10(12)
Q17	1120	29	24(28), 17(10), 16(20), 10(12)
Q18	1072	29	24(7), 18(15), 16(39), 10(21)
Q19	1020	18	51(11), 25(19)
Q20	1011	15	34(7), 16(8), 10(39)
Q21	977	5	41(39), 24(8)
Q22	898	9	75(29)

Table 33
Potential Energy Distribution of Deuterated Guanine

Mode [a]	Calculated B3-LYP/6-31G** (cm^{-1}) x 0.95 [b]	A (km mol^{-1}) [c]	% (Local Symmetry Coordinate) [d]
Q6	1731	569	72(14), 15(13)
Q7	1546	796	47(15), 22(6), 10(24)
Q8	1521	74	36(9), 26(17), 13(10)
Q9	1486	140	15(16), 12(8), 11(17), 10(6)
Q10	1446	10	42(16), 14(28)
Q11	1360	44	23(17), 19(10), 18(8)
Q12	1298	19	41(12), 16(13), 14(10)
Q13	1269	9	33(20), 22(11), 10(28), 10(29), 10(16)
Q14	1231	5	30(11), 10(19)
Q15	1177	14	37(38), 13(11), 12(18)
Q16	1112	30	28(28), 19(20), 13(23), 10(10)
Q17	1066	42	40(7), 13(38)
Q18	1018	7	22(38), 11(21), 10(10)
Q19	918	17	18(18), 13(29), 13(39), 10(7), 10(8)
Q20	895	1	51(29), 20(11)

[a] Q represents the normal modes of the guanine base.

[b] Wavenumbers calculated with the B3-LYP/6-31G** procedure.

[c] Intensities calculated with the B3-LYP/6-31G** procedure.

[d] Local symmetry coordinates defined in Table 31, page 148.

Table 34
Internal and Symmetry Coordinates of Thymine

No.[a]	Internal Valence Coordinates		Internal Symmetry Coordinates	
	definition [b]	description [c]	designation [d]	internal coordinate combination [e]
1	N-H stretch	N(6) - H(11)	-N–H stretch	1
2		N(1) - H(4)	-N–H stretch	2
3	C-H stretch	C(3) - H(8)	=C–H stretch	3
4		C(10) - H(13)	$-CH_3$ asym stretch	$(6^{-1/2})(2*4-5-6)$
5		C(10) - H(14)	$-CH_3$ asym stretch	$(2^{-1/2})(5-6)$
6		C(10) - H(15)	$-CH_3$ sym stretch	$(3^{-1/2})(4+5+6)$
7	C-N stretch	C(2) - N(1)	-C(O) –N- stretch	7
8		C(3) - N(1)	=C–N(C)- stretch	8
9		C(2) - N(6)	-C(O)–N- stretch	9
10		C(9) - N(6)	-C(O)–N - stretch	10
11	C-C stretch	C(7) - C(9)	=C–C(O) stretch	11
12		C(7) - C(10)	$=C-CH_3$ stretch	12
13	C=O stretch	C(2) - O(5)	-C=O	13
14		C(9) - O(12)	-C=O	14
15	C=C stretch	C(3) - C(7)	-C=C-	15
16	H-C-H bend	α(13-10-15)	-C–H (Me) asym deform	$(6^{-1/2})(2*16-17-18)$
17	H-C-H bend	α(13-10-14)	-C–H (Me) asym deform	$(2^{-1/2})(17-18)$
18	H-C-H bend	α(14-10-15)	-C–H (Me) sym deform	$(3^{-1/2})(16+17+18)$
19	C-N-H i/p bend	α(9-6-11)	-N–H i/p bend	$(2^{-1/2})(19-20)$
20		α(2-6-11)	-N–H i/p bend	$(2^{-1/2})(21-22)$
21		α(2-1-4)	=C–H i/p bend	$(2^{-1/2})(23-24)$
22		α(3-1-4)	-C=O i/p wag	$(2^{-1/2})(25-28)$
23	N-C-H i/p bend	α(1-3-8)	-C=O i/p wag	$(2^{-1/2})(26-27)$
24	C=C-H i/p bend	α(7-3-8)	$=C-CH_3$ wag	$(2^{-1/2})(29-30)$
25	N-C=O i/p bend	α(6-9-12)	$-CH_3$ i/p rock	$(6^{-1/2})(2*31-32-33)$
26		α(6-2-5)	$-CH_3$ o/p rock	$(6^{-1/2})(2*33-31-32)$
27		α(1-2-5)	6-ring deform	$(12^{-1/2})(2*39-38-37+2*34-36-35)$
28	C-C=O	α(7-9-12)	6-ring deform	$(6^{-1/2})(39-38+37-34+36-35)$
29	C-C-C	α(9-7-10)	6-ring deform	$(2^{-1})(37-38+35-36)$
30	C=C-C	α(3-7-10)	6-ring bend	$(12^{-1/2})(2*40-41-42+2*43-44-45)$
31	C-C-H (Me) bend	α(7-10-13)	6-ring pseudorotation	$(6^{-1/2})(40-41+42-43+44-45)$
32		α(7-10-14)	6-ring twist	$(2^{-1})(42-41+45-44)$
33		α(7-10-15)	H-C-H (Me) torsion	46
34	C-N-C ring bend	α(2-1-3)	$C-CH_3$ o/p bend	47
35		α(2-6-9)	N–H o/p bend	48
36	N-C-N ring bend	α(1-2-6)	N–H o/p bend	49
37	C=C-N ring bend	α(7-3-1)	C–H o/p bend	50
38	C=C-C ring bend	α(3-7-9)	C=O o/p bend	51
39	C-C-N ring bend	α(7-9-6)	C=O o/p bend	52
40	C(2)-N(6) ring	τ(1-2-6-9)		
41	N(6)=C(9) ring	τ(2-6-9-7)		
42	C(9)-C(7) ring	τ(6-9-7-3)		
43	C(7)=C(3) ring	τ(9-7-3-1)		
44	C(3)-N(1) ring	τ(7-3-1-2)		

Table 34 (cont.)

No.[a]	Internal Valence Coordinates definition [b]	description [c]
45	N(1)-C(2) ring	τ(3-1-2-6)
46	C-H_3 torsion	τ(3-7-10-13)
		τ(9-7-10-14)
		τ(3-7-10-15)
47	C-CH_3 o/p bend	γ(10-3-9-7)
48	N-H o/p bend	γ(4-2-3-1)
49		γ(11-2-9-6)
50	C-H o/p bend	γ(8-1-7-3)
51	C=O o/p bend	γ(5-1-6-2)
52		γ(12-6-7-9)

[a] Internal valence and local symmetry coordinate numbers

[b] i/p = in-plane; o/p = out-of-plane.

[c] Atom numbers of thymine in parenthesis see Figure 2, page 9; α = bending-in-plane; γ = bending-out-of-plane; τ = twisting

[d] sym = symmetric; asym = antisymmetric; scis = scissors.

[e] Normalization constants followed by internal valence coordinate numbers (both in parenthesis).

Table 35
Potential Energy Distribution of Undeuterated Thymine

Mode [a]	Calculated B3-LYP/6-31G** (cm^{-1}) x 0.95 [b]	A (km mol^{-1}) [c]	% (Local Symmetry Coordinate) [d]
Q7	1751	644	70(13)
Q8	1701	488	74(14)
Q9	1629	44	60(15), 13(21)
Q10	1435	51	40(17), 13(16), 10(8)
Q11	1424	62	27(20), 19(17), 13(8)
Q12	1409	6	69(16), 23(17)
Q13	1363	2	87(18), 10(12)
Q14	1355	90	17(9), 17(20), 13(11)
Q15	1330	12	52(19), 11(21)
Q16	1310	8	32(21), 14(19), 11(15), 10(9)
Q17	1174	17	26(12), 19(8), 10(11), 10(7), 10(28)
Q18	1141	111	19(9), 18(21), 16(20), 15(10), 11(8)
Q19	1101	6	31(10), 13(8), 11(25)
Q20	1018	2	74(26)
Q21	975	2	52(25), 13(26), 12(28)
Q22	918	10	26(7), 17(25)
Q23	864	14	86(37)

Table 36
Potential Energy Distribution of Deuterated Thymine

Mode [a]	Calculated B3-LYP/6-31G** (cm^{-1}) x 0.95 [b]	A (km mol^{-1}) [c]	% (Local Symmetry Coordinate) [d]
Q7	1739	535	72(13)
Q8	1693	577	72(14)
Q9	1625	32	60(15), 12(21)
Q10	1433	16	58(17), 19(16), 11(25)
Q11	1409	6	69(16), 23(17)
Q12	1392	177	18(11), 16(7), 14(8), 11(29)
Q13	1362	4	90(18)
Q14	1311	25	41(21), 13(7), 11(15), 10(9)
Q15	1283	88	23(9), 23(8), 14(20), 12(21)
Q16	1193	2	32(10), 18(9), 17(8), 13(19)
Q17	1161	16	31(12), 14(28), 10(21)
Q18	1042	21	17(7), 15(19), 13(22), 12(10)
Q19	1018	2	74(26)
Q20	999	12	56(25), 14(26)
Q21	892	4	46(20), 17(25), 12(8)
Q22	864	14	87(37)

[a] Q represents the normal modes of the thymine base.

[b] Wavenumbers calculated with the B3-LYP/6-31G** procedure.

[c] Intensities calculated with the B3-LYP/6-31G** procedure.

[d] Local symmetry coordinates defined in Table 34, page 151.

Table 37
Internal and Symmetry Coordinates of Cytosine

No.[a]	Internal Valence Coordinates		Local Symmetry Coordinates	
	definition [b]	description [c]	designation [d]	internal coordinate combination [e]
1	N-H stretch	N(11) - H(12)	-NH_2 asym stretch	$(2^{-1/2})(1 - 2)$
2		N(11) - H(13)	-NH_2 sym stretch	$(2^{-1/2})(1 + 2)$
3		N(1) - H(4)	-N–H stretch	3
4	C-H stretch	C(3) - H(8)	=C–H asym stretch	$(2^{-1/2})(4 - 5)$
5		C(7) - H(10)	=C–H sym stretch	$(2^{-1/2})(4 + 5)$
6	C-N stretch	C(9) - N(11)	-C–N(H_2) stretch	6
7		C(2) - N(1)	-C(O)–N- stretch	7
8		C(3) - N(1)	=C–N(C)- stretch	8
9		C(2) - N(6)	-C(O)–N= stretch	9
10	C-C stretch	C(9) - C(7)	=C–C= stretch	10
11	C=O stretch	C(2) - O(5)	-C=O stretch	11
12	C=N stretch	C(9) - N(6)	-C=N- stretch	12
13	C=C stretch	C(3) - C(7)	-C=C- stretch	13
14	H-N-H bend	α(12-11-13)	N-H i/p bend	$(2^{-1/2})(17-18)$
15	C-N-H i/p bend	α(9-11-12)	=C-H asym bend	$(2^{-1})(19-22+21-20)$
16		α(9-11-13)	=C-H sym bend	$(2^{-1})(19-22-21+20)$
17		α(2-1-4)	-C=O i/p wag	$(2^{-1/2})(25-26)$
18		α(3-1-4)	6-ring deform	$(12^{-1/2})(2*32-31-29+2*27-28-30)$
19	N-C-H i/p bend	α(1-3-8)	6-ring deform	$(6^{-1/2})(32-31+29-27+28-30)$
20	C-C-H i/p bend	α(9-7-10)	6-ring deform	$(2^{-1})(29-31+30-28)$
21	C=C-H i/p bend	α(3-7-10)	6-ring bend	$(12^{-1/2})(2*33-34-35+2*36-37-38)$
22		α(7-3-8)	6-ring pseudorotation	$(6^{-1/2})(33-34+35-36+37-38)$
23	N=C-N i/p bend	α(6-9-11)	6-ring twist	$(2^{-1})(35-34+38-37)$
24	C-C-N i/p bend	α(7-9-11)	N-H o/p bend	42
25	N-C=O i/p bend	α(1-2-5)	C-H asym o/p bend	$(2^{-1/2})(43-44)$
26		α(6-2-5)	C-H sym o/p bend	$(2^{-1/2})(43+44)$
27	C-N-C ring bend	α(2-1-3)	C=O o/p bend	45
28	N-C-N ring bend	α(1-2-6)	-C-N(H_2) i/p wag	$(2^{-1/2})(23-24)$
29	C=C-N ring bend	α(1-3-7)	H-N-H scis	$(6^{-1/2})(2*14-15-16)$
30	C=N-C ring bend	α(2-6-9)	H-N-H rock	$(2^{-1/2})(15-16)$
31	C=C-C ring bend	α(3-7-9)	H-N-H inversion	41
32	N=C-C ring bend	α(6-9-7)	H-N-H sym torsion	$(2^{-1/2})(39-40)$
33	C(2)-N(6) ring	τ(1-2-6-9)	H-N-H asym torsion	$(2^{-1/2})(39+40)$
34	N(6)=C(9) ring	τ(2-6-9-7)		
35	C(9)-C(7) ring	τ(6-9-7-3)		
36	C(7)=C(3) ring	τ(9-7-3-1)		
37	C(3)-N(1) ring	τ(7-3-1-2)		
38	N(1)-C(2) ring	τ(3-1-2-6)		
39	N(11)-H torsion	τ(6-9-11-12)		
40		τ(7-9-11-13)		
41	N-H_2 inversion	γ(9-12-13-11)		
42	N(1)-H o/p bend	γ(4-2-3-1)		
43	C-H o/p bend	γ(8-1-7-3)		
44		γ(10-3-9-7)		
45	C=O o/p bend	γ(5-1-6-2)		

Table 38
Potential Energy Distribution of Undeuterated Cytosine

Mode [a]	Calculated B3-LYP/6-31G** (cm^{-1}) x 0.95 [b]	A (km mol^{-1}) [c]	% (Local Symmetry Coordinate) [d]
Q6	1728	617	74(11)
Q7	1620	464	40(13), 13(16), 13(12), 10(8)
Q8	1558	156	73(29), 15(6)
Q9	1497	161	27(12), 23(10)
Q10	1443	99	27(15), 20(12), 18(6), 11(8), 11(29)
Q11	1373	80	34(14), 17(8), 13(10)
Q12	1297	34	44(15), 19(6), 11(13), 10(14)
Q13	1202	33	45(9), 11(7)
Q14	1157	42	44(16), 22(14), 16(8)
Q15	1074	4	27(8), 27(16), 15(13), 13(15), 10(14)
Q16	1029	41	39(30), 18(7), 16(17)
Q17	938	0.02	51(19), 25(10)
Q18	908	0.3	84(25)
Q19	874	4	27(7), 18(10), 14(30), 12(19)

Table 39
Potential Energy Distribution of Deuterated Cytosine

Mode [a]	Calculated B3-LYP/6-31G** (cm^{-1}) x 0.95 [b]	A (km mol^{-1}) [c]	% (Local Symmetry Coordinate) [d]
Q6	1720	630	77(11), 10(9)
Q7	1613	361	43(13), 14(16), 13(12), 10(8)
Q8	1480	175	31(12), 26(10), 12(13)
Q9	1463	261	37(6), 19(15), 15(12)
Q10	1338	132	24(15), 20(6), 15(8)
Q11	1276	22	27(15), 25(8), 12(14)
Q12	1207	33	41(9), 14(7)
Q13	1116	16	52(16), 19(29)
Q14	1086	11	46(29), 13(16)
Q15	960	14	22(19), 17(7), 17(10), 14(17)
Q16	924	13	27(14), 27(19), 13(8), 10(7)
Q17	909	1	84(25)
Q18	874	4	35(14), 15(19), 15(30)

[a] Q represents the normal modes of the cytosine base.

[b] Wavenumbers calculated with the B3-LYP/6-31G** procedure.

[c] Intensities calculated with the B3-LYP/6-31G** procedure.

[d] Local symmetry coordinates defined in Table 37, page 154.

Table 40
Potential Energy Distribution of the Undeuterated Cytosine-Guanine Base-Pair

Mode [a]	Calculated B3-LYP/6-31G** (cm^{-1}) x 0.95 [b]	A (km mol^{-1}) [c]	% (Local Symmetry Coordinate) [d]
Q11(cg)	1693	1199	15(C26), 12(C42), 12(C28), 12(G14), 11(C43)
Q12(cg)	1664	82	19(H31), 15(C42), 13(G14)
Q13(cg)	1635	653	26(C41), 19(C29), 10(C23)
Q14(cg)	1617	339	24(G6), 22(G53), 10(G52)
Q15(cg)	1599	139	27(C30), 21(C41), 10(C39)
Q16(cg)	1578	219	40(G53), 15(G44), 12(H33)
Q17(cg)	1547	114	28(G9), 19(G17), 15(G53), 12(G44)
Q18(cg)	1496	3	23(G8), 18(G44), 12(G52), 12(G53)
Q19(cg)	1486	138	25(C34), 17(C42), 13(C43)
Q20(cg)	1468	108	53(C29)
Q21(cg)	1461	47	27(G8), 16(G44), 15(G53), 10(G9)
Q22(cg)	1386	40	22(52G), 14(17G), 12(51G), 11(34C), 10(G6)
Q23(cg)	1376	93	30(C34), 20(C29), 16(C40), 10(H33)
Q24(cg)	1354	58	32(G8), 26(G44), 12(G53), 10(G17)
Q25(cg)	1321	16	16(G17), 13(G50), 11(G44), 10(G51)
Q26(cg)	1321	5	40(C38), 23(C42)
Q27(cg)	1300	38	26(G50), 18(G7), 15(G51), 11(G8)
Q28(cg)	1259	3	21(G7), 21(G9), 14(G17)
Q29(cg)	1247	71	49(C26), 23(C40), 11(C29)
Q30(cg)	1166	42	35(C39), 29(C42), 13(C25)
Q31(cg)	1135	49	50(G7), 16(G50), 14(H33), 11(G52)
Q32(cg)	1116	9	28(G7), 16(G50), 14(G53), 12(H31), 10(G8)
Q33(cg)	1088	50	39(C40), 19(H33)
Q34(cg)	1069	23	26(C40), 18(C42), 14(C25), 12(H33)
Q35(cg)	1059	3	32(G7), 14(H31), 14(G50)
Q36(cg)	1018	18	27(H33), 26(G8), 11(G50), 10(G11)
Q37(cg)	1008	2	50(H33), 23(G8), 16(G50)
Q38(cg)	954	0.3	38(C42), 32(H33), 11(C40)
Q39(cg)	921	0.2	37(H33), 31(C42), 10(C34)
Q40(cg)	913	0.2	76(C73), 11(C65)
Q41(cg)	898	13	27(G17), 21(H33), 15(G51)
Q42(cg)	871	145	43(G77), 19(C76), 17(H7), 15(C67)

[a] Q(cg) represents the normal modes of the undeuterated C-G base-pair.

[b] Wavenumbers calculated with the B3-LYP/6-31G** procedure.

[c] Intensities calculated with the B3-LYP/6-31G** procedure.

[d] Local symmetry coordinates defined in Table 4, page 68.

Table 41
Potential Energy Distribution of the Undeuterated Adenine-Thymine Base-Pair

Mode [a]	Calculated B3-LYP/6-31G** (cm^{-1}) x 0.95 [b]	A ($km\ mol^{-1}$) [c]	% (Local Symmetry Coordinate) [d]
Q12(at)	1739	583	57(T17), 43(H33)
Q13(at)	1663	452	47(T29), 17(T25), 13(T48)
Q14(at)	1625	13	44(T30), 11(T46), 10(T26)
Q15(at)	1616	388	55(T31)
Q16(at)	1568	261	36(A50), 24(A6)
Q17(at)	1553	13	20(A57), 16(A12), 15(A49)
Q18(at)	1476	26	21(A7), 17(A16), 13(A54)
Q19(at)	1460	5	33(T38), 15(A54), 13(T30)
Q20(at)	1451	66	22(A54), 13(A13), 11(H34)
Q21(at)	1438	75	30(A54), 12(A14), 12(A13)
Q22(at)	1426	49	18(T36), 17(T48), 13(T24)
Q23(at)	1410	5	21(T36), 17(T48), 12(T39)
Q24(at)	1382	11	69(T35), 23(T36)
Q25(at)	1363	5	33(A54), 16(H34), 13(A16), 10(A56)
Q26(at)	1359	92	82(T37)
Q27(at)	1356	5	18(T42), 13(A54), 10(T25), 10(T41)
Q28(at)	1314	13	33(A54), 23(H34)
Q29(at)	1312	20	18(A54), 11(A7), 10(A14)
Q30(at)	1301	37	30(T40), 15(T42), 15(T25), 12(T31)
Q31(at)	1285	106	32(A8), 15(A9), 12(A14)
Q32(at)	1210	20	42(H34), 22(A54), 11(A15)
Q33(at)	1206	35	24(H34), 17(A53), 13(A54)
Q34(at)	1184	23	19(A49), 15(A51), 14(A9), 12(A8)
Q35(at)	1170	80	34(T25), 28(T26)
Q36(at)	1119	17	24(T47), 21(T28), 19(T24), 16(T26)
Q37(at)	1101	17	16(T24), 16(T26), 16(H33)
Q38(at)	1031	18	17(A58), 13(A56), 11(A10)
Q39(at)	1018	4	49(A11), 25(A52), 11(A58)
Q40(at)	995	19	72(T45)
Q41(at)	977	17	31(H33), 26(A14), 14(A51)
Q42(at)	963	73	25(T44), 22(H33), 21(T47)
Q43(at)	947	12	66(T77), 12(A60)
Q44(at)	941	18	38(A83), 34(A60), 18(A65)
Q45(at)	899	17	23(T42), 16(T41), 12(T23), 11(T44), 11(H33)
Q46(at)	866	11	50(A59), 13(H33)

[a] Q(at) represents the normal modes of the undeuterated A-T base-pair.

[b] Wavenumbers calculated with the B3-LYP/6-31G** procedure.

[c] Intensities calculated with the B3-LYP/6-31G** procedure.

[d] Local symmetry coordinates defined in Table 6, page 72.

Appendix 3: Conversion of Units

$$1\left[km\ mol^{-1}\right] = \sqrt{2\pi}\ \bar{\nu}\left[cm^{-1}\right] \cdot \text{Dipole strength}\left[Debye^{2}\right]$$

$$1\left[Debye\right] = 10^{-18}\left[esu\ cm\right]$$

$$\text{Dipole Strength}\left[esu^{2}\ cm^{2}\right] = \frac{1}{\bar{\nu}\left[cm^{-1}\right] \cdot \left(1.088 \times 10^{38}\right)} \int_{band} \varepsilon(\bar{\nu})\left[M^{-1}\ cm^{-1}\right] \partial\bar{\nu}$$

$$\text{Rotational strength}\left[esu^{2}\ cm^{2}\right] = \frac{1}{\bar{\nu}\left[cm^{-1}\right] \cdot \left(4.352 \times 10^{38}\right)} \int_{band} \Delta\varepsilon(\bar{\nu})\left[M^{-1}\ cm^{-1}\right] \partial\bar{\nu}$$

where the integral is obtained by integrating the intensity of the VCD band at wavenumber $\bar{\nu}$ from a plot of $\Delta\varepsilon(\bar{\nu})$ versus $\bar{\nu}$.